Modeling the atmospheric diurnal cycle

van Hooft, Antoon

DOI
10.4233/uuid:e45cea45-8915-4a11-b8fd-389cb3e19d22

Publication date
2021

Document Version
Final published version

Important note
To cite this publication, please use the final published version (if applicable).
Please check the document version above.

Modeling the Atmospheric Diurnal Cycle

Johannes Antonius van Hooft

November 9, 2020

.

On the cover:
A large vortex (red ring) entrains vorticity-rich fluid (blue) from the viscous boundary layer into the interior flow. In the rear, the used quadtree grid structure that is used to compute the flow's evolution and represent the title' letters is drawn. The snapshot is generated with `Basilisk view` and may be reproduced:
`http://www.basilisk.fr/sandbox/Antoonvh/front_page.c`

Modeling the Atmospheric Diurnal Cycle

Proefschrift

ter verkrijging van de graad van doctor
aan the Technische Universteit Delft,
op gezag van de Rector Magnificus Prof. dr. ir. T.H.J.J. van der Hagen,
voorzitter van het College van Promoties,
in het openbaar te verdedigen op 20 Januari 2021

door

Johannes Antonius VAN HOOFT

Ingenieur in de technische natuurkunde,
Technische Universiteit Eindhoven, Nederland.
Geboren in Maasdriel, Nederland.

Dit proefschrift is goedgekeurd door de

promotor:	Prof. Dr. ir. B.J.H. van de Wiel
promotor:	Prof. Dr. ir. H.W.J. Russchenberg
co-promotor:	Dr. S. Popinet

Samenstelling van de promotiecommisie:

Rector Magnificus,	Voorzitter
Prof Dr. ir. B.J.H. van de Wiel	Technische Universiteit Delft
Prof Dr. ir. H.W.J. Russchenberg	Technische Universiteit Delft
Dr. S. Popinet	CNRS/Sorbonne Université Paris

Onafhankelijke leden:	
Prof Dr. ir. W.S.J. Uijttewaal	Technische Universiteit Delft
Dr. ir. J. Tomas	RIVM/VLH
Prof. Dr. J. Vila-Guerau de Arellano	Wagenigen University and Research
Prof. Dr. ir. B.J. Boersma	Technische Universiteit Delft

keywords:
Atmospheric boundary layer, diurnal cycle, modeling, adaptive methods, weather
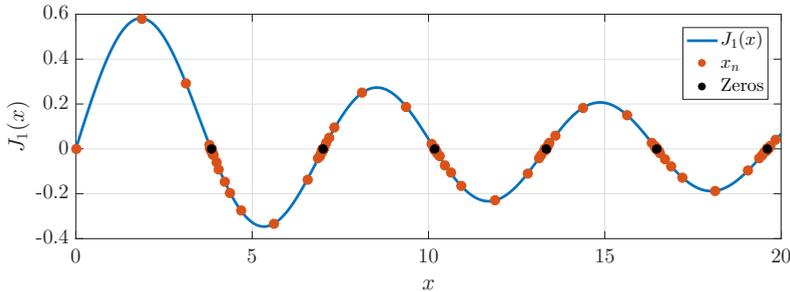
Ik bedank Saskia voor alle liefde en geluk die ze mij schenkt. Ik kijk uit naar de toekomst met ons gezin.

Contents

Say we wish to approximate the roots of an analytical function on a finite domain; i.e. the solution (x) to $f(x) = 0$ for $x \in (x_0,\ x_0 + L_0)$. A *brute force* method for doing this is to first discretize the x-axis with N grid points spaced $\Delta = L_0/N$ apart, such that the n-th cell center corresponds to $x_n = x_0 + \Delta(n + \frac{1}{2})$. Next, for each grid point we check if the function changes sign within the i-th cell: $f(x_i - \Delta/2)f(x_i + \Delta/2) \leq 0$. If this is the case, the cells 'contains' a root and x_i is an approximation of that root with accuracy $\pm\Delta/2$. When pushing the fidelity of the approximations using this method (i.e. lowering Δ), it is tempting to increase N. Intuitively, the required computer effort (E) grows linearly with N or, $E \propto \Delta^{-1}$. This scaling exponent reflects the one-dimensional character of the embedding space (x).

Alternatively, one may push the resolution by *adaptively* increasing the resolution of *only* the cells that contain roots. A cell can be split into two cells with half the grid size and the process can be repeated for more accurate estimations. When the function has R roots, only $2R$ new cells need to be studied in order to double the resolution. Interestingly, the required computer effort for the evaluation of the numerical methods does not scale with the fidelity of the approximation anymore, i.e. $E \propto \Delta^0$. This asymptotic scaling exponent reflects the point character of the roots (i.e. zero dimensional).

The favorable scaling exponent with Δ and the fact that the effort required for evaluation of the numerical method automatically reflects the complexity of the problem (e.g. the number of roots) are desirable features that characterize *adaptive numerical methods*.

For a test of the implementation of this method applied to the non-trivial roots of first Bessel function of the first kind: $J_1(x) = 0$ for $x \in \langle 0, 20]$, see:
`www.basilisk.fr/sandbox/Antoonvh/root-finding.c`
The results are shown in the top figure. Here the function $(J_1(x))$ was only evaluated 368 times in order to obtain an estimate as accurate as with the 'brute force' equidistant resolution of $N = 524288$.

For further info on numerical root finding in practice, see: `reference.wolfram.com/language/tutorial/EquationsInOneVariable.html`

7

Summary

Weather and climate influence life in many ways; varying climatic conditions can be associated with varying human cultures and on a day-to-day basis, the weather influences our plans and mood. As such, a proper prediction of the weather is of great importance. Ultimately, the weather is fueled by solar irradiation, which changes sharply over the course of the day. The relative position of the sun is directly influencing the meteorological properties in the atmosphere closest to the surface. The atmospheric state in the lowest few kilometers, known as the troposphere, is therefore characterized by a daily cycle: during daytime, the sun heats the air and at night, the atmosphere typically cools down and the wind settles a bit.

In spite of its omnipresence and importance, this diurnal cycle in weather patterns is still not fully understood by the meteorological community. Consequently, it is also hard to describe and predict the weather properly. The challenges emerge from the fact that the weather is continuously evolving, and is therefore never 'in balance', which would simplify analysis of the processes. With the goal to better understand the 24-hour weather cycle, this book addresses the following topics:

1. We present a proof-of-concept for the adaptive mesh refinement method applied to atmospheric boundary-layer simulations. Such a method may form an attractive alternative to static grids for studies on atmospheric flows that have a high degree of scale separation in space and/or time. Examples include the diurnal cycle and a convective boundary layer capped by a strong inversion. For such cases, large-eddy simulations using regular grids often have to rely on a subgrid-scale closure for the most challenging regions in the spatial and/or temporal domain. In Chapt. 2 we analyze a flow configuration that describes the growth and subsequent decay of a convective boundary layer using direct numerical simulation (DNS). We validate the obtained results and benchmark the performance of the adaptive solver against two runs using fixed regular grids. It appears that the adaptive-mesh algorithm is able to coarsen and refine the grid dynamically whilst maintaining an accurate solution. In particular, during the initial growth of the convective boundary layer a high resolution is required compared to the subsequent stage of decaying turbulence. More specifically, the number of grid cells varies by two orders of magnitude (!) over the course of the simulation. For this specific (DNS) case, the adaptive solver was not yet more efficient than the more traditional solver that is dedicated to these types of flows. However, the overall analysis shows that the method has a clear potential for numerical investigations of the most challenging atmospheric cases.

2. It is well known that the representation of certain atmospheric conditions in climate and weather models can still suffer from the limited grid resolution that is facilitated by modern-day computer systems. Herein we study a simple one-dimensional analogy to those models by using a Single-Column Model description of the atmosphere. The model employs an adaptive Cartesian mesh that applies a high-resolution mesh only when and where it is required. The so-called adaptive-grid model is described and we report on our findings obtained for tests to evaluate the representation of the atmospheric boundary layer, based on the first two GABLS intercomparison cases. The analysis shows that the adaptive-grid algorithm is indeed able to dynamically coarsen and refine the numerical grid whilst maintaining an accurate solution. This is an interesting result as in reality, transitional dynamics (e.g. due to the diurnal cycle or due to changing synoptic conditions) are the rule rather than the exception.

3. We present a conceptual model for the diurnal cycle of the dry atmospheric boundary layer (ABL). It may serve as a framework for future numerical studies on the transitional dynamics that characterize the ABL over land. The conceptual model enables to define expressions for relevant physical scales as a function of the most prominent forcing parameters and the low degree of complexity facilitates a dimensionless description. This is useful to help generalize boundary-layer dynamics that occur on a diurnal timescale. Further, the model's application for numerical studies is illustrated herein with two examples: A single-column-model study which assesses the effect of wind forcing on the main characteristics of the diurnal cycle, and a large-eddy-simulation study on the daily evolution of turbulence under weak-wind-forcing conditions. The results from these studies sketch the general evolution of the present set of diurnal-cycle systems in more detail. We discuss how the setups are able to reproduce well-known dynamical features of the ABL and also highlight limitations, where the simple conceptual system is unable to capture realistic ABL behavior. We conclude that the present conceptual model has an interesting balance between model-system complexity and physical realism, such that it is useful for future, idealized, studies on the diurnal cycle of the ABL.

Further, this book presents an *entr'acte* between each chapter. These sections serve as fun scientific and illustrative excursions on adaptive grid refinement.

Samenvatting

Weer en klimaat beïnvloeden het leven op talloze manieren; verschillende klimaat-zones hebben een sterk verband met de verschillende menselijke leefculturen en van dag-op-dag beïnvloedt het weer in grote mate onze plannen en ook onze gemoedstoestand. Een goede weersvoorspelling is daarom van groot belang. De energievoorziening van 'het weer' is afkomstig van de zonnestraling die de aarde bereikt. De zonnestand (zonnehoek) heeft direct invloed op de meteorologische eigenschappen van de atmosfeer nabij het aardoppervlak. De toestand van de atmosfeer is de onderste kilometers, ook wel de troposfeer genoemd, word gekenmerkt door een typische 'dagelijkse gang'. Het warmt op overdag en 's nacht koelt de lucht af en waait het wat minder.

Hoewel de dagelijkse gang van groot belang is voor de meteorologie, is er nog altijd onduidelijkheid over de exacte dynamica die ermee gemoeid is. Mede hierdoor blijft het accuraat voorspellen van het weer een uitdaging voor meteorologen. De moeilijkheid zit hem in het feit dat het weer zelfs op een dagelijkse tijdschaal voortdurend verandert. Hierdoor is het nooit sprake van balans, hetgeen een vereenvoudigde analyse verhindert. Met het doel om de 24-uur cyclus van het weer beter te doorgronden, presenteert dit boek de volgende onderwerpen:

1. We presenteren een 'principe bewijs' voor de adaptieve rekenrooster verfijnings-methode, toegepast op simulaties van de atmosferische grenslaag. Een dergelijke methodiek kan een interessant alternatief zijn voor de gangbare statische reken-roosters voor het bestuderen van problemen die gekenmerkt worden door een hoge mate van schaal separatie in de ruimte en/of de tijd. Voorbeeld hiervan is de opbouw (en neergang) van de zogenaamde convectieve grenslaag, waarbij zich een sterke temperatuursinversie aan de top bevindt. Voor dergelijke scenario's, waarbij brute-force berekeningen haast uitgesloten zijn, moeten "Grote-Wervel-Simulaties" noodzakelijkerwijs volledig vertrouwen op parameterizaties van de kleinschalige processen in de meest uitdagende regionen van het ruimtelijke en tijds domein. Voor een adaptief rooster geldt dat in veel mindere mate.

   We analyseren een configuratie die de groei en het daaropvolgende verval van een convectieve grenslaag beschrijft, gebruik makend van directe numerieke simulatie (DNS). We valideren de resultaten van het adaptive model en confronteren de efficiëntie tegen resultaten verkregen met een regulier rekenrooster, dat zowel gelijkmatig als statisch is. Het blijkt dat het adaptieve algoritme in staat is om het rekenrooster dynamisch te verfijnen en vergroven, terwijl een accurate oplossing gehandhaafd blijft. Gedurende de initiële groei van de grenslaag is een relatief hoge resolutie vereist ten opzichte van de fase waarin de convective tur-

bulentie uitsterft. Over de totale simulatie varieert het aantal roosterelementen wel met een factor honderd! Desalniettemin, bleek, voor dit specifieke (DNS) scenario de adaptieve methode nog niet efficiënter dan de traditionele methode die is toegespitst of dit type problemen. Echter, de complete analyse laat zien dat de adaptieve methode duidelijk potentie heeft voor toekomstig numeriek onderzoek naar de meest uitdagende atmosferische systemen.

2. Het is wel bekend dat de representatie van bepaalde atmosferische condities in weer en klimaat modellen te lijden heeft onder de beperkingen (en eindigheid) in rekenresolutie, waarmee we met moderne supercomputers te maken hebben. We bestuderen een simpele, één dimensionale analogie voor dergelijke modellen, door gebruik te maken van een één-kolomsbeschrijving van de atmosfeer. Het model past een adaptief rekenrooster toe dat enkel een hoge resolutie toepast waar en wanneer dit nodig is. We presenteren de details van het model en rapporteren onze bevindingen voor twee vergelijkingsstudies. Deze studies evalueren de representatie van de atmospherische grenslaag met het scenario volgens de zogenaamde GABLS configuraties. Dit zijn twee benchmark cases die goed beschreven zijn in de literatuur. De analyse toont aan dat de adaptieve methode inderdaad in staat is om het rekenrooster dynamisch te vergroven en verfijnen, en zorgt ervoor dat de oplossing over het hele tuid-ruimte domain accuraat berekend wordt. Dit is een interessant resultaat omdat in de werkelijkheid, transitie-dynamica (zoals bijv. de dagelijkse gang of veranderende synoptische condities) meer de regel zijn in plaats van een uitzondering in de natuur.

3. In Hoofdstuk 4 presenteren we een conceptueel model voor de dagelijkse gang van de atmosferische grenslaag. Het model kan dienst doen als een raamwerk voor toekomstige studies naar de transitie dynamica. Het conceptuele model faciliteert het definiëren van relevante lengte en temperatuur schalen als een functie van de meest belangrijke forceringsmechanismen. Verder maakt de eenvoud van het model het mogelijk om het systeem te non-dimensionaliseren, waarmee de resultaten gegeneraliseerd worden. Het gebruik van het model als raamwerk voor numerieke studies word geïllustreerd met twee voorbeelden: een studie naar het effect van de wind forcering op de dagelijkse dynamica, gebruikmakende van een éénkoloms model en een grote-wervel-simulatie studie naar de evolutie van de turbulente structuren. We bespreken hoe het simpele systeem in staat is om de werkelijkheid te vatten. Daarnaast worden ook tekortkomingen onder de loep genomen. De conclusie is dat het conceptuele model een interessante balans weet te vinden tussen fysisch realisme en complexiteit, zodanig dat het dienst kan doen in toekomstige studies naar de dagelijkse gang van de atmosferische grenslaag.

Tenslotte bevat dit boek tussen ieder hoofdstuk een *entr'acte*. Deze dienen als leuke, illustratieve excursies met adaptieve gridverfijning als rode draad tussen de onderwerpen.

Perhaps some day in the dim future it will be possible to advance the computations faster than the weather advances.

L.F. Richardson (1922)

1 | Introduction

1.1 Numerical weather prediction

Accurate prediction of the weather is of great societal and economic importance, but meteorologist face a challenging task due to the complexity and chaotic nature of geophysical flows. In the year 1922, Lewy Fry Richardson was the first attempting to make a weather prediction based on the equations that describe the evolution of the atmospheric state (Richardson, 1922). He solved a system of discretized equations for air motion and thermodynamics, but found out the model predictions were inaccurate and, in some aspects, even nonphysical. Richardson's results and experiences indicated the challenges that the approach faced. Almost a century later, numerical weather prediction lies at the center of meteorological forecasts and the so-called 'skill score' of these models has been continuously increasing (Bauer et al., 2015). The actual improvement of our weather forecast results from progress made in various sub fields in research as well as from the complex interplay between those fields. Here we mention a few important developments, that contributed to the overall success of current day weather forecast.

1. Our level of understanding regarding the atmospheric structure and the relevant processes has increased.

2. The availability of Meteorological data has improved. For example, data from global-coverage satellites facilitate accurate model assimilation/nudging.

3. The computational resources have greatly increased, allowing to solve more complex physical processes with greater accuracy.

4. Advances in numerical methods and computer science allow us to use the available computational resources more effectively.

Each of these four topics represents a field of research in itself and in this book we aim to add to subcategories of both the first and the fourth point. More specifically, we investigate the dynamical behavior of the atmospheric boundary layer within a diurnal cycle and study a possible avenue for more efficient modeling via the employment of adaptive grids.

1.2 The research in this book

Chapters 2, 3 and 4 form the body of this book and are based on peer-reviewed articles. Furthermore, they appear in chronological order. As such, the chapters may not necessarily connect in the most optimal manner. To alleviate this issue, this introduction chapter aims to provide an overview and discusses how the chapters are linked to each other, even tough they may be read in 'stand alone' mode, each with separate introduction and conclusion sections.

The common denominator between the chapters in this book is the usage of *adaptive grids* for the *numerical modeling* of the *diurnal cycle* of the *atmospheric boundary layer*. This sentence warrants the introduction of some concepts: The *atmospheric boundary layer* is the lowest part of the atmosphere, and is directly influenced by the processes that take place at the surface. Here the atmosphere exchanges heat, momentum and moisture with the underlying soil, and these quantities are mixed in the boundary layer, primarily through turbulent air motion. The surface also heats due to the incoming solar radiation, which typically drives thermal convection in the atmosphere. During the nighttime, it may cool due to the emission of long-wave radiation. A thorough understanding of the governing processes for its accurate representation in weather models is desirable for its omnipresence in local weather patterns. However, the interplay between even the most dominant processes of the diurnal cycle are not well understood (Lothon et al., 2014; Baas et al., 2017). A possible avenue to study such complex systems is with the use of *turbulence-resolving models*. With respect to a full weather model, such a research model reduces the level of complexity, and enables to study an idealized system. The obtained data is complementary to those from field experiments as turbulence-resolving models provide improved control over the forcings, yield detailed four-dimensional data (space and time), and facilitate simplifications to the system's forcing. Finally, the word *'adaptive'* refers to a detail of the numerical method and it is discussed with more depth in Sect 1.3.

The scope of the first two chapters is similar. Both investigate the potential of adaptive grids for the representation of highly dynamic atmospheric boundary layers in models. In Chapter 2, we motivate our wish to study the diurnal cycle with a three-dimensional turbulence resolving model in depth and argue that, compared to a static grid, an adaptive-grid approach is likely to be advantageous for this purpose. The focus is on the ability of an adaptive solver to accurately resolve the growth and decay of atmospheric convection-driven turbulence. Chapter 3 experiments with the idea that the same adaptive-grid philosophy may also be applied to weather models. This Chapter therefore employs a one-dimensional column model and focuses on the representation of the atmospheric boundary layer. It serves as a toy model for a future adaptive weather model. Chapter 4 introduces an idealized model scenario that could be used for studies on the diurnal cycle. The case aims to balance physical realism and model-system complexity. It hence may form a possible framework for detailed studies on the diurnal cycle. This chapter also includes results obtained with both turbulence-resolving methods and a single-column model. Chapter 5 presents a short note on the emergence of sharp temperature fronts. The conclusion of these chapters are summarized in Chapter 6. Further, between of each chapter, an short excursion is taken. These serve as 'mere' scientific fun, but also illustrate the broad applicability of the adaptive grid approach.

1.3   On adaptive-grid methods

Since the first usage of digital systems for scientific computing, researchers have pushed the available computational hardware to their limits. An elegant idea to increase the capabilities of existing computer systems and numerical methods is to optimize the computational mesh used for computations. This can be achieved by using a high resolution only for the regions where it is most required, and use coarser elements where the solution is more smooth in space. As such, a grid may be pre-tuned for a specific problem based on existing knowledge, *or*, the grid can be refined and coarsened *adaptively* as the solution evolves over timed based on an automatic algorithm. For the latter case, we speak of an adaptive grid approach, and the accompanying concepts will be further discussed in this book.

Pioneering studies on the problem-specific grid optimization by e.g. Brandt (1977); Babuška and Rheinboldt (1979); Harten and Hyman (1983) inspired Marsha Berger to present her seminal works on adaptive numerical methods (Berger and Oliger, 1984; Berger and Colella, 1989). Here the local resolution varies adaptively, based on the evolution of the solution itself. The adaptive method has transformed into the modus operandi for various fields of research, e.g. in astrophysics and multi-phase flows and presently, ca. one-in-five articles in the journal of computational physics are published with the key words 'adaptive mesh'. Due to the multi-scale character of atmospheric flows, weather models were soon recognized as a prime candidate for the adaptive grid method. Notable early works include those of Skamarock et al. (1989); Dietachmayer and Droegemeier (1992); Skamarock and Klemp (1993) and the present state-of-the art of adaptive weather modeling may be represented by Bacon et al. (2000); Jablonowski et al. (2009) and Aechtner et al. (2015). However, the adoption of adaptive models has not percolated into true operational weather forecasting, but this might change in the upcoming future, when the method has matured in its full extend. In the next paragraph we will discuss why immediate practical implementation of adaptive grids in weather forecast models is not as trivial as it seems. As a comprehensive review on adaptive methods is beyond the scope of the introduction, we refer to Behrens (2007) for further background on this topic.

The conceptual advantages of adaptive methods are obvious; it focuses the available resources and require less a priori knowledge on resolution requirements. However, despite the vast amount of literature, a prominent question as 'do adaptive methods actually function properly?' remains surprisingly hard to answer for the general case. The issue is rooted in the fact that an adaptive method naturally carries *overhead* compared to the more simple static methods. In practice it appears that the scenarios with a high degree of localization in space and time are able to benefit from the adaptive approach. However, there is much freedom when implementing an adaptive code and it is hard to gauge the overhead when assessing the feasibility of a novel formulation. According to the author of this thesis, the adaptive-grid community has failed to present a critical review of the wealth of approaches it has come up with and present a distinction between the good from the inefficient concepts. Such a discussion is essential before adaptivity can be adopted by a broader community. As computational performance depends on many factors and deserves a dedicated study in itself, the current work focusses on physics in relation to adaptivity. In particular the potential of AMR for diurnal ABL simulations and analysis will be shown. As

turbulent length scales highly vary over the course of the day, this type of diurnal ABL simulations are notorious and known to be very challenging for regular fixed-grid computational methods. Therefore, the diurnal cycle of the ABL seems to be an interesting 'showcase' for adaptivity as a tool to study the underlying physics in more depth.

1.4   This book contains links to online locations

For work to be considered inside the realm of scientific research it is essential to provide a clear description of the used methods. This is especially true for studies relying on digitally generated data. For this book to remain legible and concise, the English language is used to inform the reader and this forms a challenge, since the methods are written in a computer programming language. Fortunately, the advent of the internet has provided academic researchers with a medium to conveniently share unambiguous descriptions of the used methods. To ensure that the results herein are reproducible and the methods unambiguous, the used computer code is documented and presented in clear formatting online. As such, the interested reader in encouraged to follow the links to the relevant online locations that are presented alongside the textual description in each chapter.
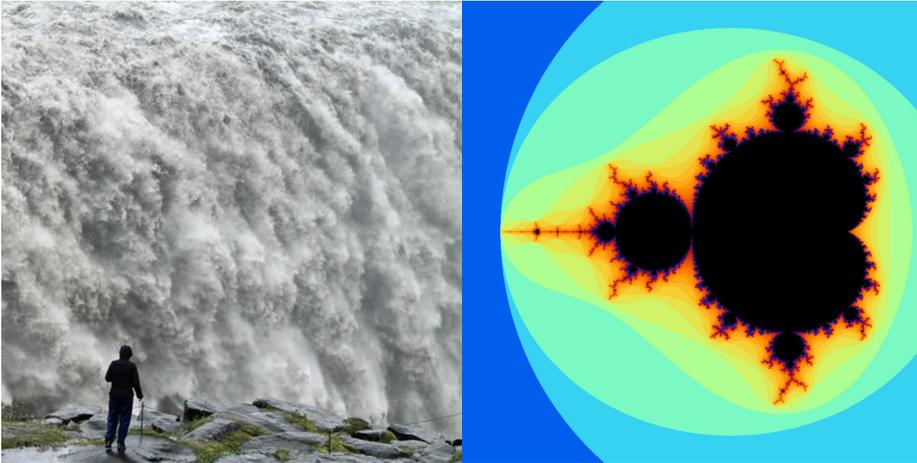
The natural beauty of the Detivoss water fall in Iceland (top left) may be rooted in the wide variety of length scales that can be observed. As a toy model for such fractals, Benoit B. Mandelbrot studied a sequence of complex numbers (c_n) first considered by Piérre Fatou, starting from c_0,

$$c_{n+1} = c_n^2 + c_0.$$

It can be shown that this sequence diverges in absolute sense when $\|c_n\| > 2$. The Mandelbrot set is defined as the set of numbers c_0 for which the sequence does not diverge when $n \to \infty$. A spectacular non-self-similar fractal pattern arises (top right) when we associate a color code to the number of iterations N it takes such that $\|c_N\| > 2$ for each pixel position (x, y), starting from $c_0 = x + iy$, with i the imaginary unit $(i = \sqrt{-1})$. The black area corresponds to the pixel-centered locations that did not diverge for $N = 1000$, and gives a good indication of the set. The color coding associates the logarithm of $N + 1$ with one of 128 different colors in the palette, from dark blue $(N = 0)$ to red/purple $(N = 1000)$.

To study the small-scale patterns in more detail, it is tempting to generate a high-resolution image. However, it seems reckless to search through the sequence for each individual pixel when the corresponding color code could be readily computed form a coarser grid via interpolation. As such, for each group of 2×2 points, we compute N_{coarse} based on the group's averaged location and check how well the interpolation from the local coarser resolution approximates the original color-code values. When this difference is larger than a single-color code, there appears to be non-trivial spatial features and a point can be split up into 2×2 points at double the resolution. Starting from a coarse 2×2 points grid, this process is repeated until a desired maximum resolution, keeping the coarse grid values when it is sufficient. Once the computations stop, an image at the maximum resolution is generated, using bilinear interpolation for the 'up sampling' of the coarse grid points. The resulting quadtree-grid points for the

512×512 pixel image is shown below (left). If we wish to further increase the resolution, a certain, non-obvious, fraction of the domain will be refined. As such, we count the number of points used for images at increasing resolutions, and the results are plotted in the figure below (right). It appears that the required points scale favorably compared to the number of pixels. Meaning that the relative gain of using the adaptive grid increases as the scale separation increases.

This facilitated to generate an image with $131,072^2$ pixels. It may be explored on the '*easyzoom*' website. The exact implementations rely on the Basilisk quadtree toolbox, are documented and made freely available.

Explore the 16 Gigapixel-Mandelbrot-set rendering:
`https://easyzoom.com/image/109963`
The used Computer code in Basilisk's C progamming language:
`http://www.basilisk.fr/sandbox/Antoonvh/mandelbrot3.c`
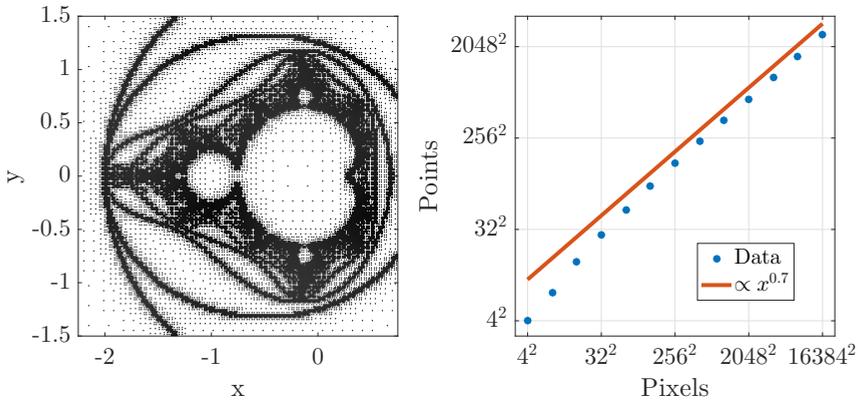
> *Even the smallest computational errors overwhelm numerical trajectories in typical simulations [...] Consequently, accuracy is expected only in a statistical sense.*
>
> V.A. Van Liebergen (2015)

2 | Towards Adaptive Grids for Atmospheric Boundary-Layer Simulations

Abstract

We present a proof-of-concept for the adaptive mesh refinement method applied to atmospheric boundary-layer simulations. Such a method may form an attractive alternative to static grids for studies on atmospheric flows that have a high degree of scale separation in space and/or time. Examples include the diurnal cycle and a convective boundary layer capped by a strong inversion. For such cases, large-eddy simulations using regular grids often have to rely on a subgrid-scale closure for the most challenging regions in the spatial and/or temporal domain. Here we analyze a flow configuration that describes the growth and subsequent decay of a convective boundary layer using direct numerical simulation (DNS). We validate the obtained results and benchmark the performance of the adaptive solver against two runs using fixed regular grids. It appears that the adaptive-mesh algorithm is able to coarsen and refine the grid dynamically whilst maintaining an accurate solution. In particular, during the initial growth of the convective boundary layer a high resolution is required compared to the subsequent stage of decaying turbulence. More specifically, the number of grid cells varies by two orders of magnitude over the course of the simulation. For this specific (DNS) case, the adaptive solver was not yet more efficient than the more traditional solver that is dedicated to these types of flows. However, the overall analysis shows that the method has a clear potential for numerical investigations of the most challenging atmospheric cases.

2.1 Introduction

The aim of the present work is to introduce adaptive mesh refinement (AMR) as an efficient tool for numerical investigations of the atmospheric boundary layer (ABL) using turbulence resolving methods. This refers typically to models that rely on direct numerical simulation (DNS) or large-eddy simulation (LES) techniques. In general, AMR solvers aim to distribute the available computational resources efficiently over a domain by dynamically refining and coarsening the computational grid in space and time. AMR techniques have successfully been employed in studies concerning flows with a high degree of scale separation throughout the spatial and/or temporal domain. Such studies concern a wide range of topics, e.g. cosmological hydrodynamics (Teyssier 2002), electro hydrodynamics (López-Herrera et al. 2011), multiphase flows (Fuster et al. 2009), flows in complex geometries (Popinet 2003) and turbulence simulations (Schneider and Vasilyev 2010). However, to our knowledge, the potential of this technique has not yet been explored for ABL research, and here we aim to do so through an investigation of the consecutive growth and decay of a convective boundary-layer (CBL) system. The flow configuration is modelled after Van Heerwaarden and Mellado (2016) who performed an in-depth study of this case using a regular grid configuration. As such, the AMR method is tested and benchmarked.

Several methods that meet a varying resolution requirement throughout the spatial domain have already been successfully applied in studies on ABL turbulence. For example, stretching and squeezing of grids (see e.g. Heus et al. 2011, Van Heerwaarden and Mellado 2016, De Roode et al. 2016), nested grids (see e.g. Sullivan et al. 1996, 1998, Moeng et al. 2007, Mirocha et al. 2013, Muñoz-Esparza et al. 2014) and the usage of unstructured anisotropic grids. However, the mesh is always kept fixed during the simulation, whereas dynamical changes in the ABL call for variation of resolution in time. Furthermore, the aforementioned methods of refinement need to be predefined. Consequently, detailed a priori knowledge is needed on the varying resolution requirement throughout the spatial domain. Apart from tailored and well-known cases, this knowledge is usually not available beforehand; therefore, we identify three favourable characteristics of an AMR approach for ABL studies. First, the resolution can vary throughout the spatial domain. Second, the grid can vary in time such that temporal variation in the local resolution requirement can be met. Third, the grid is generated adaptively based on the evolution of the numerical solution itself, relaxing the requirement of detailed a priori knowledge on the resolution requirement.

To illustrate our philosophy, we briefly discuss a textbook example of the evolution of the ABL during a diurnal cycle (after Stull 1988). Figure 2.1 depicts a typical evolution of the ABL during a diurnal cycle. Around sunrise the solar irradiation of the Earth's surface causes a thermal instability that results in the rapid growth of a CBL. The typical size of the largest thermal plumes scales with the boundary-layer height and hence there is a temporal dependency on the resolution requirement to resolve these turbulent structures. The growth of the boundary layer slows down when the rising thermals reach the inversion layer, which effectively caps turbulent structures at the top of the CBL. The dynamics within an inversion layer are of pivotal importance for the evolution of the CBL (Garcia and Mellado 2014). Apart from the effective 'lid' on the boundary layer, entrainment processes occur here and
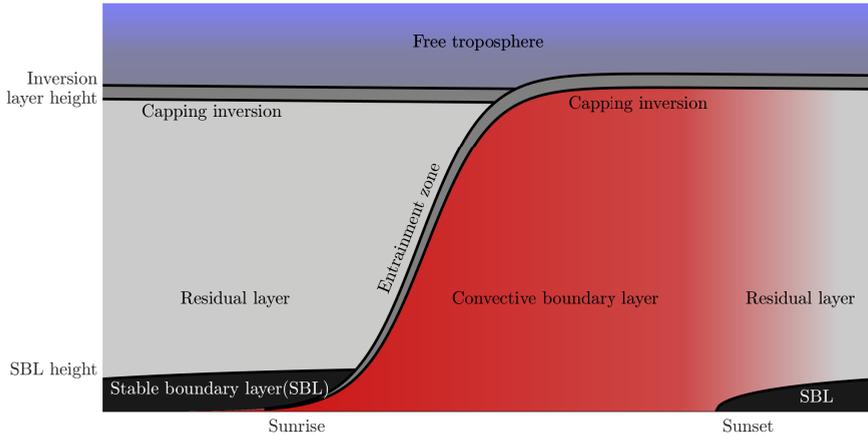
Figure 2.1: Sketch of a prototypical diurnal cycle evolution. Adapted from Stull (1988).

the formation of stratocumulus clouds is promoted by the large jump in temperature with height. Due to the presence of strong stable stratification, turbulent length scales are suppressed (De Lozar and Mellado 2015), and in order to resolve the most prominent turbulent structures here, a much higher resolution is necessary compared to the bulk of the CBL (Sullivan and Patton 2011, De Lozar and Mellado 2015). Applying such high resolution everywhere in the domain is not feasible given the current status of computational resources, and might not be feasible in coming years (Bou-Zeid 2015). For this reason, many LES studies have to rely on their subgrid-scale (SGS) parametrizations within the region of the inversion layer, partially negating the purpose of a turbulence resolving study. Furthermore, the exact height and strength of the inversion layer are not always known a priori (except in cases that have been studied before). Fixed nested grids (Sullivan et al. 1998) are thus not always flexible enough to capture the dynamics properly. On the other hand, practically speaking, it should be noted that LES results between various studies often tend to converge, signifying that SGS models have appreciable skill in describing certain characteristics of the inversion layer (see e.g Nieuwstadt et al. 1993, Siebesma et al. 2003).

At the approach of sunset, thermal plumes gradually decay into so-called residual turbulence, and due to the radiative cooling of the Earth's surface, stable stratification sets in and turbulence is now driven by wind shear only. The stable boundary layer (SBL) is typically much shallower than the CBL and, furthermore, the length scales of the turbulent structures that account for the mixing of heat and momentum within this layer are only a fraction of the size of those associated with daytime convective turbulence (Basu et al. 2008). Additionally, Ansorge and Mellado (2016) argue that the resolution requirement for their simulations of the intermittently turbulent SBL is dictated by localized dissipative flow structures that only encompass a fraction of the computational domain.

Rather than capturing the cyclic behaviour of the atmosphere as depicted in Fig. 2.1, the contrast between daytime and night-time turbulence has resulted in many

numerical studies focusing only on either convective or stable conditions. The studies that do simulate a diurnal cycle typically struggle to resolve turbulence during the night (Kumar et al. 2006, Basu et al. 2008, Abkar et al. 2015). Furthermore, the transition period itself (i.e. around sunset) would benefit from high fidelity numerical studies (Lothon et al. 2014). In summary: the example shows that the intrinsic dynamic character of the ABL calls for flexible techniques such as an AMR appoach in addition to existing techniques that have successfully been applied to studies on idealized, steady cases.

Apart from our long-term prospects, we focus here on a case corresponding to the red and grey sections in Fig. 2.1. This choice is motivated by the fact that as a first step, we would like to present a proof-of-concept of the AMR approach before we redirect our attention towards more challenging cases. Therefore, we present results obtained with DNS, for which all turbulent structures are resolved explicitly down to the small-scale Kolmogorov length (i.e. the viscous length scale) according to the Navier-Stokes equations, without any closure for turbulence. Compared to, for example, LES, the results obtained with DNS should be independent of the numerical formulations or choice of any SGS model, whereas with LES this is a topic of discussion (Bretherton et al. 1999, Siebesma et al. 2003, Fedorovich et al. 2004, Beare et al.2006, De Roode et al. 2017). However, as shown in Sect. 2.4, the concept of the AMR approach can be easily extended to LES. Since this technique is a popular choice for studies on the ABL, we also briefly discuss results obtained with the AMR technique using a LES formulation.

We realize that we cannot address all questions regarding the AMR technique in relation to ABL simulations. For example, here we focus on a single case whereas we will argue that the performance of an AMR solver varies depending on the particular case specifications (see Appendix 1). Furthermore, we choose a numerical solver called Basilisk (`http://basilisk.fr`) for the adaptive-grid runs and do not assess alternatives.

The paper is organized as follows; in Sect. 2.1 the details of the adaptive-grid solver are described, focusing on the AMR algorithm, and in addition, Sect. 2.2 provides an example analysis of how the algorithm assesses a turbulent signal and adapts the grid accordingly. In Sect. 2.3 the case and the numerical set-up of the different runs are specified. Section 3 presents the obtained results including a performance assessment, while in Sect. 4 we provide an outlook on future plans. We finish with a conclusion combined with a discussion in Sect. 5. Additionally, using a simple flow set-up, Appendix 1 illustrates an important advantage the AMR technique has over a fixed equidistant-grid approach.

2.2 Methods

2.2.1 Basilisk and the Grid Adaptation Algorithm

The AMR runs are performed with the partial-differential-equation solver called Basilisk, a code that contains a second-order accurate finite-volume solver for the Navier-Stokes equations. For a detailed description of the numerical formulations see Popinet (2003,2009), Lagrée et al. (2011), and references therein. In order to facilitate local adaptive refinement and coarsening whilst maintaining a Cartesian

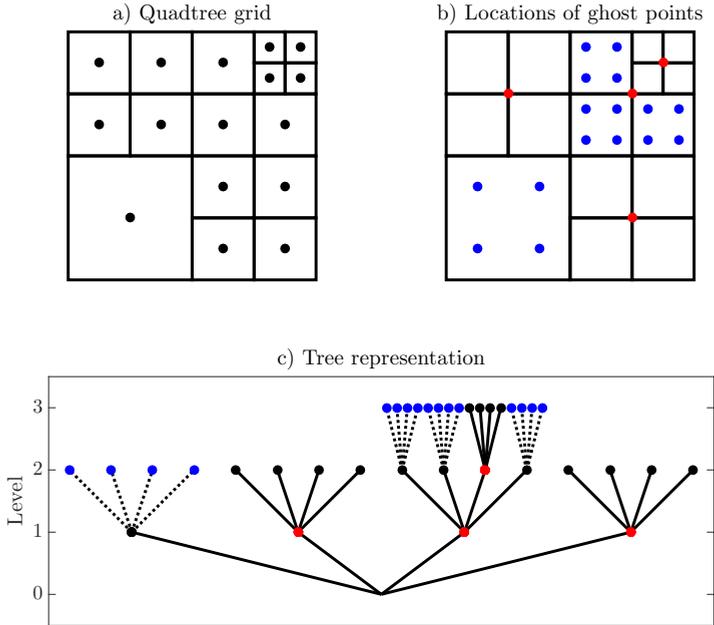a) Quadtree grid   b) Locations of ghost points

c) Tree representation

Figure 2.2: Example of a tree-grid structure. The top row presents the spatial structure of the grid cells with varying levels of refinement (a) and the locations of two types of ghost points whose field values are defined by the downsampling (red dots) and upsampling (blue dots) operations (b, see text). The plot on the bottom row presents a corresponding tree representation of the various grid cells and ghost points at different levels (c).

grid-structure, a so-called tree-based grid is used. To illustrate this mesh structure, Fig. 2.2 shows the two-dimensional (2D) variant of a tree-based grid (i.e. a quadtree), whose structure introduces a hierarchy between cells at integer levels of refinement. The resolution between the levels of refinement differs by a factor of two and the Basilisk solver allows neighbouring cells to vary up to one level. The formulations of numerical methods (e.g. evaluating spatial derivatives) on equidistant Cartesian grids are relatively straightforward compared to their uneven grid counterparts. Therefore, ghost points are defined, enabling simple Cartesian stencil operations for the cells in the vicinity of a resolution boundary. These points act as virtual cells and are located such that all cells have neighbours that are defined at the same level of refinement, see Fig. 2.2b. The field values on these ghost cells are defined with interpolation techniques using the original field values.

The tree grid facilitates an efficient and convenient structure to perform a multiresolution analysis of a discretized field. During the simulation, such an analysis is used to determine which grid cells require refinement and where in the domain cells can be coarsened. This procedure is discussed next. Consider a 1D signal (f) discretized with an even number (n) of elements f_n, where individual entries of f_n are indexed with i such that f_n^i represents the i-th entry of f_n. First, we define a
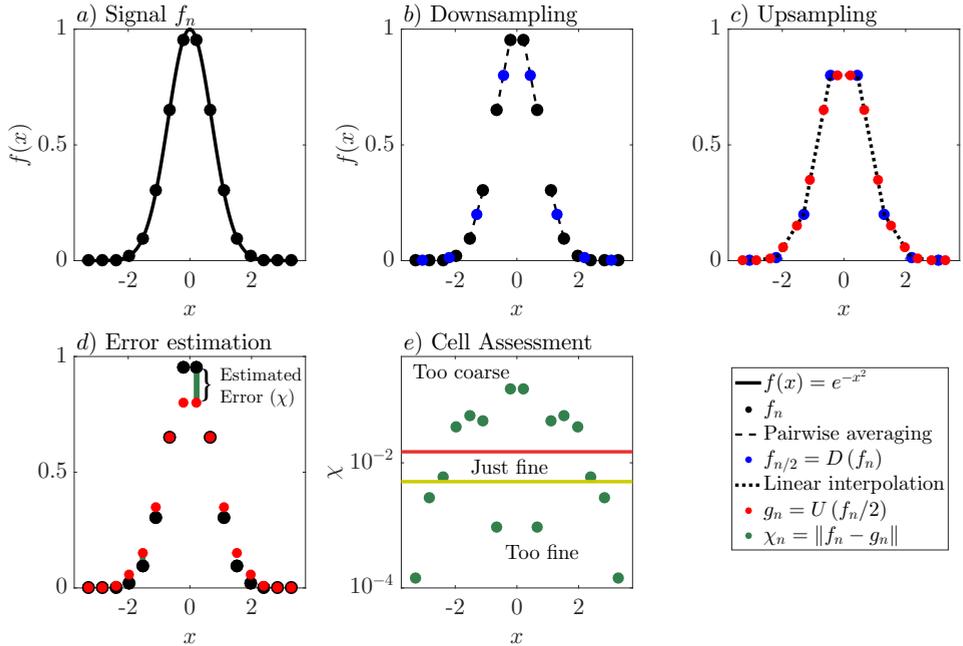
Figure 2.3: A one-dimensional, visual representation of how the adaptation algorithm assesses the discretization of a curved field $f(x)$: a) A coarser level estimate of the discretized solution is obtained using the downsampling operation. b) Using these coarse level values, the original discretized solution can be estimated using the upsampling operation. c) The difference between the estimated and original values is interpreted as an error estimator (χ) and can be compared against fixed thresholds (e.g. ζ). d) and e) If the refinement criterion is exceeded, new cells at one level higher are initialized locally by applying a linear interpolation technique using the initial cell values. Alternatively, if the estimated error is smaller than the coarsening criterion for multiple cells, these cells can be merged if that does not violate the general grid-structure requirements (see text and Fig. 2.2).

downsampling operation (D) that approximates f_n on a coarser level grid with $n/2$ elements,

$$f_{n/2} = D(f_n). \tag{2.1}$$

Second, we define an upsampling operator (U) that samples $f_{n/2}$ to a signal that is defined with the same element entries as the original signal f_n,

$$g_n = U(f_{n/2}), \tag{2.2}$$

noting that in general $f_n \neq g_n$, and the absolute difference χ, defined as,

$$\chi_n^i = \|f_n^i - g_n^i\|, \tag{2.3}$$

28

can be interpreted as an estimation of the discretization error. The downsampling operation in the Basilisk solver is defined as local volume averaging of the signal to obtain a value for a corresponding coarser-level grid cell (see Fig. 2.3 a.). This formulation is exact since in a finite-volume formulation, the grid cell values represent volume-averaged quantities. To be in line with the second-order accuracy of the solver, the upsampling operation is chosen to be second-order accurate as well, and entails performing a linear interpolation between the grid points of the coarse level solution (see Fig. 2.3b). Once these two operations have been applied to the discretized signal, it is possible to evaluate χ_n^i for each of the grid cells. Given an error threshold ζ, the following assessment with regards to a grid-cell's resolution can be made,

$$\text{the } i\text{-th grid cell is } \begin{cases} \text{too coarse.} & \chi_n^i > \zeta, \\ \text{too fine.} & \chi_n^i < \frac{2\zeta}{3}, \\ \text{just fine.} & \text{Otherwise.} \end{cases} \qquad (2.4)$$

The threshold on the estimated error for refinement ζ is called the refinement criterion, with ζ having the same physical units as f. Note that the described method is formally linked to wavelet thresholding that has already been employed for fluid dynamical simulations (Schneider and Vasilyev 2010). The grid can be refined and coarsened according to Eq. 2.4 and field values for the new refined and coarsened cells can be defined using an identical formulation as is used for the U and D operator, respectively. However, the Basilisk solver allows the formulations for upsampling and downsampling during the grid-resolution assessment and the actual refinement and coarsening of cells to differ.

In general, the tree grid that results from applying the adaptation algorithm results in the presence of the aforementioned resolution boundaries and accompanying ghost cells within the domain (see Fig. 2.2). To define the field values of ghost points, the Basilisk solver uses the downsampling and upsampling operations. The implementation is visually represented for a 1D scenario in Fig. 2.4. First, downsampling is used to define the field values of ghost points on the high-resolution side of a resolution boundary. Second, an upsampling method is used to define the field values of the ghost points on the coarse side of the resolution boundary. By using this method, the estimation error in the ghost cells' field values scales with ζ.

The formulations used for downsampling and upsampling as exemplified in Figs. 2.3 and 2.4 can be easily extended to two and three dimensions, for so-called quadtree and octree grids, respectively. In order to demonstrate the algorithm and the effect of different ζ values on the representation of a turbulent field, the next section shows the results of the algorithm applied to a slice of a 3D turbulent field.

The Basilisk solver can run in parallel on many processors by applying a domain decomposition using the Message Passing Interface (MPI). As the grid structure may change during a simulation run, an important issue is load-balancing; the decomposition of the domain between processors must then be modified as the grid is locally refined or coarsened. This is achieved in the Basilisk solver using the natural decomposition of a Z-ordering space-filling curve applied to the quad/octree structure (Griebel and Zumbusch 2001).
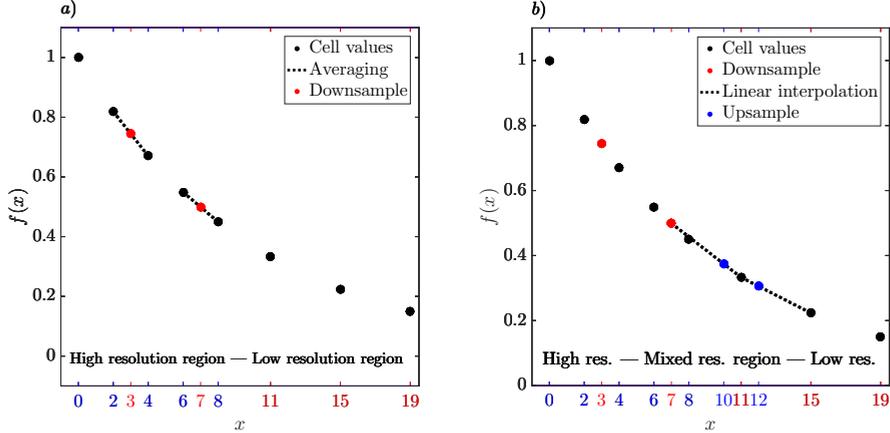
Figure 2.4: Example of the treatment of a resolution boundary in a one-dimensional scenario. First, the high level region near the resolution boundary is downsampled to obtain values for the coarse-level ghost points in red (a). Second, linear interpolation of the coarse level solution is used to define the field values of high level ghost points in blue (b).

2.2.2 An Example of the Adaptation Algorithm

This section aims to exemplify how the adaption algorithm assesses a discretized signal and adapts the grid according to a refinement criterion ζ. For this purpose, we apply the algorithm to a subset of the data from the simulation of forced isotropic turbulence in Li et al. (2008). The simulation is run using a fixed equidistant grid with 1024^3 nodes; in terms of the Kolmogorov length scale (η), the grid spacing (Δ_i) is $\Delta_i = 2.2\eta$. For the analysis we assume the data to be resolved well enough, and the results are kindly made available via the Johns Hopkins turbulence databases (http://turbulence.pha.jhu.edu/). We analyze a 2D slice of the data (i.e. 1024^2 cells) and for simplicity, we only consider the velocity component perpendicular to the sliced plane ($u_\perp$). The data are presented in Fig. 2.5a; using the algorithm described in Sect. 2.2.1, we can evaluate the χ field corresponding to the original $u_\perp$ field. A section of the resulting field, indicated by the black box in Fig. 2.5a, is shown in Fig. 2.5b, where we can clearly see that the estimated discretization error is not distributed uniformly by the equidistant-grid approach that was used in the simulation. Rather, it appears that there are anisotropic structures present, visualized by relatively high χ values (in yellow). These structures appear to correspond to vortex filaments that characterize the dissipative structures of high-Reynolds-number turbulence (Frisch, 1995). This result motivates the application of the grid refinement algorithm to the data sample shown. Note that we cannot 'add' new information by refinement and at this point we do not make any claims regarding what χ values are reasonable for a turbulence-resolving simulation (this will depend on the numerical formulations and is the topic of a future study). As such, we only allow the algorithm to coarsen the field with a maximum error threshold ζ (as defined in Eq. 2.4). The number of grid cells resulting from the application of the adaptation algorithm for a range of ζ values is

shown in Fig. 2.5c; as expected, the number of grid cells decreases with an increasing ζ value. Note that the plot also shows that even for the high ζ values, the grid still contains cells at the maximum resolution.

The main concept of employing the described grid-adaption algorithm is visualized in Fig.2.5d. Here histograms of the number of grid cells within 512 equally-spaced χ bins are presented for the original data and the data obtained from applying the grid adaptation technique with three different refinement criteria. It appears that for the original dataset, the histogram is monotonically decreasing with increasing χ. This shows that many grid cells exist where the numerical solution is relatively smooth compared to cells in the tail of the histogram. Hence, if the grid is chosen such that the discretization errors in the latter region do not affect the relevant statistics of the flow evolution, then the grid must be over-refined elsewhere. The histograms of the adapted grids show that the algorithm is able to lower the number of grid cells with low χ values, such that fewer grid cells are employed. Note that the grid coarsening does not introduce new grid cells with $\chi > 2\zeta/3$, as this part of the histogram remains unaltered.

When grid cells with a small but finite χ value are coarsened, some of the data are lost and in general cannot be exactly reconstructed by interpolation techniques (see Sect. 2.2.4). In order to assess how the data from the adapted grids compare with the original data, Fig. 2.5e presents the corresponding power spectra. It appears that none of the adapted grid data are able to exactly reproduce the original power spectrum; more specifically, with increasing ζ values, the wavenumbers (k) that show a significant deviation in $E(k)$ from the original appear to decrease. We would like to point out that in order to evaluate the spectrum we have linearly interpolated the data from the non-uniform grids to an equidistant grid with 1024×1024 data points. The choice of the interpolation technique is arbitrary and will pollute the diagnosed spectrum in a non-trivial manner. As such, we directly compare all 1024^2 $u_\perp(x, y)$ samples in Fig. 2.5f, where we see that the deviation of the data from the $1:1$ line is a function of ζ.

The example presented in Fig. 2.5 is meant to demonstrate the used adaptation algorithm. The following sections are dedicated to assessing its application to time-dependent numerical simulations of a turbulent field for an atmospheric case.

2.2.3 Physical Case Set-up

As indicated in the Introduction, we ran a DNS case from the referenced literature to validate, benchmark and exemplify the adaptive-grid approach. The cases from virtually all atmospheric-turbulence-resolving studies prescribe the periodicity of the solution in the horizontal directions. Unfortunately, at the time of writing, the Basilisk solver cannot yet handle an adaptive grid in combination with periodic boundaries. To circumvent this limitation, we limit ourselves to a case where there is no mean horizontal forcing such that we can apply a no-penetration boundary condition for the normal-velocity component at the lateral boundaries. This is supplemented with a Neumann-boundary condition for the tangential velocity components, pressure and buoyancy fields. We realize that this choice might affect the solution and therefore its impact is assessed by re-running the case using a fixed and regular grid with both sets of lateral boundary conditions (not shown). It appears that for the chosen set-
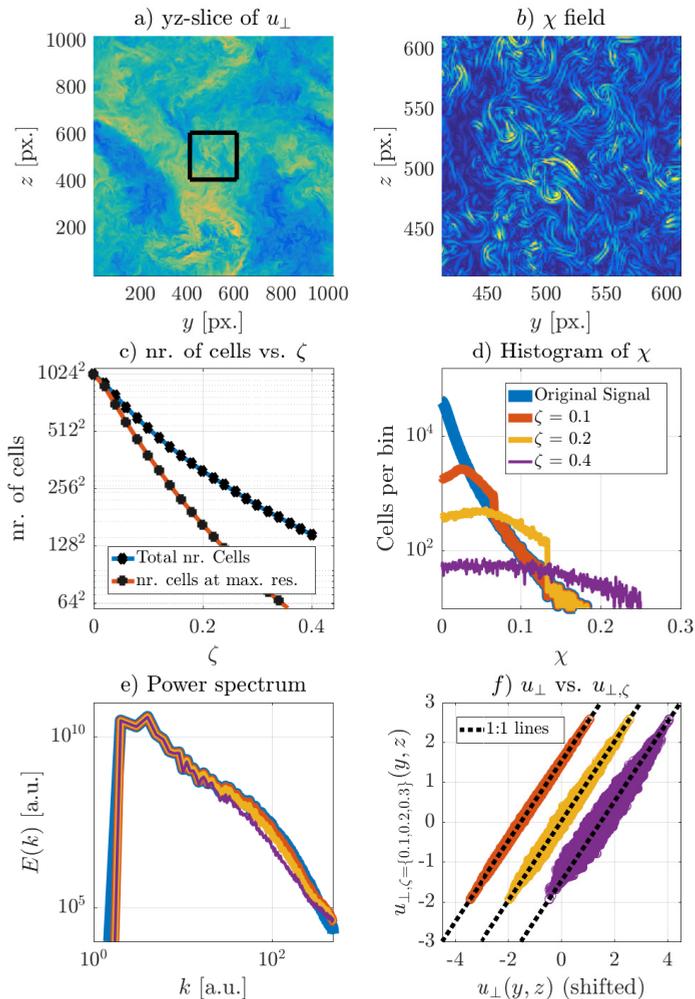
Figure 2.5: Example of the adaption algorithm applied to a (2D) slice of a 3D turbulent field. a) Shows the data slice of the velocity component in the plane-perpendicular direction ($u_\perp$, obtained from Li et al. (2008)). b) Presents the χ field, evaluated using the method described in Sect. 2.2.4. Only the centre part of the slice, indicated by the black box in (a), is shown to reveal the small scale details in this simulation. c) shows the grid cell number dependence on the chosen refinement criterion (ζ), note the logarithmic vertical axis. A histogram of the χ field with 512 bins for the original data, and the data corresponding to three ζ values are presented in d). Using the same colour coding as in d), power spectra and a direct comparison of the $u_\perp(y, z)$ field are shown in e) and f), respectively.
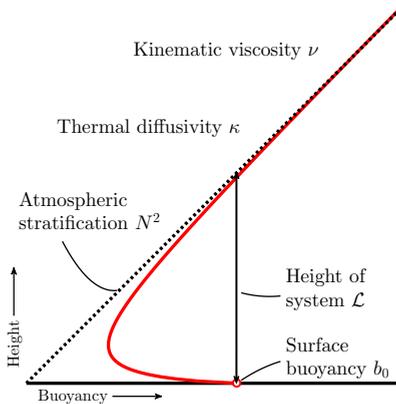
Figure 2.6: Sketch of the system and its parameters. The red line illustrates a typical buoyancy profile within the CBL during the initial development. Adapted from Van Heerwaarden and Mellado (2016).

up of the case, the simulation results are insensitive to the choice of the horizontal boundary conditions. Note that in future work, we will update the adaptive solver such that periodic boundary conditions can be combined with the AMR technique.

We study a case introduced by Van Heerwaarden and Mellado (2016) that was designed to investigate the growth and decay of a CBL. In Fig. 2.6 a schematic overview of the physical system is presented, and in their physical model a linearly stratified fluid at rest with kinematic viscosity (ν) and thermal diffusivity (κ) is heated from below by a surface with a constant temperature. For generality, buoyancy (b) is used as the thermodynamic variable. The buoyancy is related to the potential temperature (θ) according to;

$$b = \frac{g}{\theta_{\text{ref}}}(\theta - \theta_{\text{ref}}), \qquad (2.5)$$

where θ_{ref} is a reference potential temperature and g the acceleration due to gravity. The initial linear stratification is expressed as $b(z) = N^2 z$, where N^2 is the Brunt-Väisälä frequency associated with the initial stratification and z is the height above the surface. We assign a surface buoyancy b_0 larger than zero. Van Heerwaarden and Mellado (2016) identified relevant length, time, velocity fluctuation and buoyancy flux

scales, $\mathcal{L}, T, U$ and B, respectively, according to;

$$\mathcal{L} = \frac{b_0}{N^2}, \tag{2.6a}$$

$$T = \frac{b_0^{2/3}}{N^2 \kappa^{1/3}}, \tag{2.6b}$$

$$U = \frac{b_0^{7/9} \kappa^{1/9}}{N^{2/3}}, \tag{2.6c}$$

$$B = b_0^{4/3} \kappa^{1/3}, \tag{2.6d}$$

and are used to analyze the results in a non-dimensional framework. Two dimensionless groups can be identified that describe the system for any given set of $\{\nu, \kappa, N^2, b_0\}$,

$$Pr = \frac{\nu}{\kappa}, \tag{2.7a}$$

$$Re = \left(\frac{b_0^{4/3}}{\nu^{2/3} N^2} \right)^{4/3}, \tag{2.7b}$$

where Pr is the Prandtl number and Re is the Reynolds number. Note that for $Pr = 1$, the definition of the Reynolds number is consistent with $Re = U\mathcal{L}/\nu$.

2.2.4 Numerical Set-up and Formulation

For the evolution of the three velocity components (u_i), modified pressure (p) and buoyancy (b), the Navier-Stokes equations for an incompressible fluid are solved under the Boussinesq approximation, according to,

$$\frac{\partial u_i}{\partial t} + \frac{\partial u_j u_i}{\partial x_j} = -\frac{\partial p}{\partial x_i} + \nu \frac{\partial^2 u_i}{\partial x_i^2} + b\delta_{i3}, \tag{2.8}$$

$$\frac{\partial b}{\partial t} + \frac{\partial u_j b}{\partial x_j} = \kappa \frac{\partial^2 b}{\partial x_j^2}, \tag{2.9}$$

$$\frac{\partial u_j}{\partial x_j} = 0, \tag{2.10}$$

and with respect to no-slip and a fixed buoyancy (b_0) condition at the bottom boundary. At the top boundary, no-penetration with a free-slip condition is used and for the buoyancy, a fixed vertical gradient (N^2) is prescribed. Furthermore, a damping layer in the top 25% of the domain is active that damps buoyancy and velocity fluctuations to prevent the artificial reflection of gravity waves at the top boundary. The adaptive-grid runs are initialized with a grid at the minimum resolution that is locally refined to the maximum resolution near the bottom boundary (i.e. $z < \mathcal{L}/10$) before a random perturbation is added to the velocity components and buoyancy field in each grid cell.

Each integration timestep, grid adaptation is based on the estimated error (see Sect. 2.2.1) of the three velocity components, and the buoyancy field. For each

field a refinement criterion (ζ) is specified (ζ_{u_i}, ζ_b), where we non-dimensionalize the refinement criteria according to $\xi_b = \zeta_b b_0^{-1}$ and $\xi_{u_i} = \zeta_{u_i} U^{-1}$. In order to validate the results and assess the performance of the adaptive solver, we iteratively decrease the refinement criterion between runs whilst we limit the minimum grid-box size. This maximum resolution is inspired by Van Heerwaarden and Mellado (2016), and to limit the degrees of freedom, we choose; $\xi_{u_1} = \xi_{u_2} = \xi_{u_3} = 2.7 \times \xi_b$. We realize that this choice (based on trial and error) is rather arbitrary, as currently a solid framework of how the refinement criteria should be chosen is still lacking. The results are validated by a comparison with runs using a regular and fixed grid at the maximum resolution, performed with the Basilisk and MicroHH flow solvers: MicroHH is the numerical code used by Van Heerwaarden and Mellado (2016) to obtain their results. This code represents a state-of-the-art flow solver that is dedicated to studying atmospheric systems (Van Heerwaarden and Mellado 2016, Shapiro et al. 2016); for a detailed description of the MicroHH code see Van Heerwaarden et al. (2017). In addition, the fixed grid results of the Basilisk and MicroHH flow solvers are compared to each other.

We choose $Pr = 1$ and $Re = 3000$ with a domain size of $3\mathcal{L} \times 3\mathcal{L} \times 3\mathcal{L}$ and simulate the evolution of the system until the physical time $t = 45T$. In order to limit the computational costs, the evolution of the Basilisk-based run with a fixed regular grid is only computed until $t = 10T$. To illustrate the physical size of such a numerical experiment in reality; for a domain size of 0.5 m $\times$ 0.5 m $\times$ 0.5 m and $\theta_{\text{ref}} = 21\ ^oC$, the corresponding parameters are: $\mathcal{L} = 0.16$ m, $\theta_{\text{bottom}} = 36\ ^oC$ and $T = 153$ s. This could be interpreted as a modest laboratory experiment.

The simulations are performed with Surfsara's supercomputer Cartesius located in Amsterdam, The Netherlands (SURFsara 2017). An overview of the different runs, including the number of cores used, integration timesteps and total run time is listed in Table 2.1. Additional information on the case set-up for both models can be found at:
Basilisk:
basilisk.fr/sandbox/Antoonvh/freeconv.c
MicroHH:
github.com/microhh/microhh/tree/master/cases/vanheerwaarden2016

2.3 Results

2.3.1 Grid Structure

First, we study the evolution of the solution and grid structure qualitatively. Vertical slices of the magnitude of the gradient of the buoyancy field ($\|\nabla b\|$) and the used grid at $t = \{2, 10, 20\}T$ for run BA-0.0025 are presented in Fig. 2.7. At $t = 2T$ a complex grid structure is generated by the AMR algorithm, and within the ABL, the grid is refined at locations where vigorous turbulent structures are present. Above the ABL (i.e. $z/\mathcal{L} > 1$), turbulence is absent and the grid is coarse. Both effects are appealing from a physical perspective as the computations are focused on the regions where the activity is present. As the physical time progresses, the boundary layer becomes more neutrally stratified and the turbulence intensity decreases. And again, in response, the adaptive-grid algorithm has coarsened the grid at $t = 10T$. This

Table 2.1: Overview of the different simulation run details. In the top section a reference name, the used solver, grid type, the (maximal) numerical grid resolution, lateral boundary conditions and refinement criterion (ξ_b, if applicable) are listed for each run. In the bottom section the used number of cores, the total amount of integration steps taken at $t/T = \{10, 45\}$ and the total wall clock time of each run are presented.

Run name	Code	Grid	$n_x^2 \times n_z$ (Maximal)	Lateral BCs	ξ_b
MicroHH	MicroHH	Stretched	$512^2 \times 387$	Periodic	-
BA-512^3	Basilisk	Equi	512^3	Slip & No-pen.	-
BA-0.0025	Basilisk	AMR	512^3	Slip & No-pen.	0.0025
BA-0.005	Basilisk	AMR	512^3	Slip & No-pen.	0.005
BA-0.01	Basilisk	AMR	512^3	Slip & No-pen.	0.01

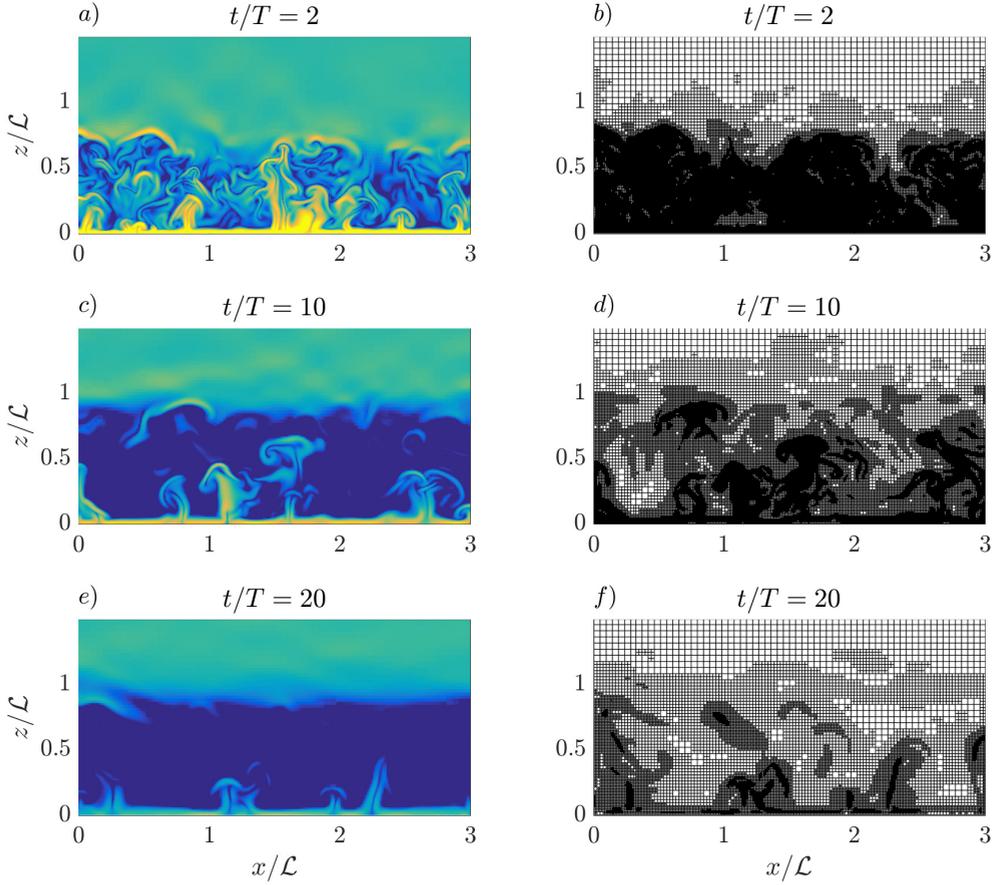| Run name	Number of cores	Integration steps at t/T = $\{10, 45\}$		total wall clock time (D:HH:MM)
MicroHH	64	$\{13920, 35670\}$		0:12:22
BA-512^3	64	$\{14073, (35670)\}$ *(estimated)*		2:16:12 ($t/T = 10$)
BA-0.0025	96	$\{14095, 30144\}$		2:10:30
BA-0.005	96	$\{14061, 28704\}$		1:18:19
BA-0.01	96	$\{14167, 25544\}$		1:02:16

Figure 2.7: Vertical slices of the $\|\nabla b\|$ field (left column) and the corresponding numerical grid (right column) in the lowest half of the domain. The top, middle and bottom rows represent snapshots taken at $t/T = \{2, 10, 20\}$, respectively. These snapshots are taken from the adaptive-grid run BA-0.0025.

remarkable effect is even more pronounced at $t = 20T$, where the coarsened regions have grown in size, indicating that the number of grid cells is decreasing over time. Physically speaking, this is facilitated by the fact that the size of the smallest eddies increases as turbulence decays.

2.3.2 Validation

Next we compare the results obtained with the AMR and fixed-uniform-grid runs. Following Van Heerwaarden and Mellado (2016), we compare the domain integrated quantities: a boundary-layer height z_i that is based on the buoyancy profile, kinetic energy I_e, buoyancy flux I_b and dissipation I_ϵ according to,

$$z_i = \frac{2}{N^2} \int^\infty (\langle b \rangle - N^2 z) \mathrm{d}z, \tag{2.11}$$

$$I_\alpha = \int^\infty \langle \alpha \rangle \mathrm{d}z, \tag{2.12}$$

where α is a dummy variable for $\{e, b, \epsilon\}$ and $\langle \alpha \rangle$ denotes the horizontally-averaged value of the quantity α. Figure 2.8a shows the evolution of the boundary-layer height, where good agreement between all simulations is found. The boundary-layer height is an integral measure for the amount of buoyancy (i.e. analogous to heat) in the system, though due to the case set-up, this integral quantity is not a very sensitive measure to assess the accuracy of the resolved turbulent motions. Therefore, we focus on higher-order statistics. In general, the evolution of the total kinetic energy shows similar behaviour between all runs (see Fig. 2.8). Nevertheless small discrepancies on the order of 5% are present, particularly between the runs with the adaptive grid and the fixed uniform grids, and as expected, this discrepancy decreases when the refinement criterion is more strict. In order to analyze the evolution of kinetic energy in further detail, Fig. 2.8c presents the evolution of the domain-integrated buoyancy flux, which represents the energy-production rate for this system. The buoyancy flux agrees well for all different runs and the observed differences between the runs are a result of turbulent fluctuations within the chaotic system rather than systematic discrepancies. This indicates that the overall structure and characteristics of the energy-producing motions are resolved accurately for all runs, and for free convection, these motions are associated with the large thermal plumes. In order to assess the representation of the small-scale structures in these simulations, Fig. 2.8d presents the evolution of the resolved energy-dissipation rate. Compared to the fixed-grid runs, the AMR-based runs slightly underestimate the resolved absolute dissipation, an aspect that is present throughout the simulation. Again, the discrepancy appears to be controlled by the refinement criterion, for which using stricter (i.e. smaller) criteria, the results seem to converge towards the values found with the fixed-grid runs. The fact that the runs diagnosed with a lower dissipation rate are also associated with lower kinetic energy indicates that a small part of the dissipation has a numerical/non-physical origin.

Figure 2.9 shows the vertical profiles of the kinetic energy at $t/T = \{2, 4, 25\}$, and shows discrepancies at $t/T = 2$ between all runs. The highly chaotic flow structure at this early stage of the simulation could explain some of the differences. However, consistent with Fig. 2.8b, the adaptive-grid runs show a systematically lower kinetic
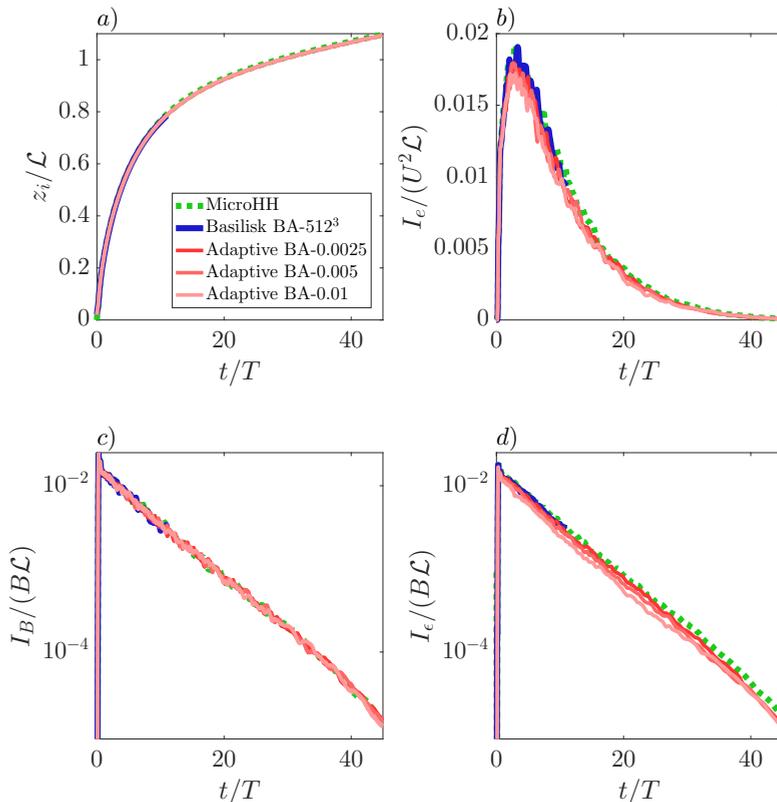
Figure 2.8: Time series of the domain integrated quantities, a) boundary-layer height (z_i), b) kinetic energy (I_e), c) buoyancy flux (I_B) and d) dissipation rate (I_ϵ) according to Eq. 2.11. The results are obtained with both Basilisk and MicroHH using fixed grids and Basilisk using the adaptive mesh refinement algorithm. Note that plots c) and d) use a logarithmic scale.

energy content over the entire domain. At $t/T = 4$, the profiles of the fixed-grid runs agree well, and furthermore, the energy found in the adaptive-grid run BA-0.0025 also compares well. It can be seen from the time series in Fig. 2.8b that for $t/T < 5$, the evolution of kinetic energy shows large fluctuations. Therefore, we also compare the energy profiles at $t/T = 25$, where we see again that the fixed-grid run still contains more energy than the adaptive-grid runs. Again, the adaptive run with the smallest refinement criterion is closest to the fixed-grid profile compared to the other adaptive-grid runs.

Although it appears that the adaptive-grid algorithm is able to refine the grid at locations of the turbulent structures, discrepancies in the simulations results remain present. This can be explained by the fact that the process of refining and coarsening the mesh relies on a linear interpolation strategy for defining values on new grid cells. This interpolation introduces additional errors compared to a simulation that employs a static grid, and these errors are similar to the truncation errors of fixed
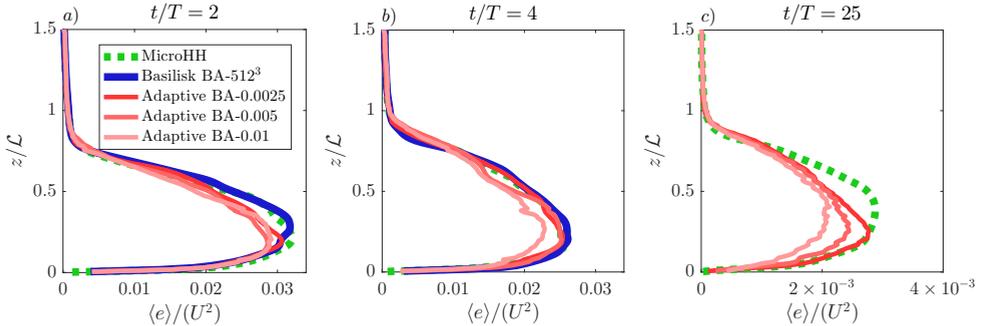
Figure 2.9: Vertical profiles of the horizontally-averaged kinetic energy ($\langle e \rangle$) at $t/T = \{2, 4, 25\}$ in left, middle and right plot, respectively. The results are obtained with both Basilisk and MicroHH using fixed grids and Basilisk using the adaptive mesh refinement algorithm. Note that in panel c) the horizontal axis is rescaled and that regular-grid computations with Basilisk are not available (see text, Sect. 2.2.4).

grid advection schemes and thus lead to similar additional numerical dissipation of energy. More accurate interpolation techniques could be tested to limit the error due to interpolation. Therefore, this relevant aspect will be studied in more detail in the future.

2.3.3 Performance

As discussed in the introduction, for highly dynamic flow configurations such as a diurnal cycle, model performance may benefit from the AMR approach. Although the present case of decaying convection is less dynamic than a full diurnal cycle, it is tempting to compare the simulation performance of the AMR-based run to its counterparts using a fixed and regular grid. Thereupon, several performance characteristics are presented in Fig. 2.10. Figure 2.10a shows, for the AMR-based runs, the evolution of the number of grid cells, that appear to be controlled by the refinement criterion, in which a smaller value causes the algorithm to use a more refined grid. As illustrated in the snapshots of Fig. 2.7, the number of grid cells varies significantly over the course of the simulation. Supposedly, the computational resources are distributed more efficiently over time. Furthermore, even in the run with the most strict refinement criterion, the number of grid cells does not exceed 21% of the maximum-resolution value. Figure 2.10b shows how the computational speed (i.e. defined here as wall clock time per integration timestep) is correlated with the number of grid cells. It appears that there are several regimes in how the performance is affected by the number of grid cells. For a large number of grid cells (i.e. $> 10^6$) the amount of integration timesteps per second increases with a decreasing number of grid cells, indicating that the solver does indeed speed up when the grid is coarsened. Note that the simulations apply many grid cells in the early stage of the runs (i.e. at the right-hand side of Fig. 2.10b and uses fewer cells as time progresses (towards the left-hand side of Fig. 2.10b). However, as denoted by the $x^{0.6}$-scaling line, in this regime the simulation speed is not linearly dependent on the amount of grid cells. Furthermore,
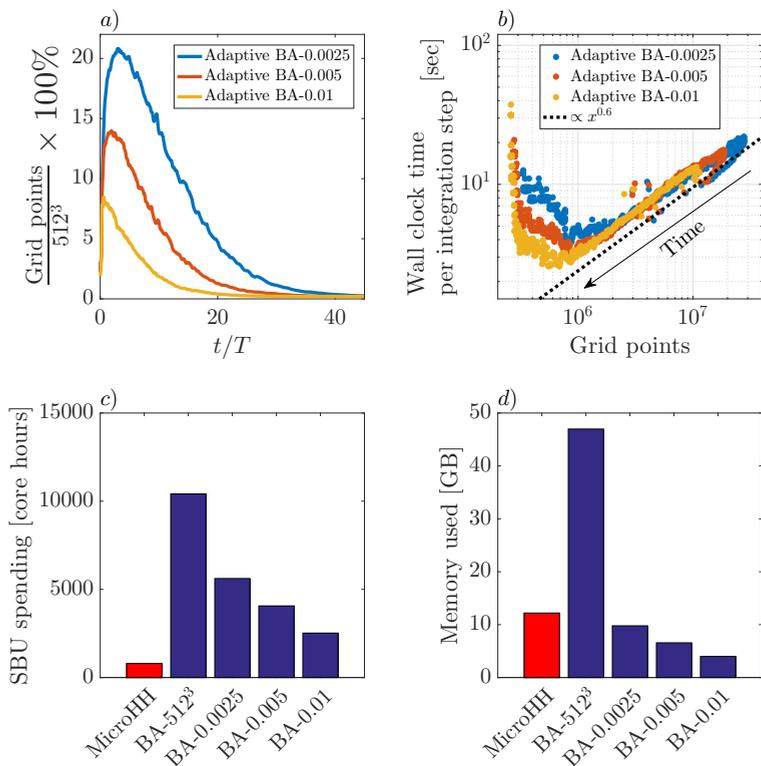
Figure 2.10: Overview of the performance characteristics of the adaptive and fixed-grid simulation runs. a) Time series of the number of grid points for the adaptive runs normalized by the maximum-resolution value (i.e. 512^3). b) Scatter plot of the wall clock time per integration step versus the used number of grid cells in the adaptive-grid runs. c) The total amount of System Billing Units (SBU, i.e. *number of cores × hours*) spending on each simulation run. Note that the value for BA-512^3 is estimated as if it were run until $t/T = 45$. d) The total RAM memory used in each simulation run in gigabytes (GB).

for lower number of grid points (i.e. $< 10^6$) the simulation speed appears to slow down when the simulation runs with fewer grid cells, i.e. there is a performance penalty for coarser grids! Possible causes for these performance characteristics are listed below:

1. For this case, the grid structure of the coarsened grids at later stages in the simulation contains a relatively larger fraction of resolution boundaries (see Fig. 2.7). These boundaries are associated with additional overhead as they require special attention by the solver (see Sect. 2.2.1).

2. The number of used processors (linked to domain decomposition for parallelization) is fixed throughout the simulations. Therefore, the relative overhead of MPI-domain communication routines compared to actual calculations increases as the number of grid cells decreases.

3. For coarse grids, the physical timestep taken per integration timestep increases (Courant-Friedrichs-Lewy criterion). Since diagnostic analysis of the solution is performed with a regular interval in the physical time, i.e. $\Delta t = T$ for profiles and slices and $\Delta t = T/20$ for the domain-integrated quantities. The frequency of calls to diagnostic routines increases (i.e. say, calls per 100 integration steps) on average resulting in an increased effort per integration step.

In Fig. 2.10c the amount of system billing units (i.e. the used $\#cores \times hours$) spending for the different runs is presented. Before an interpretation of the results is made, it is important to realize that the performance of a simulation run is a function of many aspects that ranges from the details of the hardware configuration to the exact case set-up. Therefore, the results presented here are intended as an illustration rather than as absolute values. Nevertheless, it is clear that the MicroHH run is notably cheaper compared to the runs performed with the Basilisk solver. This can be explained by the different numerical schemes that are employed. Most notably, for obtaining the pressure field, the Basilisk code uses a multigrid strategy for solving the corresponding Poisson equation whereas the isotropic-fixed grid in MicroHH facilitates the usage of a spectral Poisson solver. Although the spectral method requires more MPI communication for parallelization when using a large number of processors, it is known to be more efficient (Fornberg 1998). If we compare the adaptive and non-adaptive simulation runs performed with the Basilisk solver, we do see a considerable decrease in costs for the adaptive method runs.

In Fig. 2.10d the memory used for the different simulation runs is presented. Compared to the fixed-grid runs, the adaptive-grid runs require less memory. This is due to the fact that the maximum number of grid cells is considerably lower than the number of grid cells in the fixed-grid runs (see Fig. 2.10a). From this perspective, the adaptive-grid approach can also be attractive for applications where the available memory is limited. However, even though the run with MicroHH employs many more grid cells, the required memory is comparable to that of run BA-0.0025, meaning that per grid cell, the MicroHH code is more efficient in terms of memory.

2.4 Outlook: Towards Adaptive Mesh Refinement in Atmospheric LES

We have based our test and performance benchmark on an idealized flow configuration of a CBL using DNS, providing a ground truth for our intercomparison. In the future, we plan to study more practically-oriented cases by using an LES formulation. For many atmospheric cases, LES is preferred over DNS, because it provides an efficient tool for studying high-Reynolds-number flows. Therefore, the next step is to test the AMR approach in combination with an LES formulation. In this section, we briefly discuss some preliminary results on this topic. Because this is part of ongoing research, we do not perform a quantitative discussion of the test runs, the results and performance characteristics. The presented results aim to exemplify the AMR method for a different case and show the flexibility of the AMR approach. The example is based on the LES intercomparison study case by Bretherton et al. (1999), in which a boundary layer is filled with a smoke cloud that cools from the top due to longwave emission. The boundary layer is initially capped by a strong temperature inversion (i.e. 7 K over 50 m) at $z \approx 700$ m and rises over the course of the simulation due to entrainment. The inversion layer is identified as a region where turbulent length scales are suppressed and turbulent motions are anisotropic due to the stable stratification. As such, this region requires a high resolution to capture the predominant turbulent structures accurately. In constrast, the convective turbulence in the boundary layer itself can be captured on a relatively coarse grid (Sullivan and Patton 2011). Accordingly, we decide not to base the grid adaptation upon the estimated discretization error in the representation of the velocity-component fields, but only on the estimated error in the smoke-cloud fraction and temperature fields. With such an approach the AMR algorithm does not refine the mesh in order to resolve the small turbulent structures in the near-neutral boundary layer, but allows the LES to employ the SGS model effectively in this region. In this run, the numerical grid varies by three levels of refinement, i.e. between 25 m and 3.125 m. Figure 2.11 presents snapshots of the temperature and numerical grid taken at $t = 3$ h after initialization. It is clear from Fig. 2.11a that an inversion layer is present, while Fig. 2.11b shows that the numerical grid has a high resolution in the region of the inversion layer and remains coarse in the boundary layer itself. Furthermore, we see the subsiding shells in the boundary layer that are qualitatively similar to those observed in the laboratory experiment performed by Jonker and Jiménez (2014).

For this case, the AMR algorithm dynamically adapts to the flow by redirecting the grid refinement to those regions of the spatial domain where it is required. Hence in this case, adaptation is predominantly spatially focussed, whereas in the DNS case the refinement was most prominent in the temporal domain (see Fig. 2.10a). As such, both examples in this study are complementary and both effects (spatial and temporal adaptive grid refinement) are expected to play an important role in future simulations of full diurnal cycles (cf. Fig. 2.1).

Finally, we note the following; the present cases where restricted to spatially homogeneous set-ups, where 'scale separation' naturally occurs through the internal variability of turbulence, originating from the non-linearity of the governing equations. In reality, heterogeneity in the *surface boundary conditions* also becomes important
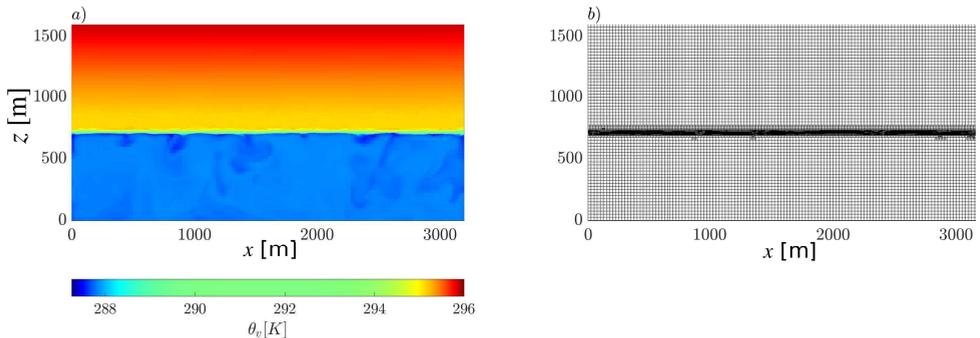
Figure 2.11: Snapshots of a) the vertical slices of the virtual potential temperature field and b) the numerical grid at $t = 3$ h. The case is based on the work of Bretherton et al. (1999).

and provides an additional cause of scale separation that may call for adaptive grid refinement. For example, refinement may be preferred at sharp transitions between different types of land use, such as land–sea interfaces.

2.5 Discussion and Conclusions

We have introduced and tested an adaptive mesh refinement (AMR) method for studies of the atmospheric boundary layer (ABL). This work is motivated by a desire to numerically study highly dynamic cases. Such cases are characterized by a high degree of scale separation throughout the spatial and temporal domain. This work should be viewed as the first step in our AMR-based research that assesses the usage of an AMR method for studies of the ABL. We have based our adaptive-grid simulations on the flow solver implemented in the Basilisk code.

The method is tested using DNS based on a case introduced by Van Heerwaarden and Mellado (2016), describing the growth and subsequent decay of a CBL. The AMR algorithm was able to identify the time-varying turbulent regions in the domain and refined/coarsened the grid accordingly. The AMR-based simulations can reproduce the simulation results of their fixed grid counterparts with minor discrepancies. Furthermore, the AMR algorithm can be tuned to apply more grid cells such that these discrepancies are suppressed. For all AMR runs, the number of grid cells varies significantly over time, resulting in more efficient simulations compared to using a regular fixed grid with identical numerical formulations. This provides a proof of principle for the AMR method regarding ABL systems.

For this case, a numerical solver dedicated to ABL systems (MicroHH) outperformed all other runs in terms of computational efficiency, indicating that there is an overhead associated with the usage of the adaptive solver. In general, the exact impact of this overhead depends on the details of the studied case. The most challenging ABL systems typically owe their complexity to the dynamical interplay between various processes at different length and time scales. Hence, the AMR technique is

likely to be more favourable as complexity increases. More specifically, as discussed in Popinet (2011), the cost of an adaptive simulation, relative to a constant resolution simulation (G) is expected to scale as

$$G = \frac{C_a \Delta^{-D}}{C_c \Delta^{-3}} = \frac{C_a}{C_c} \Delta^{3-D}, \tag{2.13}$$

where C_a and C_c are constants related to the absolute speed of the computation for the adaptive- and constant-resolution simulations, respectively ; Δ is the ratio of the minimum to the maximum scale of the physical system (i.e. a measure of scale separation) and D is the effective (or fractal) dimension of the physical process (which is necessarily ≤ 3). In the present study, Δ is relatively large (i.e of order 10^{-2}) and the computational gain using the adaptive method is correspondingly small, whereas for challenging cases Δ can be several orders of magnitude smaller, with a correspondingly larger potential gain in efficiency of the adaptive method relative to constant-resolution methods. This important aspect of the overall scaling behavior is illustrated in the second entr'acte for a canonical flow set-up. The results shown herein thus motivate our continued research using the AMR technique.

Acknowledgements
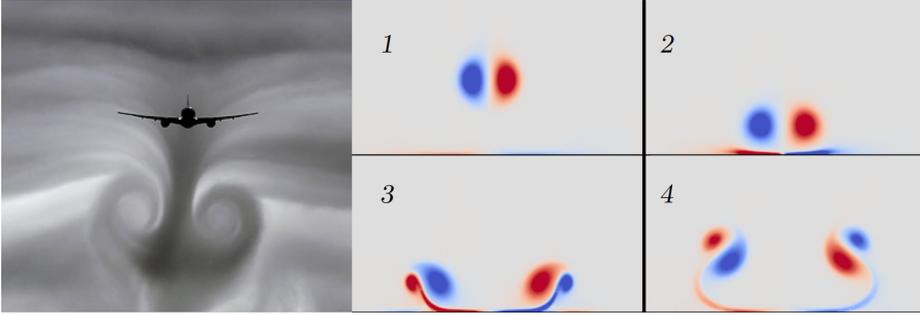
An airplane may target a dipolar vortex structure (dipole) at the underlying surface (top left). P. Orlandi (1990) was the fist to study the fate of the dipole numerically and he found that the original vortices rebound from the surface as they entrain secondary circulation originating from the viscous boundary layer (vorticity snapshots, top right). For an excellent overview of the research since Orlandi's seminal work, we refer to Clercx and Van Heijst (2017). Here we consider a dipole-wall collision and use the vortex-soliton model of S.A. Chaplygin and H. Lamb (Meleshko and Van Heijst, 1994), which is characterized by a size radius R and a propagation velocity U. The boundary layer at the no-slip wall owes its existence to the fluid's viscosity (ν) and with these three parameters we can formulate a dimensionless group that characterizes the system,

$$Re = \frac{UR}{\nu},$$

known as the Reynolds number. Inspired by Kramer et al. (2007), we focus on the vorticity dynamics as a function of the Reynolds number. At the wall, the flow adjusts from the interior, dipole-induced flow, to the no-slip boundary in the so-called viscous boundary layer. Its depth is inversely proportional to the Reynolds number. We simulate the dynamics of the collision in a $15R \times 15R$ domain and present a zoom-in on the vortex structures that emerge in the unstable boundary layer. Furthermore, the adaptive grid is drawn at the corresponding moment in time (bottom snapshots). It can be seen that as the Reynolds number increases, the fraction of the domain that requires the maximum resolution decreases. As such, we log the total wall-clock time of our simulation and plot it as a function of the Reynolds number. We do this for both the adaptive solver (see Chapter 2) and an equidistant-grid solver (see below). For the equidistant solver, the cost scale with Re^3. This can be understood from the fact that the grid-size scales inversely proportional to Re, resulting in the total numbers of grid cells to scale with Re^2, for this two-dimensional simulation. Furthermore, the number of timesteps scales with Re^1 due to the Courant-Freidrichs-Lewy stability criterion. As such the total effort (*cells × iterations*) scales with Re to the (2 + 1 =) 3rd power. Noting that this analysis holds for any equidistant approach. As such, we may already anticipate the performance characteristics of

a solver that is, say, 20 times more efficient than the equidistant-grid approach we have employed (i.e. Basilisk in fixed-grid mode). For the adaptive-grid simulations, the numerical details inherit some properties of the physical system and the resulting scaling behavior is favorable ($Re^{1.6}$) compared to the equidistant solver. Therefore, even though the theorized equidistant-grid solver outperforms the adaptive solver for smaller values of Re ($< \mathcal{O}(1000)$), the adaptive method becomes the more effective option as the scale separation increases.

An detailed description of the used methods is presented online:
`www.basilisk.fr/sandbox/Antoonvh/lamb-dipole.c`
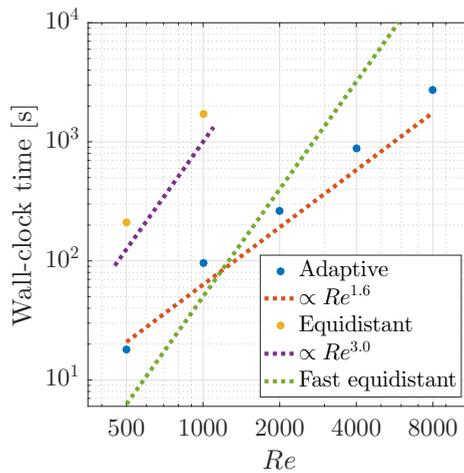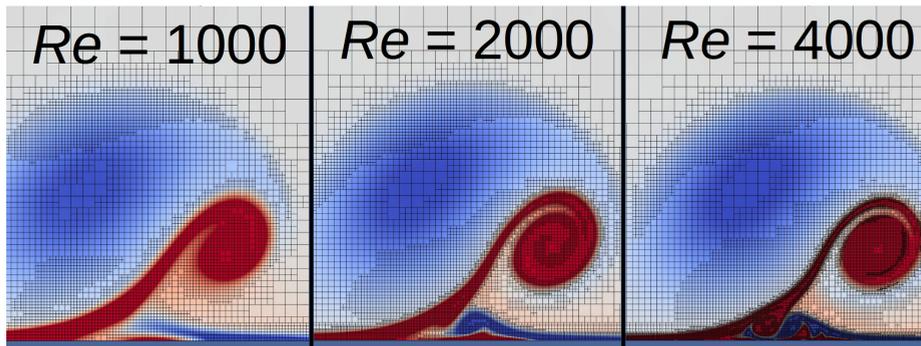
> *If performance was not a central issue, one could use simple and robust methods with excellent theoretical properties, such as first-order Godunov schemes and direct linear solvers, and this article (together with thousands of others) would not make any sense.*
>
> S. Popinet (2015)

3 | Adaptive Cartesian Meshes for Atmospheric Single-Column Models

abstract

It is well known that the representation of certain atmospheric conditions in climate and weather models can still suffer from the limited grid resolution that is facilitated by modern-day computer systems. Herein we study a simple one-dimensional analogy to those models by using a Single-Column Model description of the atmosphere. The model employs an adaptive Cartesian mesh that applies a high-resolution mesh only when and where it is required. The so-called adaptive-grid model is described and we report on our findings obtained for tests to evaluate the representation of the atmospheric boundary layer, based on the first two GABLS intercomparison cases. The analysis shows that the adaptive-grid algorithm is indeed able to dynamically coarsen and refine the numerical grid whilst maintaining an accurate solution. This is an interesting result as in reality, transitional dynamics (e.g. due to the diurnal cycle or due to changing synoptic conditions) are the rule rather than the exception.

3.1 introduction

Single-Column Models (SCMs) are often used as the building blocks for Global (or General) Circulation Models (GCMs). As such, many of the lessons learned from SCM development can be inherited by GCMs and hence the evaluations of SCMs receive considerable attention by the geoscientific model development community (see e.g. Neggers et al., 2012; Bosveld et al., 2014; Baas et al., 2017). In this work, we present a SCM that employs an adaptive Cartesian mesh that can drastically reduce the computational costs of such models, especially when pushing the model's resolution. The philosophy is inspired by recently obtained results on the evolution of atmospheric turbulence in a daytime boundary layer using three-dimensional (3D) adaptive grids. As promising results were obtained for turbulence-resolving techniques such as Direct Numerical Simulations and Large-eddy Simulation (LES), herein we explore whether similar advancements can be made with more practically oriented techniques for the numerical modelling of the atmosphere. As such, the present model uses Reynolds-averaged Navier-Stokes (RANS) techniques to parameterize the vertical mixing processes due to turbulence (Reynolds, 1895), as is typical in weather and climate models.

The discussion of limited grid resolution is present in many studies of SCMs and GCMs. A prominent example is the nocturnal cumulus-cloud case (Wyant et al., 2007): whereas a high resolution mesh is required for capturing the processes at the cloud interface, a coarser resolution may be used for the time when the sun has risen and the cloud has been dissolved. More generally speaking, virtually all of the atmospheric dynamics that require a relatively high-resolution grid for their representation in numerical models are localized in both space and in time. The issue is made more difficult to tackle by the fact that their spatio-temporal localization is typically not known a priori (e.g. the height and strength of a future inversion layer). Therefore, the pre-tuned and static-type grids that most operational GCMs use (virtually all) are not flexible enough to capture all dynamical regimes accurately or efficiently. This also puts a large strain on the used closures for the sub-grid scale processes. In order to mitigate this challenge, GCMs that employ a so-called adaptive grid have been explored in the literature. Here the grid resolution adaptively varies in both space and time, focussing the computational resources to where and when they are most necessary. Most notably, the innovative works of Jablonowski (2004), Jablonowski et al. (2009) and St-Cyr et al. (2008) report on the usage of both Cartesian and non-conforming three-dimensional adaptive grids and clearly demonstrate the potential of grid adaptivity for GCMs. Inspired by their works, we follow a 1D SCM approach and aim to add to their findings, using different grid-adaptive formulations and solver strategies. Since SCMs do not resolve large-scale atmospheric circulations, the analysis herein focusses on the representation of the Atmospheric Boundary Layer (ABL).

Over the years, the computational resources that are available to run computer models have increased considerably (Schaller, 1997). This has facilitated GCMs to increase their models' spatial resolution, enabling to resolve the most demanding processes with increased grid resolutions. However, it is important to realize that the (spatial and temporal) fraction of the domain that benefits most from an increasing maximum resolution necessarily decreases as separation of the modelled spatial scales

increases (Popinet, 2011b). This is because the physical processes that warrant a higher-resolution mesh are virtually never space filling. E.g. the formation phase of tropical cyclones is localized in both space and time and is characterized by internal dynamics that evolve during the formation process. By definition, with an increasing scale separation, only an adaptive-grid approach is able to reflect the effective (or so-called fractal) dimension of the physical system in the scaling of the computational costs (Popinet, 2011b; Van Hooft et al., 2018c). This is an aspect where the present adaptive-grid approach differs from for example, a dynamic-grid approach (Dunbar et al., 2008), that employs a fixed number of grid cells that needs to be predefined by the user. This work employs a similar method for grid adaptation as presented in the work of Van Hooft et al. (2018c) on 3D-turbulence-resolving simulations of the ABL. As such, this work is also based on the adaptive-grid toolbox and built-in solvers provided by the 'Basilisk' code (`http://basilisk.fr`).

We test our model with the well established cases defined for the first two GABLS intercomparison projects for SCMs. As part of the Global Energy and Water cycle EXchanges (GEWEX) modelling and prediction panel, the GEWEX ABL Study (GABLS) was initiated in 2001 to improve understanding of the atmospheric boundary layer processes and their representation in models. Based on observations during field campaigns, a variety of model cases has been designed and studied using both LES and SCMs with a large set of models using traditional static-grid structures. An overview of the results and their interpretation for the first three intercomparison cases are presented in the work of Holtslag et al. (2013). Here we will test the present adaptive-grid SCM based on the first two intercomparison cases, referred to as GABLS1 and GABLS2. These cases were designed to study the model representation of the stable boundary layer and the diurnal cycle, respectively. Their scenarios prescribe idealized atmospheric conditions and lack the complete set of physical processes and interactions encountered in reality. At this stage within our research, the authors consider this aspect to be an advantage, as the present SCM model does not have a complete set of parameterizations for all processes that are typically found in the operational models (see e.g. Slingo, 1987; Grell et al., 2005)).

This paper is organized as follows, the present SCM is discussed in more detail in Sect. 3.2. Based on the results from a simplified flow problem, Sect. 5.3 starts with an analysis of the used numerical methods and the grid adaptation strategy. Model results for ABL-focussed cases that are based on the first two GABLS intercomparison scenarios are also presented in Sect. 5.3. Finally, a discussion and conclusions are presented in Sect. 3.4.

3.2   Model Overview

As we focus on the merits of grid adaptivity in this study on SCMs and not on the state-of-the-art closures for the vertical transport phenomena, we have opted to employ simple and well-known descriptions for the turbulent transport processes. More specifically, the present model uses a stability-dependent, first-order, local, K-diffusivity closure as presented in the work of Louis et al. (1982) and Holtslag and Boville (1993). For the surface-flux parameterizations we again follow the formulations in the work of Holtslag and Boville (1993). However, to improve the representation

of mixing under stable conditions, an alteration is made to the formulation of the so-called stability-correction function under stably-stratified conditions. Based on the work of England and McNider (1995), we use a so-called short-tail mixing function. The used closures for the turbulent transport are summarized next. The upward *surface* fluxes (F) of the horizontal velocity components (u, v), the potential temperature (θ) and specific humidity q are evaluated as:

$$F_u = -C_M U_1 u_1, \tag{3.1a}$$

$$F_v = -C_M U_1 v_1, \tag{3.1b}$$

$$F_\theta = -C_H U_1 \left(\theta_1 - \theta_0 \right), \tag{3.1c}$$

$$F_q = -C_H U_1 \left(q_1 - q_0 \right), \tag{3.1d}$$

Where U is the wind-speed magnitude and indices 0 and 1 refer the to values at the surface and the first model level, respectively. The surface transport coefficients are,

$$C_M = C_N f_{s,M}(\mathrm{Ri_b}), \tag{3.2a}$$

$$C_H = C_N f_{s,H}(\mathrm{Ri_b}), \tag{3.2b}$$

with $\mathrm{Ri_b}$ the surface bulk Richardson number, that is defined as,

$$\mathrm{Ri_b} = \frac{g}{\theta_{v,\mathrm{ref}}} \frac{z_1 \left(\theta_{v,1} - \theta_{v,0} \right)}{U_1^2}, \tag{3.3}$$

where g is the acceleration due to gravity, θ_v is the virtual potential temperature and $\theta_{v,ref}$ is a reference temperature whose value is taken as a scenario-specific constant. Equation 3.3 assumes that θ_v is related to the buoyancy (b) (Boussinesq, 1897) via g and $\theta_{v,ref}$ according to $b = g/\theta_{v,ref}(\theta_v - \theta_{v,ref})$. The virtual potential temperature is related to the potential temperature (θ) and specific humidity (q) according to,

$$\theta_v = \theta \left(1 - \left(1 - \frac{R_v}{R_d} \right) q \right), \tag{3.4}$$

with $R_v/R_d = 1.61$ the ratio of the gas constants for water vapour and dry air (Emauel, 1994; Heus et al., 2010). The so-called neutral exchange coefficient (C_N) is calculated using,

$$C_N = \frac{k^2}{\ln \left((z_1 + z_{0,M})/z_{0,M} \right)^2}, \tag{3.5}$$

with $k = 0.4$ the Von Karman constant, z_1 the height of lowest model level and $z_{0,M}$ is the roughness length for momentum. For the cases studied in this work, the roughness length for heat is assumed to be identical to $z_{0,M}$. The stability correction functions for the surface transport of momentum and heat ($f_{s,M}, f_{s,H}$) are,

$$f_{s,M}(\mathrm{Ri_b}) = \begin{cases} 0, & \mathrm{Ri_b} \geq 0.2, \\ \left(1 - \frac{\mathrm{Ri_b}}{0.2} \right)^2, & 0 \leq \mathrm{Ri_b} < 0.2, \\ 1 - \frac{10\mathrm{Ri_b}}{1 + 75 C_N \sqrt{((z_1 + z_{0,M})/z_{0,M}) \| \mathrm{Ri_b} \|}}, & \mathrm{Ri_b} < 0, \end{cases} \tag{3.6a}$$

$$f_{s,H}(\text{Ri}_{\text{b}}) = \begin{cases} f_{s,M}(\text{Ri}_{\text{b}}), & \text{Ri}_{\text{b}} \geq 0, \\ 1 - \frac{15\text{Ri}_{\text{b}}}{1+75C_N\sqrt{((z_1+z_{0,M})/z_{0,M})\|\text{Ri}_{\text{b}}\|}}, & \text{Ri}_{\text{b}} < 0, \end{cases} \tag{3.6b}$$

which conclude the description of the surface fluxes. The vertical flux $(\overline{w'a'})$ of a dummy variable a due to turbulence within the boundary layer is based on a local diffusion scheme and is expressed as,

$$\overline{w'a'} = -K\frac{\partial a}{\partial z}, \tag{3.7}$$

where K is the so-called eddy diffusivity,

$$K = l^2 S f(\text{Ri}). \tag{3.8}$$

l represents an effective mixing length,

$$l = \min\left(kz, l_{bl}\right), \tag{3.9}$$

with l_{bl} is the Blackadar length scale, we use, $l_{bl} = 70m$ (Holtslag and Boville, 1993). S is the local wind-shear magnitude,

$$S = \sqrt{\left(\frac{\partial u}{\partial z}\right)^2 + \left(\frac{\partial v}{\partial z}\right)^2} \tag{3.10}$$

and $f(\text{Ri})$ is the stability correction function for the vertical flux,

$$f(\text{Ri}) = \begin{cases} 0, & \text{Ri} \geq 0.2, \\ \left(1 - \frac{\text{Ri}}{0.2}\right)^2, & 0 \leq \text{Ri} < 0.2, \\ \sqrt{1 - 18\text{Ri}}, & \text{Ri} < 0, \end{cases} \tag{3.11}$$

i.e. based on the gradient Richardson number,

$$\text{Ri} = \frac{g}{\theta_{v,ref}}\frac{\partial\theta_v/\partial z}{S^2}. \tag{3.12}$$

The authors of this work realize that there have been considerable advancements on the representation of mixing under unstable conditions in the past decades, e.g non-local mixing (Holtslag and Boville, 1993) and turbulent-kinetic-energy-based closures (see e.g., Mellor and Yamada, 1982; Lenderink and Holtslag, 2004). Therefore, we would like to note that such schemes are compatible with the adaptive-grid approach and they could be readily employed to improve the physical descriptions in the present model. From an implementations' perspective, those schemes would not require any grid-adaptation specific considerations when using the Basilisk code.

For time integration; we recognize a reaction-diffusion-type equation describing the evolution of the horizontal wind components and scalar fields such as the virtual potential temperature and specific humidity (q). For a variable field $s(z,t)$, we write,

$$\frac{\partial s}{\partial t} = \frac{\partial}{\partial z}(K\frac{\partial}{\partial z}s) + r. \tag{3.13}$$

Where r is a source term and K is the diffusion coefficient c.f. Eq. 3.8. Using a mixed implicit-explicit first-order-accurate time discretization for the diffusive term and an explicit time integration for the source term (r), with time step Δt separating the solution s^n and s^{n+1}, this can be written,

$$\frac{s^{n+1} - s^n}{\Delta t} = \frac{\partial}{\partial z}(K^n \frac{\partial}{\partial z} s^{n+1}) + r^n. \tag{3.14}$$

Rearranging the terms we write,

$$\frac{\partial}{\partial z}(K^n \frac{\partial}{\partial z} s^{n+1}) - \frac{s^{n+1}}{\Delta t} = -\frac{s^n}{\Delta t} - r^n, \tag{3.15}$$

to obtain a Poisson-Helmholtz equation for s^{n+1}, using the eddy diffusivity calculated from the solution s^n (K^n). Eq. 3.15 is solved using a multigrid strategy, employing a finite-volume-type second-order-accurate spatial discretization (Popinet, 2017b,a). The source term r in Eq. 3.13 is defined using different formulations for the various scalar fields in our model. For θ and q, the source term r concerns the tendency in the lowest grid level due to the surface fluxes (F, see Eqs. 3.1, r_{F_s}) and the effect of large scale synoptic divergence (r_w) according to the vertical velocity w (i.e. prescribed for the GABLS2 case). We write for a dummy variable s,

$$r_{w,s} = -w\frac{\partial s}{\partial z} \tag{3.16}$$

For the horizontal velocity components (u, v) the corresponding source terms (i.e. r_{F_s} and r_w) are also taken into account and supplemented with the additional source term $\boldsymbol{r}_{\boldsymbol{\nabla}_h P, f}$, that concerns the horizontal pressure-gradient-forcing vector (i.e. $-\frac{1}{\rho}\boldsymbol{\nabla}_h P$, for air with a density ρ) and the Coriolis-force term according to the local Coriolis parameter f. For the horizontal velocity vector $\boldsymbol{u} = \{u, v, 0\}$ we write,

$$\boldsymbol{r}_{\boldsymbol{\nabla}_h P, f} = \frac{-\boldsymbol{\nabla}_h P}{\rho} - f\left(\hat{\boldsymbol{k}} \times \boldsymbol{u}\right), \tag{3.17}$$

where '$\times$' represents the cross product operator and $\hat{\boldsymbol{k}} = \{0, 0, 1\}$ the unit vector in the vertical direction. In this work we adopt the commonly used strategy to introduce a velocity vector that known as the geostrophic wind ($\boldsymbol{U_{geo}}$), according to,

$$\boldsymbol{U_{geo}} = \frac{\hat{\boldsymbol{k}}}{\rho f} \times \boldsymbol{\nabla}_h P. \tag{3.18}$$

The most prominent feature of the SCM presented in this work is that it adaptively coarsens and refines the grid resolution based on the evolution of the solution itself. As mentioned in the introduction, the associated grid-adaptation algorithm is the same as described in Van Hooft et al. (2018c). Here we only briefly discuss the general concept.

Apart from the imperfect representation of the physical aspects of a system in numerical models, additional errors naturally arise due to the spatial and temporal discretization. In general, a finer resolution corresponds to a more accurate solution and a simulation result is considered to be 'converged' when the numerically obtained

solution and the statistics of interest do not crucially depend on the chosen resolution. The aim of the grid-adaptation algorithm is to dynamically coarsen and refine the mesh so that the errors due to the spatial discretization remain within limited bounds and to be *uniformly distributed* in both space and time. For our adaptive approach this requires, (1) an algorithm that evaluates a local estimate of the discretization error in the representation of selected solution fields (χ_a for a field 'a') and (2), a corresponding error threshold (ζ_a) that determines if a grid cell's resolution is either too coarse (i.e. $\chi_a > \zeta_a$), too fine (i.e. $\chi_a < 2\zeta_a/3$), or just fine. Grid adaptation can then be carried out accordingly and the solution values of new grid cells can be found using interpolation techniques. A cell is refined when the estimated error for at least one selected solution field exceeds it's refinement criterion and a cell is coarsened when it is considered to be 'too fine' for all selected solution fields. The 'error estimator' (χ) is based on a so-called multi-resolution analysis that is formally linked to wavelet thresholding. The algorithm aims to estimate the magnitude of higher-order contributions in the spatial variability of the solution that are not captured by the solver's numerical schemes. Consistent with the second-order spatial accuracy of the solver's numerical schemes (Popinet, 2017a), the algorithm employs a second-order accurate wavelet-based error estimate. In practice, grid refinement will typically occur at the locations where the solution is highly 'curved', whereas those areas where the solution fields vary more 'linearly' in space are prone to coarsening. The error threshold, or so-called refinement criterion ζ, is defined by the user. Noting that similar to the pre-tuning of the fixed-in-time grids as is common in most SCMs, the balance between accuracy and the required computational effort remains at the discretion of the model's user.

For the cases in this work that focus on the ABL (i.e. in Sect 3.3.2 and 3.3.3), the dynamics are governed by the wind ($\vec{U} = (u, v)$) and the virtual potential temperature (θ_v), hence we base the refinement and coarsening of the grid on a second-order-accurate estimated error associated with the representation of these discretized fields. Based on trial and error, we set the corresponding refinement thresholds,

$$\zeta_{u,v} = 0.25 \text{ m/s}, \tag{3.19}$$
$$\zeta_{\theta_v} = 0.5 \text{ K}, \tag{3.20}$$

for both of the horizontal wind components and virtual potential temperature, respectively. These values are the result of a choice by the authors that aims to strike an arbitrary balance between the accuracy of the solution and the computational effort required to run the model. Note that a similar (arbitrary) balance needs also to be found when static grids are employed. For a simple flow set-up, Sect. 3.3.1 presents an example convergence study to show the effects of using different refinement criteria on the accuracy of the obtained solutions.

Grid adaptation is carried out each time step. The tree-based anisotropic-grid structure in Basilisk facilitates a convenient basis for the multi-resolution analysis and the subsequent refinement and coarsening of cells at integer levels of refinement. This entails that the spatial resolution can vary by factors of two (Popinet, 2011b). For the adaptive-grid runs presented in this paper, the time spent in the actual grid assessment and adaptation routines is less than than 5% of the total wall-clock time (see table 4.1).

Apart from the Ekman-spiral case in Sect. 3.3.1, the physical time step in the ABL-focussed cases is adaptively varied between 2 sec. and 15 sec. based on the convergence properties of the aforementioned iterative solver. Noting that these values are rather small compared to existing GCMs that often employ higher-order-accurate time-integration schemes. Additionally, the correlation of spatial and temporal scales warrants a smaller time step, since the present model employs a higher maximum vertical resolution compared to that of an operational GCM. The solver's second-order spatial accuracy is validated and the performance is accessed for a simple flow set-up in Sect. 3.3.1. For the exact details of the model set-ups for the cases presented in this paper, the reader is referred to the case-definition files (in legible formatting). Links are provided to their online locations in table 4.1.

Table 3.1: The exact formulation of the methods are described at the online locations of the definition files for the different cases presented in this manuscript. The wall-clock times are evaluated using a single core (processor model: Intel i7-6700 HQ).

Section	Case	Grid	URL: via Basilisk	time steps	time [s]
3.3.1	Ekman flow	Adaptive	ekman.c	1000	≈ 19
"	"	Equidistant	ekmanfg.c	1000	≈ 18
3.3.2	GABLS1	Adaptive	GABLS1.c	16204	≈ 1.4
"	"	Equidistant	GABLS1fg.c	16324	≈ 0.9
3.3.3	GABLS2	Adaptive	GABLS2.c	24262	≈ 9
"	"	Equidistant	GABLS2fg.c	33993	≈ 22

3.3 Results

3.3.1 The Laminar Ekman spiral and grid adaptation

Before we focus our attention on cases that concern the ABL, this section discusses the philosophy of the used grid adaptation strategy based on the analysis of a one-dimensional (1D) *laminar* Ekman-flow set-up. This simple and clean set-up enables to quantify numerical errors explicitly and test the solver's numerical schemes. The aim of this section is to show that the grid-adaptation strategy and the accompanying refinement criteria provide a consistent and powerful framework for adaptive mesh-element-size selection. Results are presented for both an equidistant-grid and the adaptive-grid approach. The case describes a neutrally-stratified fluid with a constant diffusivity for momentum (K) given by the kinematic viscosity ν and density ρ in a rotating frame of reference with respect to the Coriolis parameter f. A flow is forced by a horizontal pressure gradient ($-\boldsymbol{\nabla_h} P$) according to Eq. 3.18 using $\boldsymbol{U_{geo}} = \{U_{geo}, 0\}$, over a no-slip bottom boundary (located at $z_{bottom} = 0$). Assuming that the velocity components converge towards the geostrophic wind vector for $z \to \infty$ and vanish at the bottom boundary, there exists an analytical, 1D, steady solution for the

horizontal wind component profiles $(u_E(z), v_E(z))$, that is known as the Ekman spiral;

$$u_E = U_{geo} \left(1 - e^{-\gamma z} \cos(\gamma z) \right), \tag{3.21}$$

$$v_E = U_{geo} e^{-\gamma z} \sin(\gamma z), \tag{3.22}$$

with γ the so-called inverse Ekman depth, $\gamma = \sqrt{f/(2\nu)}$. We choose numerical values for U_{geo}, γ and f of unity in our set-up and present the results in a dimensionless framework. The solution is initialized according to the exact solution and we set boundary conditions based on Eqs. 3.21 and 3.22. Equation 3.13 is solved numerically for both u and v components, on a domain with height $z_{top} = 100\gamma^{-1}$. The simulation is run until $t_{end} = 10f^{-1}$, using a fixed time step $\Delta t = 0.01 f^{-1}$. The time step is chosen sufficiently small such that the numerical errors are dominated by the spatial discretization rather than by the time-integration scheme. During the simulation run, discretization errors alter the numerical solution from it's exact, and analytically steady, initialization. For all runs, the diagnosed statistics regarding the numerical solutions that are presented in this section have become steady at $t = t_{end}$.

The spatial-convergence properties for the equidistant-grid solver are studied by iteratively decreasing the used (equidistant) mesh-element sizes (Δ) by factors of two and we monitor the increasing fidelity of the solution at $t = t_{end}$ between the runs. Therefore, based on the analytical solution, a local error ($\epsilon_{u,v}$) of the numerically obtained solution (u^n, v^n) within each grid cell is diagnosed and is defined here as:

$$\epsilon_a = \| a^n - \langle a_E \rangle \|, \tag{3.23}$$

where a is a dummy variable for u and v, $\langle a_E \rangle$ is the grid-cell-averaged value of the analytical solution (a_E) and a^n the value of the numerical solution within the cell. Noting that a^n also represents the grid-cell-averaged value in our finite-volume approach. Figure 3.1a shows the results for all runs and compares the used grid resolution (Δ) with the error $\epsilon_{u,v}$. It appears that the observed range of ϵ-values is large and typically spans 10 orders of magnitude, with a lower bound defined by the 'machine precision' (i.e. $\approx 10^{-15}$ for double-precision floating-point numbers). This wide range can be explained by the fact that the Ekman spiral is characterized by exponentially decreasing variation with height (see Eqs. 3.21, 3.22) and hence the equidistant grid may be considered overly refined at large z. This illustrates that, for a given solver formulation, the error in the solution is not directly dictated by the mesh-element size, but also depends on *the local shape of the numerical solution itself*. This poses a challenge for the pre-tuning of meshes applied to GCMs, where a balance need to be found between accuracy and computational speed performance. The solution of a future model run is not known beforehand and hence the tuning of the grid typically relies heavily on experience, empiricism and a-priori knowledge. This motivates to apply the method of error *estimation* in the representation of a discretized solution field as described in Popinet (2011b) and Van Hooft et al. (2018c). For both velocity components, this estimated error ($\chi_{u,v}$) is evaluated at the end of each simulation run for each grid cell and is plotted against the corresponding actual error ($\epsilon_{u,v}$) in Fig. 3.1b. It seems that for this virtually steady case, there is a clear correlation between the diagnosed (instantaneous) χ-values and the ϵ-values that have accumulated over the simulation run time. Even though the correlation is not perfect, it provides a convenient and consistent framework for a grid adaptation algorithm. As
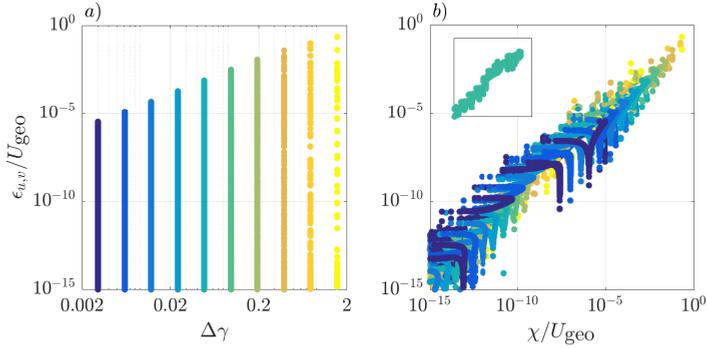
Figure 3.1: The locally evaluated error in the numerical solutions for u and v at $t = t_{end}$, based on the analytical solution ($\epsilon_{u,v}$, see Eq. 3.23) for 10 runs using different equidistant mesh-element sizes. The left-hand side plot (a) Shows that the diagnosed errors for each run plotted against the used mesh-element size (Δ) times the inverse Ekman depth (γ, see text). The right-hand side plot (b) shows, with the same colour coding as in the left-hand side plot (a), the correlation between the wavelet-based estimated error (χ) and the corresponding diagnosed error in the numerically obtained solution (ϵ). The inset (using the same axis scales) shows the results for a single run, and reveal a spread of several orders of magnitude in both ϵ and χ values.
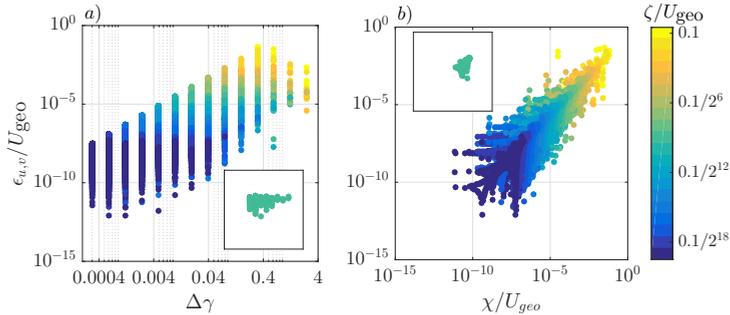

Figure 3.2: The locally evaluated error in the numerical solutions for u and v at $t = t_{end}$, based on the analytical solution ($\epsilon_{u,v}$, see Eq. 3.23) for 20 runs using the adaptive-grid approach with different refinement criteria (see colour bar). The left-hand side plot (a) Shows that the diagnosed errors for each run plotted against the used mesh-element size (Δ). The inset (using the same axis scales) shows the results for a single run. The right-hand side plot (b) shows the correlation between the wavelet-based estimated error (χ) and the corresponding diagnosed error in the numerically obtained solution (ϵ)). The inset (using the same axis scales) shows the results for a single run, and reveals a relatively small spread in both ϵ and χ values compared to the equidistant-grid results presented in figure 3.1b.

such, a second convergence test for this case is performed using a variable-resolution grid within the domain. The mesh is based on the aforementioned adaptive-grid approach. For these runs, we iteratively decrease the so-called refinement criterion ($\zeta_{u,v}$) by factors of two between the runs and monitor the increasing fidelity of the numerically obtained solution for all runs. The refinement criterion presets a threshold value (ζ) for the estimated error χ that defines when a cell should be refined ($\chi > \zeta$) or alternatively, when it may be coarsened ($\chi < 2\zeta/3$). Figure 3.2a presents the results and compares the used local grid resolution against $\epsilon_{u,v}$ for the various (colour-coded) runs. It appears that for all separate runs, the algorithm employed a variable resolution mesh and that this has resulted in a smaller range of the local error in the solution (ϵ), as compared to the equidistant-grid cases. The local error in the solution is also compared against the wavelet-based estimated error in the representation of the solution fields in Fig. 3.2b. Compared to the results from the equidistant-grid approach as presented in Fig. 3.1b), the spread of the χ and ϵ values is relatively small for the separate runs when the adaptive-grid approach is used. The most prominent reason for the finite spread is that the error (ϵ) was diagnosed after 1000 time steps. This facilitated errors in the solution that arise in the solution at a specific location (with a large χ-value) to 'diffuse' over time towards regions where the solution remains to be characterized by a small χ-value (not shown). Also, since u and v are coupled (due to the background rotation), local errors that arise in the solution for u 'pollute' the v-component solution, and vice versa. Furthermore, a spread is expected because the tree-grid structure only allows the resolution to vary by factors of two (Popinet, 2011b).

Finally, the global convergence characteristics and the speed performance of the two approaches are studied. The global error (η) in the numerically obtained solution is evaluated as,

$$\eta = \int_{z_{bottom}}^{z_{top}} (\epsilon_u + \epsilon_v)\, \mathrm{d}z, \tag{3.24}$$

In order to facilitate a comparison between the methods, we diagnose the number of used grid cells (N) for the adaptive-grid run. Figure 3.3a shows that for both approaches the error scales inversely proportional to the used number of grid cells to the second power (i.e. second-order spatial accuracy in 1D). The adaptive grid results are more accurate than the results from the fixed-grid approach when employing the same number of grid cells. Figure 3.3b shows that for both approaches the required effort (i.e. measured here in wall-clock time) scales linearly with the number of grid cells, except for the runs that require less than one-tenth of a second to perform. The plots reveals that *per grid cell* there is computational overhead for the adaptive-grid approach. These results show that the used numerical solver is well behaved.

The following sections are devoted to testing the adaptive-grid approach in a more applied SCM scenario, where the turbulent transport closures are applied (see Sect. 3.2) and the set-up is unsteady. Here, the quality of the adaptive-grid solution has to be assessed by comparing against reference results from other SCMs, large-eddy simulations and the present model running in equidistant-grid mode.
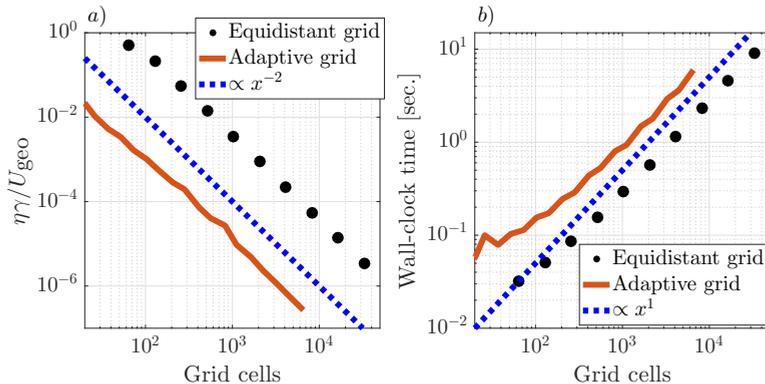
Figure 3.3: The scaling characteristics for the laminar-Ekman-spiral case. (a) Presents the error convergence for the equidistant-grid and adaptive-grid approach. The errors (η) follow the slope of the blue dashed line that indicates the second-order accuracy of the methods. The wall-clock time for the different runs is presented in (b), showing that for both of the aforementioned approaches, the required effort scales linearly with the number of grid cells.

3.3.2 GABLS1

The first GABLS intercomparison case focusses on the representation of a stable boundary layer. It's scenario was inspired by the LES study of an ABL over the Arctic sea by Kosović and Curry (2000). The results from the participating SCMs are summarized and discussed in Cuxart et al. (2006), for the LES intercomparison study, the reader is referred to the work of Beare (2006). The case prescribes the initial profiles for wind and temperature, a constant forcing for momentum corresponding to a geostrophic wind vector, $U_{geo} = \{8, 0\}$m/s and Coriolis parameter $f = 1.39 \times 10^{-4}\text{s}^{-1}$. Furthermore, a fixed surface-cooling rate of 0.25 K/hour is applied and $\theta_{v,ref} = 263.5K$. The model is run with a maximum resolution of 6.25 meter and a domain height of 400 meters. The maximum resolution corresponds to 6 levels of tree-grid refinement, where each possible coarser level corresponds to a factor of two increase in grid size.

Due to the idealizations in the case set-up with respect to the reality of the field observations, the model results were not compared against the experimental data (Cuxart et al., 2006). However, for the SCMs, a reference was found in the high-fidelity LES results that tended to agree well between the various models. The LES results therefore serve as a benchmark for the results obtained with the present model. This facilitates a straightforward testing of the formulations and implementations of the used physical closures, before we continue our analysis towards the full diurnal cycle. Inspired by the analysis of Cuxart et al. (2006) and *their* figure 3, we compare our SCM results with the 6.25 meter-resolution LES ensemble results. We focus on the profiles for the wind components and potential temperature averaged over the ninth hour of the simulation in Fig. 3.4. We observe that the present SCM is in

good agreement with the LES results and is able to capture the vertical structure of the ABL, including the low-level jet. The differences are only minor compared to the variations in the results presented in the aforementioned GABLS1 SCM reference paper.
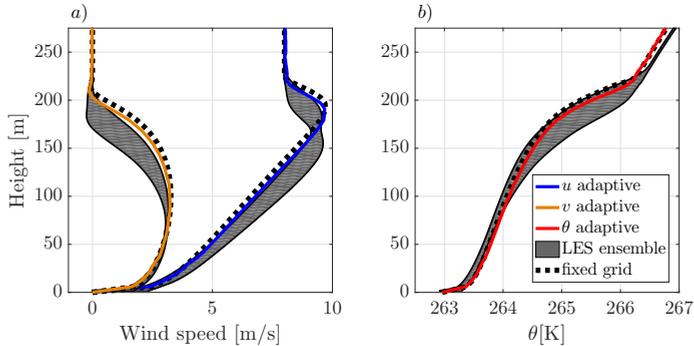

Figure 3.4: Time averaged profiles over the ninth hour of the run according to the GABLS1 intercomparison scenario. For (a) the horizontal wind components and (b) the potential temperature. Results are obtained with the present adaptive-grid SCM (coloured lines), the LES models ensemble (i.e mean $\pm \sigma$) from Beare (2006) (grey-shaded areas) and the present SCM, employing an equidistant and static grid with a 6.25 meter resolution (dashed lines). For $z > 250$m, the profiles have remained as they were initialized.
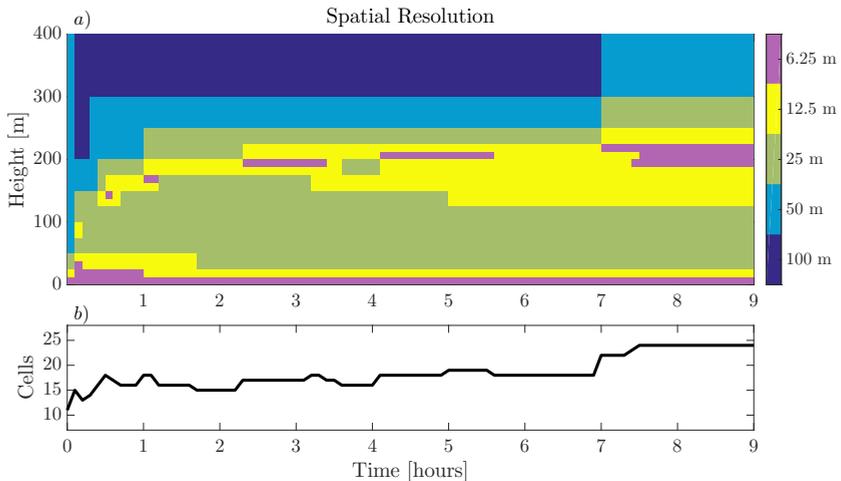
Figure 3.5: Evolution of (a) the vertical spatial-resolution distribution and (b) the total number of grid cells, for the GABLS1 intercomparison case.

Note that in general, results are of course sensitive to the closure chosen to parameterize the turbulent transport, in our case given by Eqs.3.6 and 3.11. In order to separate between the numerical effects of using grid adaptivity and the chosen physical closures, we define an additional reference case in which we run an *equidistant-grid*

SCM. This model run employs a fixed 6.25 meter resolution (i.e with 64 cells), but otherwise identical closures and numerical formulations. I.e. we have switched-off the grid adaptivity and maintain the maximum resolution throughout the domain. We can observe that results between both SCMs are in good agreement but that minor deviations are present. These discrepancies are on the order of magnitude of the refinement criteria and can be reduced by choosing more stringent values, that would result in using more grid cells. The evolution of the adaptive-grid structure is shown in Fig. 3.5 a. We see that a relatively high resolution is employed near the surface, i.e. in the logarithmic layer. Remarkably, without any a priori knowledge, the grid is refined at a height of 150 m $< z <$ 200 m as the so-called low-level jet develops, whereas the grid has remained coarse above the boundary layer where the grid resolution was reduced to be as coarse as 100 meters. From Fig.3.5 b we learn that the number of grid cells varied between 11 and 24 over the course of the simulation run.

3.3.3 GABLS2

The second GABLS model intercomparison case was designed to study the model representation of the ABL over the course of two consecutive diurnal cycles. The case is set-up after the observations that were collected on the 23rd and 24th of October, 1999 during the CASES-99 field experiment in Leon, Kansas, USA (Poulos et al., 2002). The case prescribes idealized forcings for two consecutive days that were characterized by a strong diurnal cycle pattern. During these days, the ABL was relatively dry, there were few clouds and $\theta_{v,ref} = 283.15K$. The details of the case are described in the work of Svensson et al. (2011) that was dedicated to the evaluation of the SCM results for the GABLS2 intercomparison. Compared to the original case prescriptions, we choose a slightly higher domain size of $z_{top} = 4096$ meters (compared to 4000 m), so that a maximum resolution of 8 meters corresponds to 9 levels of refinement.

In this section we place our model output in the context of the results presented in the work of Svensson et al. (2011), that, apart from the SCM results, also includes the results from the LES by Kumar et al. (2010). To obtain their data we have used the so-called 'data digitizer' of Rohatgi (2018). Inspired by the analysis of Svensson et al. (2011) and *their* figures 10 and 11, we compare our results for the wind-speed magnitude ($U = \|\vec{u}\|$) and virtual potential temperature profiles at 14:00 local time on the 23rd of October in Fig. 3.6 a and b, respectively. Here we see that the results obtained with the present SCM fall within the range of the results as were found with the selected models that participated in the original intercomparison. These models also employed a first-order-style turbulence closure and have a lowest model-level height of less than 5 meters. The present modelled virtual potential temperature (θ_v) shows a slight negative vertical gradient in the well mixed layer. This is a feature related to the usage of the local K-diffusion description for the turbulent transport (see Sect. 3.2 and the work of Holtslag and Boville (1993)). Figure 3.6 c presents a timeseries of the 10-meter wind speed (U_{10m}) during the 23-rd of October. Again the present model results compare well with the others. Next, in order to validate the grid-adaptivity independently from the used closures, we present the hourly evolution of the wind speed on the 24-th of October against the results obtained with adaptivity switched off, using 512 *equally-spaced* grid points in Fig.
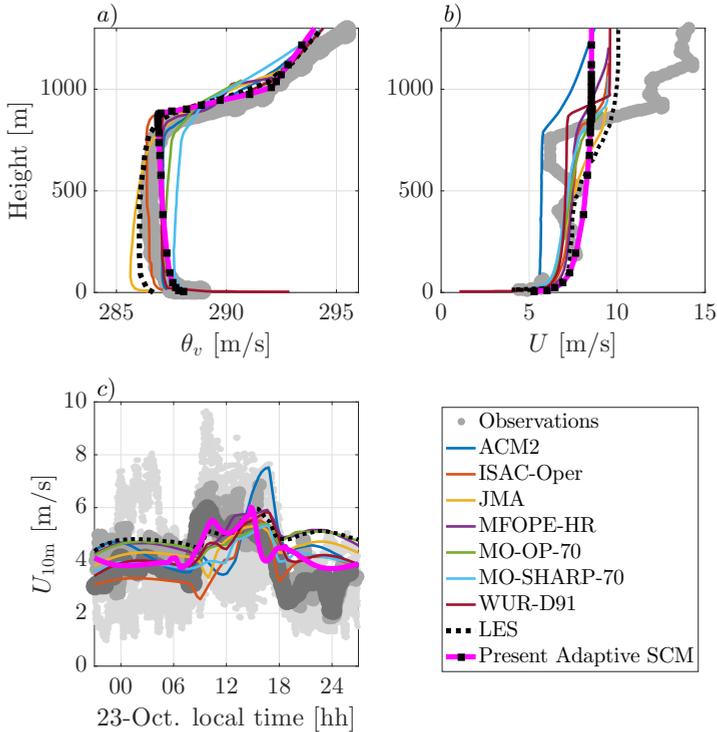
Figure 3.6: Comparison of the results obtained with the adaptive-grid SCM and the participating models in the work of (Svensson et al., 2011) for the vertical profiles of (a) the virtual potential temperature and (b) the wind-speed magnitude, for 14:00 local time on the 23rd of October. Lower panel: (c) the evolution of the 10-meter wind speed (U_{10m}) on the 23rd of October. For the used model abbreviations in the legend, see Svensson et al. (2011). The different shades of grey in plot c) indicate observations from different measurement devices, see Svensson et al. (2011) for the details.

3.7. A nearly identical evolution of the wind speed profiles is observed and even the small-scale features in the inversion layer (i.e. $z \approx 800$ m) are present in the adaptive-grid-model calculations. The corresponding evolution of the adaptive-grid structure is presented in Fig. 3.8, where the colours in the resolution plot appear to sketch a 'Stullian' image, showing a prototypical diurnal evolution of the ABL (see figure 1.7 in the book of Stull, 1988). Apparently, the grid-adaptation algorithm has identified (!) the 'surface layer' within the convective boundary layer, the stable boundary layer, the entrainment zone and the inversion layer as the dynamic regions that require a high-resolution mesh. Conversely, the well-mixed layer within the CBL, the residual layer and the free-troposphere are evaluated on a coarser mesh. The total number of grid cells varied between 24 and 44.
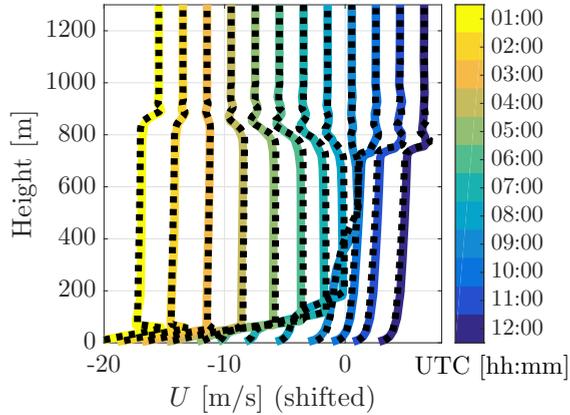
Figure 3.7: Vertical profiles of the wind-speed magnitude U obtained with the adaptive-grid (in colour) and the fixed equidistant-grid (dashed) SCMs. The twelve plotted profiles are obtained for the 24th of October with an hourly interval, starting from 1:00 AM local time. Noting that the profiles are shifted in order to distinguish between the different times (with vanishing wind at the surface). The profiles of U are constant with height for $z > 1200$m.

Figure 3.8: Evolution of (a) the vertical spatial resolution and (b) the total number of grid cells, for the GABLS2 intercomparison case. Two full diurnal cycles, corresponding to the 23rd and 24th day of October, 1999 (ranging from the labels 1:00:00 to 3:00:00 on the x-axis).

3.4 Discussion & Conclusions

In this work we have presented a one-dimensional (1D) single-column model (SCM) that employs a mesh whose resolution is varied adaptively based on the evolution of the numerically obtained solution. This is an attractive feature because it is a prerequisite to enable the c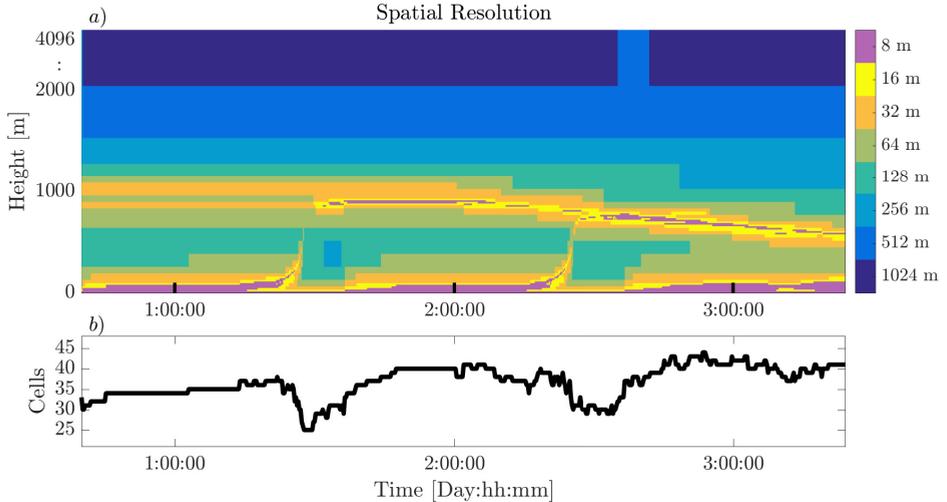omputational effort required for the evaluation of numerical solution to scale with the complexity of the studied physical system. The adaptation algorithm based on limiting discretization errors appears to function very well for a wide variety of geophysical applications: e.g. 3D atmospheric turbulence-resolving models (Van Hooft et al., 2018c), tsunami and ocean-wave modelling (Popinet, 2011b; Beetham et al., 2016; Marivela-Colmenarejo, 2017), hydrology (Kirstetter et al., 2016), two-phase micro physics (Howland et al., 2016), flow of granular media (Zhou et al., 2017) and shock-wave formation (Eggers et al., 2017). For these studies on highly dynamical systems, the adaptive-grid approach is chosen because it offers a more computationally efficient approach as compared to the usage of static grids.

The present work does not include an in-depth assessment and discussion on the performance of the presented methods in relation to the computational speed. Even though this is an important motivation for the application of the adaptive-grid strategy to GCMs, the authors argue that a SCM is not suitable for speed-performance testing: the speed of single-column calculations is virtually never a critical issue. Only in 3D mode, when SCMs are 'stitched together' to enable the resolving of global circulations, the model's computational efficiency becomes an issue. Furthermore, the performance of a SCM that employs a few tens of cells is not a good indicator for the performance of a GCM that can employ billions of grid cells. For the latter, parallel computation overhead and the so-called memory bottle neck are important aspects. In contrast, for the SCM case, the complete instruction set and solution data can typically be loaded onto the cache memory of a single CPU's core. Nevertheless, for the readers' reference, the required run times for the different SCM set-ups presented herein are listed in table 4.1, and figure 3.3b also presents quantitative results on this topic and shows that the adaptive-grid solver is well behaved.

Following the turbulence resolving study of Van Hooft et al. (2018c), the results presented herein are a proof-of-concept for future 3D modelling, using RANS techniques. The authors of this work realize that the present SCM is a far cry from a complete global model and that more research and development is required before the method can be compared on a global-circulation scale. As shown by e.g. Jablonowski (2004), a 3D adaptive grid also allows a variable grid resolution in the horizontal directions. This further enables the computational resources to focus on the most challenging atmospheric processes where there is a temporal and spatial variation in the horizontal-resolution requirement of the grid. Examples include the contrasting dynamics between relatively calm centres of high-pressure circulations and those characterizing stormy low-pressure cells. Also, in the case of a sea breeze event (Arrillaga et al., 2016), it would be beneficial to temporarily increase the horizontal resolution near the land–sea interface. As such, we encourage the usage of this technique for those meteorologically challenging scenarios.

Entr'acte 3: Two Vortex Rings in a Head-on Collision
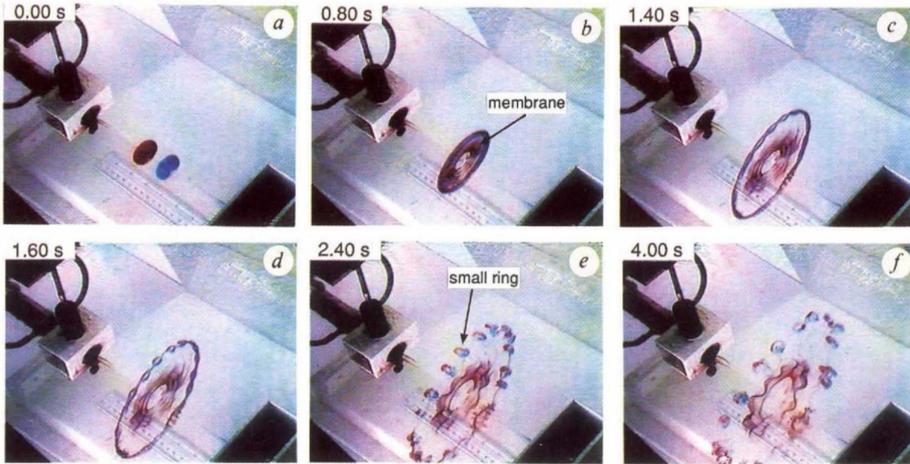
In 1992, T.T. Lim and T.B. Nickels published their spectacular findings from a water-tank lab experiment studying the head-on collisions of two ring vortices (top snapshots of dye). The experiment starts by triggering two opposing, axially symmetric, short-lived jets of dyed water into a large tank. Such a jet may transform into a ring vortex; a flow structure that entrains the injected dye as it propagates solitary though the fluid. Lim and Nickels (1992) captured the formation of a dye membrane as the vortex rings' major radius quickly increases during the collision. Next, via a shear instability, the two vortex rings pinch and connect with each other to form between 15 and 20 smaller vortex rings. These experimental results have inspired numerical modelers to study these dynamics as well. E.g. Kudela and Kosior (2014) employed 'many graphics cards' [sic], but were unable to reproduce the experimental results proper. More recently, McKeown et al. (2018) successfully simulated the recombination process of the rings, but artificially imposed a five-fold azimuth symmetry to reduce the computational costs. Naturally, we have also setup the case with Basilisk's adaptive flow solver, using a maximum resolution that corresponds to a 2048^3-cell equidistant grid. The resulting snapshots of the grid structure and the vortex structures are presented against a purple background. The white surfaces are based on the λ_2 vortex-detection criterion of Jeong and Hussain (1995). Furthermore, a simulation is performed with passive tracers added to each jet (bottom left). This facilitates a visual comparison against the results from the modernly equipped dye-experiment documentary of Destin Sandlin (2018) (bottom right), presented online via his Youtube channel; *'Smarter Every Day'*. The computations never used more than 4.5×10^6 cells, less than 0.05% of the maximum number (2048^3). This enabled to perform the numerical experiment using a desktop workstation. You may view the methods online;
`www.basilisk.fr/sandbox/Antoonvh/two_rings.c` .
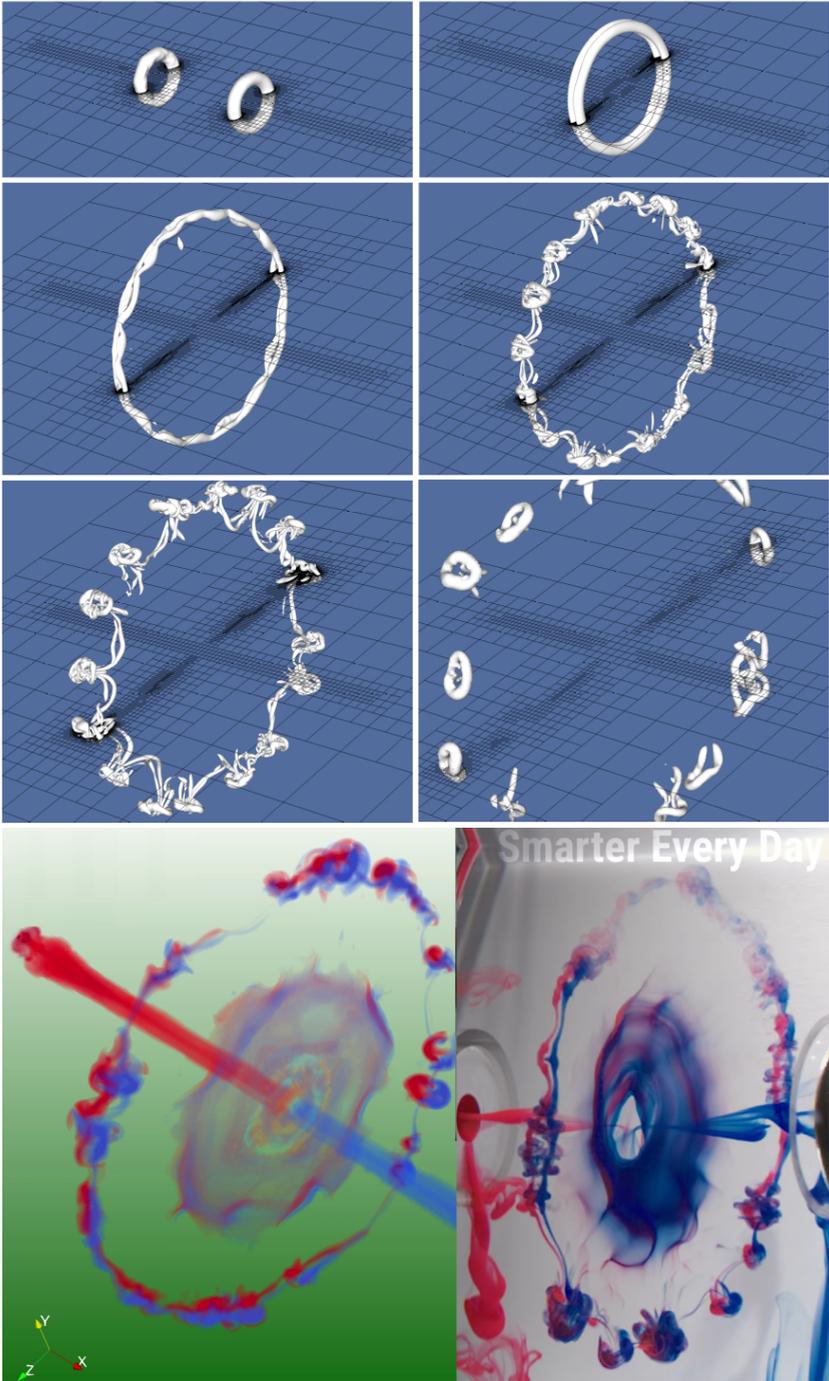
> *Emergence is complexity arising from simplicity, and emergence is everwhere!*
>
> Kurzgesagt (2017)

4 | An Idealized Description for the Diurnal Cycle of the Atmospheric Boundary Layer

abstract

We present a conceptual model for the diurnal cycle of the dry atmospheric boundary layer (ABL). It may serve as a framework for future numerical studies on the transitional dynamics that characterize the ABL over land. The conceptual model enables to define expressions for relevant physical scales as a function of the most prominent forcing parameters and the low degree of complexity facilitates a dimensionless description. This is useful to help generalize boundary-layer dynamics that occur on a diurnal timescale. Further, the model's application for numerical studies is illustrated herein with two examples: A single-column-model study which assesses the effect of wind forcing on the main characteristics of the diurnal cycle, and a large-eddy-simulation study on the daily evolution of turbulence under weak-wind-forcing conditions. The results from these studies sketch the general evolution of the present set of diurnal-cycle systems in more detail. We discuss how the setups are able to reproduce well-known dynamical features of the ABL and also highlight limitations, where the simple conceptual system is unable to describe realistic ABL behavior. We conclude that the present conceptual model has an interesting balance between model-system complexity and physical realism, such that it is useful for future, idealized, studies on the diurnal cycle of the ABL.

4.1   Introduction

Apart from the Antarctic summer and winter time, the Atmospheric Boundary Layer (ABL) over land is characterized by a diurnal cycle. As such, a thorough understanding of the boundary-layer dynamics on a 24-hour timescale is highly desirable. A classic result on the diurnal evolution of the ABL structure is presented in the well-known book of Stull (1988). The seminal depiction of the ABL's diurnal evolution is powerful for didactic purposes and provides a context for in-depth research on the various ABL archetypes. For example, the daytime Convective Boundary Layer (CBL) and the nighttime Stable Boundary Layer (SBL) are often studied separately, due to their dynamical differences. As such, conceptual and quantitative models for the ABL typically assume (quasi) stationary dynamics. This approach has proven successful and has yielded detailed knowledge on the complex dynamics that are encountered in the ABL. Further, studies focusing on the early-morning transition (e.g. Angevine et al., 2001; Beare, 2008) and late-afternoon transition (e.g. Grimsdell and Angevine, 2002; Van Heerwaarden and Mellado, 2016) aim to bridge the gap in our understanding that lays between convective and stable boundary layer conditions. However, proper understanding of the interactions between even the most prominent processes that govern the dynamical evolution of the ABL during a diurnal cycle, including the transitional dynamics, remains elusive (Lothon et al., 2014; LeMone et al., 2018). For this purpose, we build upon the idealized diurnal cycle as presented in Stull (1988) and introduce a simplified description of the governing processes. The additional value is that the concept yields quantitative expressions for relevant physical scales and a dimensionless framework that may be useful for future investigations. Following the conceptual development, we emphasize numerical modeling as a tool to study the dynamical behavior of the simplified framework in more detail. We conduct exemplifying numerical studies that illustrate the potential for more in-depth research via this route.

When the aim is to accurately describe local weather patterns, all relevant physical processes need to be taken into account. Alternatively, in order to gain understanding of the dynamics, idealized model cases have been studied in virtually countless works regarding the ABL. The decrease in the model-system complexity allows to better distinguish the interactions between the processes that remain represented in the model. However, interpretation of the results requires special attention when placing them in the context of reality and usually comes with disclaimers regarding the validity of the assumptions that were made. As such, both conceptual and numerical models have to strike a balance between physical realism and model-system complexity and they typically need to be tailored for a specific research purpose. Herein we introduce such a simplified model, aiming to capture the key dynamical aspects of a diurnal cycle of the dry ABL. We introduce the set of parameters that govern the dynamics, and formulate expressions for relevant characteristic physical scales such as boundary-layer height, wind speed and temperature. Furthermore, the low degree of complexity enables to describe the system with few dimensionless parameters.

Apart from the a priori analysis, it is tempting to study the dynamics of the present conceptual model for the diurnal cycle in more detail. Herein we aim to do so using numerical methods, where the computer model of the ABL is setup following the present conceptual/simplified descriptions of the relevant forcing mechanisms.

More specifically, we conduct a Single-Column-Model (SCM) study on the effect of the pressure-gradient forcing and study the evolution of the atmospheric turbulent structures using a turbulence-resolving Large-Eddy Simulation (LES). These preliminary numerical model studies illustrate how the present concepts can form a useful framework for future model studies on the diurnal cycle. The results exemplify how relevant and well-known features of the ABL are dynamically retrieved by the model setup. Further, we also highlight some of the limitations of the present concepts with respect to their ability to describe reality.

From the numerical-modeling perspective, we argue that there exist a bifurcation regarding the description of the surface boundary in model scenarios. On one hand, there are studies at the idealized side of the spectrum, that artificially prescribe the boundary conditions of the ABL regarding the thermodynamic variable at the underlying surface via the evolution of the surface sensible heat flux or the evolution of the surface temperature. These studies typically employ turbulence resolving methods such as LES or direct numerical simulation (DNS) (e.g. Sullivan et al., 2016; Haghshenas and Mellado, 2019) techniques. Of course, in reality, both surface flux and temperature are *internal* variables, that will actively respond on atmospheric dynamics itself. Rather than prescribing the surface conditions beforehand, there are other numerical studies that assess the surface temperature and the heat flux as parameters that are integrally part of the soil-atmosphere continuum. This requires the evaluation of the various terms in the surface energy budget (SEB) equation, which in turn increases the model's complexity by either resolving more physical processes or introducing more extensive closures for their parametrization. The advantage being that the ABL can then develop according to the *external forcings* of the system. Such models typically rely on Reynolds-Averaged-Navier-Stokes (RANS) modelling (Reynolds, 1895), either in a full three-dimensional (3D) numerical model (e.g. Greve et al., 2013) or using a single-column model (SCM, e.g. Baas et al., 2018). The more realistic setups, that aim to include all the relevant processes for weather prediction, have also become the realm of LES (e.g. Bertoldi et al., 2007; Liu and Shao, 2013; Heinze et al., 2017; Maronga and Bosveld, 2017). In this work we introduce a simple SEB that takes the mid-way between both approaches. The setup is simple and does not require the model to resolve or parameterize much physical processes other than turbulent transport. This is advantageous as it means that the setup can be readily run with existing numerical-solver codes and has limited degrees of freedom. On the other hand, it does not require a prescribed formulation of the heat flux or temperature at the surface, which is interesting from a physical point of view.

This paper delineates between the description of the conceptual model, including the a priori analysis, and the two numerical studies. The description of the system and the accompanying idealizations are described in Sect. 4.2.1. This scenario is a priori analyzed, resulting in a conceptual model, the identification of relevant scales and the dimensionless groups that describe the system in Sect.4.2.2. Next, numerical-method-specific details and choices for the two aforementioned approaches are discussed in Sect. 4.3. The numerically obtained results are then presented and discussed in Sect. 4.4. Finally, the conclusions of the work herein are presented in Sect. 4.5. This is supplemented with the Appendix that details on the performed numerical simulations, and lists links to online locations that present an precise description of the methods that were used.

4.2 A Simplified model for the diurnal cycle and its non-dimensional representation

In this section, we discuss the idealized description of the physical forcings and the initial conditions that govern the present conceptual model for the diurnal cycle. Next, the scenario is a priori analyzed and casted into a dimensionless form. Thereafter, the choices that are specific to the numerical methodologies are presented for a single-column (RANS) model and the LES study. Furthermore, some considerations for a DNS are presented. Although, this work does not present any results obtained from DNS, those considerations are relevant as they illustrate how the chosen numerical method can introduce method-specific dimensionless groups that govern the dynamics.

4.2.1 Forcing and initial conditions

The forcing of air mass in the ABL is governed by large-scale ($\mathcal{O}\,(1000\ \mathrm{km})$) horizontal circulations and their dynamics. Herein, we only aim to model the ABL over a comparatively small horizontal extent and hence we need to parameterize and idealize the mean wind forcing. Following countless numbers of works, the most prominent wind-forcing mechanism is described as a constant horizontal pressure gradient ($-\nabla_h P$). Furthermore, we include the effect of background rotation with respect to the Coriolis parameter f. With a reference air density ρ and for non-vanishing f, we may conveniently write the pressure-gradient forcing as a velocity vector, U_{geo}, that is known as the geostrophic wind,

$$\overrightarrow{U}_{\mathrm{geo}} = \frac{\hat{\mathbf{k}}}{\rho f} \times \nabla_h P, \tag{4.1}$$

where $\hat{\mathbf{k}}$ is the unit vector in the direction of the zenith. The velocity components in the two lateral ($\{x, y\}$) and vertical (z) direction are labeled $\{u, v, w\}$, respectively, and are initialized in geostrophic balance:

$$\{u, v, w\} = \{U_{\mathrm{geo}}, 0, 0\}, \tag{4.2}$$

where $U_{\mathrm{geo}} = \|\overrightarrow{U}_{\mathrm{geo}}\|$, meaning that the coordinate system is chosen such that the pressure gradient points in the negative y-direction for positive values of f. The persistence of a constant-with-height and constant-in-time pressure gradient and a geostrophic balance in the free atmosphere is part of the model idealization and does not represent the general case of momentum forcing in the ABL. Furthermore, we state explicitly that the velocities at the surface vanish due to the small, yet finite molecular viscosity of the air in the atmosphere. However, the implementation of the surface boundary is argued to be a method-specific feature and the associated treatment is discussed for the different numerical approaches separately in Sect. 4.3.

The forcing of the thermodynamic variable in the ABL is considered to occur at the underlying surface and is described via the sensible heat flux (H). In reality, the partitioning of the available energy among the various terms of the SEB remains a topic of discussion, and is a major challenge for modeling. Therefore, in view of the desired simplicity of our description, we adopt a simplified version of the SEB were we only consider the net radiation (Q_n), the soil heat flux (F_{soil}) and the sensible

heat flux,

$$Q_n = F_{\text{soil}} + H. \tag{4.3}$$

Where Q_n is defined positive towards the surface, and F_{soil} and H are defined positive when directed away from the surface, into the soil and atmosphere, respectively. For generality, we use buoyancy (b) as our thermodynamic variable, and it is related to the potential temperature (θ) according to;

$$b = \frac{g}{\theta_{\text{ref}}} \left(\theta - \theta_{\text{ref}} \right), \tag{4.4}$$

where g is the acceleration due to gravity and θ_{ref} a constant reference potential temperature such that θ_{ref}^{-1} is a sufficient approximation of the thermal expansion coefficient of the (dry) air in the atmosphere. We re-express the SEB Eq. 4.3 for the corresponding buoyancy fluxes: We write Q^*, G and B as the *buoyancy-flux equivalents* to replace the heat fluxes Q_n, F_{soil} and H, respectively;

$$Q^* = G + B. \tag{4.5}$$

These buoyancy-flux terms differ by a factor of $\theta_{\text{ref}} \rho C_p g^{-1}$ from their heat-flux counterparts, where ρC_p is the heat capacity of air at constant pressure, with (constant) density (ρ). In this work, we prescribe the diurnal evolution of $Q^*(t)$ and calculate G at the surface based on a simple closure so that B can be evaluated as a residual. For the soil buoyancy flux (G), we adopt a 'lumped-parameter view' (Van de Wiel et al., 2017). The concept is that there exists a *negative* feedback of heat based on the surface temperature T_s. The main assumption is that this term can be described using an effective feedback-temperature scale T_d and coupling strength λ such that the feedback heat flux F can be expressed according to,

$$F = \lambda \left(T_s - T_d \right). \tag{4.6}$$

Here λ represents the effective combined coupling strength of the surface temperature with T_d due to conductive and radiative processes in the soil and atmosphere, respectively, and hence the name 'lumped parameter'. In this work we only use the concept to model the soil heat flux ($F_{\text{soil}} = F$) such that λ and T_d are model parameters that only concern the soil. This corresponds to a zero-layer model of the soil. The temperature scale T_d can be interpreted as the temperature within the soil at the depth (d) where the diurnal temperature variations are damped out, and λ represents the effective soil and vegetation conductivity. Following Eq. 4.6, G is expressed as,

$$G = \Lambda(b_{\text{surf}} - b_d), \tag{4.7}$$

where Λ is the coupling parameter for buoyancy corresponding to λ, b_{surf} and b_d are the buoyancy-equivalent-to-temperature of T_s and T_d , respectively, see Eq. 4.4.

In practice, heat storage effects (i.e. history), the different properties of the soil layers, the vegetation properties, the phase changes of water, the water-table depth and the actual temperature variations within the soil are important aspects that determine the response of the soil heat flux as a function of T_s over time. In order to stress our simplification, Fig. 4.1 shows the diagnosed λ from data obtained at Cabauw, The Netherlands (Van Ulden and Wieringa, 1996). λ is calculated for each
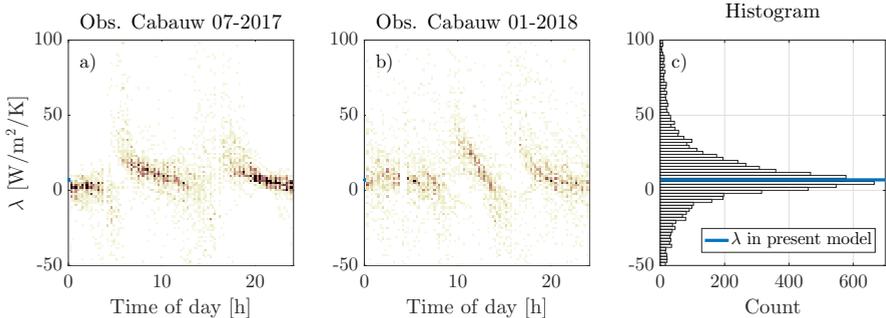
Figure 4.1: Population-density plot of estimated λ values based on observations taken at the CESAR site, in Cabauw, The Netherlands. The plot reveals that λ is highly variable and shows characteristic behavior with respect to the time of day. c) shows the histogram of all shown λ values.

10 min. period based on Eq. 4.6, where we have used the soil temperature at a depth of 30 cm below the surface, the surface (skin) temperature and the heat flux at 5 cm below the surface as T_d, T_s and F_{soil}, respectively. The data show that the concept of a constant-in-time lumped parameter value is not consistent with the observations. Not only does there appear to be a wide spread in the diagnosed λ values, there appears to be a distinctive diurnal pattern (which may be influenced by phase-lag/history effects). The authors stress that our simple evaluation of G is not an alternative to a more elaborated description of the soil physics in models (e.g. Chen et al., 1997; Van Tiggelen, 2018). We argue that it is a specific shade-of-gray in the balance between model system complexity and physical realism, and the results presented in Sect. 4.4 show that it yields model results with some degree of realism and also highlight some prominent limitations.

The temporal variation in the net radiative flux at the surface (Q_n), which is herein considered to be horizontally homogeneous, is the main driver of the diurnal cycle. Q_n is often expressed in models as the sum of its long and short-wave, down and up-welling components. These four terms can be modeled individually using parameterized descriptions for radiation. However, in this work we model a dry, cloud-free day and do not consider radiative divergence within the atmosphere. Due to the smooth and well known characteristics of the evolution of the solar zenith angle, and the limited temperature range within a day, we assume that Q_n has some generic features that may be exploited to arrive at a simple prescription for its time (t) evolution. Therefore, we plot the diurnal evolution of the net radiation for a clear-sky day at Cabauw, the Netherlands, as was observed on 17th of August 2016, in Fig. 4.2. The well-known diurnal pattern is characterized by positive values that reach a maximum during daytime, and during the nighttime, Q_n is more constant in time with negative values. Based on this prototypical evolution we choose to *prescribe*
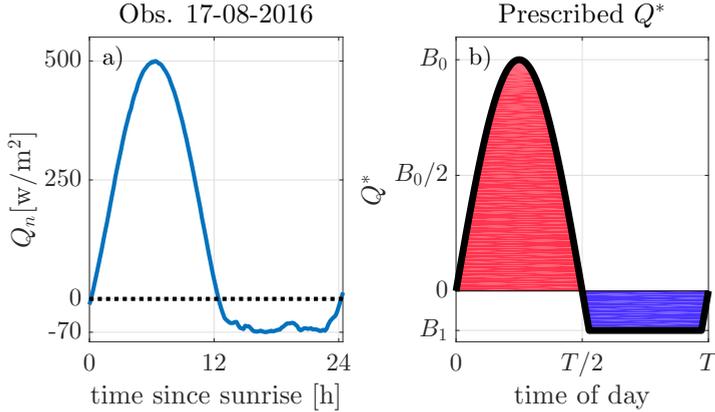
Figure 4.2: Prototypical evolution of the net radiation (Q_n) on a clear-sky day (a) and the prescription of Q^* according to Eq. 4.8 (b).

$Q^* = Q^*(t)$, according to the following functional form;

$$Q^* = \max \left[B_0 \sin \left(\frac{2\pi t}{T} \right), B_1 \right],$$ (4.8)

where B_0. and B_1 are buoyancy-flux scales for the daytime and nighttime, respectively (with $B_0 > 0 > B_1$), $\max[a, b]$ is an operator that selects the maximum value between the dummy variables a and b, and T is the timescale associated with the periodicity of the diurnal cycle (i.e. $T = 24$h on earth). This formulation implies that the daytime section of the cycle (i.e. $Q^* > 0$) is exactly equal to the nighttime part of the day (i.e. $Q^* < 0$). This is typically only accurate for a specific time of the year depending on, among other variables, the location's latitude. For the initialization of the buoyancy field, we consider a stably stratified atmosphere associated with the Brunt-Väisälä frequency N (cf. Garcia and Mellado, 2014; Van Heerwaarden and Mellado, 2016; Mellado et al., 2017),

$$b_{t=0}(z) = b_{\mathrm{surf},t=0} + N^2 z,$$ (4.9)

where z is the height above the surface. Note that the set of buoyancy scales $\{b_d, b_{\mathrm{surf},t=0}\}$ as used in Eqs. 4.7 and 4.9 are important system parameters. However, in order to limit the degrees of freedom of the setups, we only consider the case where,

$$b_d = b_{\mathrm{surf},t=0} = 0,$$ (4.10)

i.e. equal to the buoyancy associated to the reference potential temperature (θ_{ref}), see Eq. 4.4. Furthermore, the finite molecular viscosity (ν) and scalar diffusivity (κ) of the air govern the diffusive processes at the smallest length scales of the atmosphere. However, the treatment of their exact values is considered to be a method specific consideration and it is therefore discussed in Sect. 4.3.

4.2.2 Physical scales and dimensionless groups

In our a priori analysis of the system, we distinguish between relevant scales for the daytime ($0 < t < T/2$) CBL and the nighttime ($T/2 < t < T$) SBL. We assume that $B_0 > 0 > B_1$ and $\|B_0\| \gg \|B_1\|$, as is hinted in Fig. 4.2. In the limit of a vanishing buoyancy flux ($B \to 0$), $Q* = G$. This enables to define two buoyancy scales, $b_{c,\Lambda}$ and $b_{s,\Lambda}$, corresponding to the extreme values for the surface buoyancy for the CBL and SBL period, respectively,

$$b_{c,\Lambda} = \frac{B_0}{\Lambda}, \tag{4.11a}$$

$$b_{s,\Lambda} = \frac{B_1}{\Lambda}. \tag{4.11b}$$

Noting that in general, the assumption of vanishing sensible heat flux is only accurate for the very stable boundary-layer regime (Howell and Sun, 1999). The assumption is particularly unsuitable for the clear-sky convection-driven ABL at mid day (i.e when $Q^* = B_0$). Therefore, we will motivate a more relevant alternative for the daytime buoyancy scale: It is well known that the convective boundary layer is characterized by a well-mixed region with a characteristic buoyancy scale. When we consider the convective limit, with no coupling to the underlying soil ($\Lambda \to 0$), then this buoyancy scale can be evaluated using the total available buoyancy provided by Q^* to uniformly 'heat' the ABL's initial buoyancy profile. If we assume a well-mixed layer in the ABL, and the persistence of the initial stratification aloft, then a CBL with height (L_c) can be associated with a convective buoyancy scale (b_{c,Q^*}),

$$b_{c,Q^*} = N^2 L_c. \tag{4.12}$$

The total time-integrated buoyancy flux during a single day is limited and therefore an upper bound for the values of L_c and b_{c,Q^*} exist. We equate the red-shaded areas in Figs. 4.2 and 4.3 (encroachment principle);

$$\int_0^{T/2} Q^* \mathrm{d}t = \int_0^{T/2} B_0 \sin\left(\frac{2\pi t}{T}\right) \mathrm{d}t =$$
$$= \frac{B_0 T}{\pi} = \frac{b_{c,Q^*} L_c}{2}. \tag{4.13}$$

Combining the equations results in an expression for the CBL height scale L_c and the corresponding buoyancy scale b_{c,Q^*},

$$L_c = \sqrt{\frac{2B_0 T}{\pi N^2}}, \tag{4.14a}$$

$$b_{c,Q^*} = \sqrt{\frac{2B_0 T N^2}{\pi}}. \tag{4.14b}$$

For the SBL, the typical boundary-layer height is a result from the internal dynamics: For example, a very SBL (VSBL) is typically more shallow compared to a weakly SBL (WSBL). Hence, we cannot a priori formulate a relevant expression for the SBL height. However, if we follow a few assumptions, we can find a *reference* length scale for the depth of the SBL (L_s).
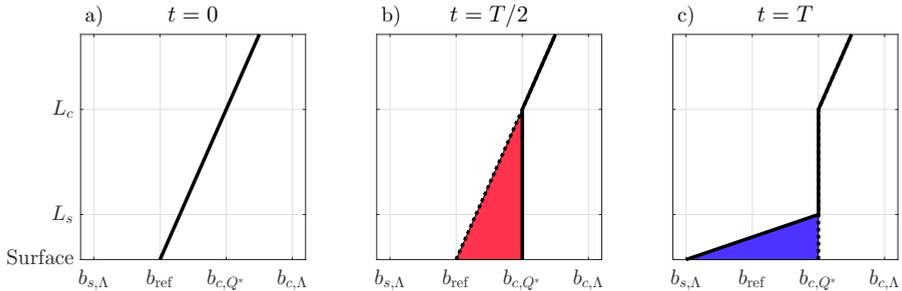
Figure 4.3: Schematic overview of the evolution of the buoyancy profile. The initialized profile (a) and the profiles according to the conceptual model of Sect. 4.2.2 at $t = \{T/2, T\}$, b) and c), respectively.

- The SBL starts to cool from the surface under a well-mixed layer with a buoyancy that is of the order $\mathcal{O}(b_{c,Q^*})$

- The surface buoyancy of the SBL will decrease over the course of the night to be of the order $\mathcal{O}(b_{s,\Lambda})$.

- Within the SBL ($z < L_s$), there is a constant stratification strength N^2_{SBL} such that $b(z) \approx b_{s,\Lambda} + N^2_{SBL} z$ with,

$$N^2_{SBL} = \frac{b_{diurnal}}{L_s},\tag{4.15}$$

with $b_{diurnal}$ a diurnal-buoyancy-range scale based on the first two assumption in this list,

$$b_{diurnal} = b_{c,Q^*} - b_{s,\Lambda}.\tag{4.16}$$

Following the same reasoning as with Eq. 4.13, we assume the blue-shaded areas of Figs. 4.2 and 4.3 to be equal,

$$\frac{L_s b_{diurnal}}{2} = \int_{t=T/2}^{t=T} Q^* \mathrm{d}t \approx \frac{B_1 T}{2},\tag{4.17}$$

and therefore we write,

$$L_s = \frac{B_1 T}{b_{c,Q^*} - b_{s,\Lambda}}.\tag{4.18}$$

Apart from the geostrophic velocity scale (U_{geo}), a relevant velocity-fluctuation scale due to convection can be expressed according to Deardorff (1970),

$$U_c = (B_0 L_c)^{1/3}.\tag{4.19}$$

Similarly we express a *reference* velocity scale for the SBL (cf. Van de Wiel et al., 2012; Van Hooijdonk et al., 2015),

$$U_s = (\|B_1\| L_s)^{1/3}.\tag{4.20}$$

The present system is governed by the set of seven parameters $\{B_0, B_1, T, N, f, \Lambda, U_{\text{geo}}\}$. With two base units (i.e. for length and time), we can identify sets of five independent dimensionless groups that govern the system dynamics (Buckingham, 1915). An example of such a set is,

$$\Pi_1 = \frac{B_0}{B_1}, \tag{4.21a}$$

$$\Pi_2 = TN, \tag{4.21b}$$

$$\Pi_3 = Tf, \tag{4.21c}$$

$$\Pi_4 = \frac{\sqrt{B_0 T}}{\Lambda}, \tag{4.21d}$$

$$\Pi_5 = \frac{U_{\text{geo}}}{U_c}. \tag{4.21e}$$

Here we have chosen to nondimensionalize B_1, N, f and Λ with the daytime forcing parameters B_0 and T, and U_{geo} with the Deardorff velocity scale (U_c). They are formulated such that the values of these groups are typically larger than unity (see Sect. 4.3) . The reference potential temperature θ_{ref}, the acceleration due to gravity g and properties of the air (ρ and C_p) are not additional variables that determine the system dynamics. This is due to the fact that the heat fluxes are expressed in terms of buoyancy fluxes, the case setup and corresponding assumptions. Note that the set of groups in Eqs. 4.21 is based on an arbitrary choice out of infinitely many (equivalent) possibilities and any set of five orthogonal groups can be re-expressed in terms of those presented in Eqs. 4.21 (Vaschy, 1892; Buckingham, 1915).

4.3   Numerical case studies

This section presents the setups for two example studies on the diurnal cycle using both a SCM and an LES approach. Additionally, relevant dimensionless groups for a DNS study are discussed.

4.3.1   An example single-column-model study

For this exemplifying study, we are inspired by the work of Van der Linden et al. (2017), who developed a multi-year climatology of the nocturnal boundary layer at Cabauw, from the perspective of large-scale pressure-gradient forcing. As discussed in depth, our model setup does not aim to capture the conditions to accurately model the ABL at Cabauw. Yet, it is interesting to see what well-known features of the diurnal cycle are realistically reproduced with by the model. As such, we run a suite of model cases where we keep the values for Π_1, Π_2, Π_3 and Π_4 fixed (see Eqs. 4.21), and vary the parameter that controls the pressure-gradient forcing, Π_5.

Associated with the pressure-gradient forcing is the geostrophic wind (U_{geo}), see Eq. 4.1. It is well known that with increasing U_{geo}, the wind shear also increases, which affects the mixing within the ABL. The shear owes its existence to the combination of a mean wind and the fact that velocities vanish at the surface. Since our single-column model does not resolve the turbulent flow near the surface, we rely on a closure that parameterizes the effect of a rough surface as a drag force on the flow.

This warrants the introduction of a so-called roughness length for momentum ($z_{0,m}$) to our setup. We therefore add a sixth dimensionless group that governs the model system,

$$\Pi_6 = \frac{L_c}{z_{0,m}}. \tag{4.22}$$

Furthermore, to compute the buoyancy flux (B), the soil-flux (G) needs to be evaluated using the surface buoyancy(b_{surf}). In our model b_{surf} is found by assuming a logarithmic variation of the buoyancy with height on the sub-grid scale within the lowest two grid cells. A profile may be fitted and the buoyancy can be evaluated at the surface (See the appendix for details). This introduces a roughness length for scalars ($z_{0,h}$), and a corresponding dimensionless group,

$$\Pi_7 = \frac{z_{0,h}}{z_{0,m}}. \tag{4.23}$$

It is commonly accepted that $\Pi_7 \leq 1$, and there is considerable debate in the literature what it value should be. For simplicity, we choose a value of $\Pi_7 = 1$ in this work. Noting that $z_{0,h}$ is related to b_{surf} and that this buoyancy value should be interpreted as an effective surface buoyancy with respect to Eq. 4.7. We choose values for the six groups of Eqs. 4.21 and 4.22 according to the physical parameters listed in table 4.1,

$$b_{c,\Lambda} = 2 \text{ ms}^{-2}, \tag{4.24a}$$
$$b_{s,\Lambda} = -0.33 \text{ ms}^{-2}, \tag{4.24b}$$
$$b_{c,Q^*} = 0.64 \text{ ms}^{-2}, \tag{4.24c}$$
$$b_{diurnal} = 0.97 \text{ ms}^{-2}, \tag{4.24d}$$
$$L_c = 1030 \text{ m}, \tag{4.24e}$$
$$L_s = 170 \text{ m}, \tag{4.24f}$$
$$U_{geo} = [2.3 \text{ ... } 10.6] \text{ ms}^{-1}, \tag{4.24g}$$
$$U_c = 2.3 \text{ ms}^{-1}, \tag{4.24h}$$
$$U_s = 1.5 \text{ ms}^{-1}, \tag{4.24i}$$

and the following values for the dimensionless groups as presented in Eqs. 4.21 and 4.22;

$$\Pi_1 = -6, \tag{4.25a}$$
$$\Pi_2 = 2160, \tag{4.25b}$$
$$\Pi_3 = 10, \tag{4.25c}$$
$$\Pi_4 = 5366, \tag{4.25d}$$
$$\Pi_5 = [1 \text{ ... } 5], \tag{4.25e}$$
$$\Pi_6 = 5150. \tag{4.25f}$$

A SCM solves an evolution equation for the relevant atmospheric vertical profiles according to parameterized descriptions for turbulent transport (Betts, 1986). We use the single-column model that is described in Van Hooft et al. (2018a), based on

Table 4.1: An overview of the parameter values for the physical system that are used in the single-column model study and give rise to the values of the dimensionless groups in Eqs. 4.25

Symbol	Value	Based on
B_0	1.2×10^{-2} m^{2}s^{-3}	$\max{(Q_n)} \approx 360$ Wm^{-2}
B_1	-0.2×10^{-2} m^{2}s^{-3}	$\max{(Q_n)} \approx -60$ Wm^{-2}
T	24 h	The duration of a day
N	0.025 s^{-1}	0.0175 Km^{-1} with $\theta_{\text{ref}} = 280$ K
f	1.15×10^{-4} s^{-1}	Mid-Latitude / Cabauw
Λ	6×10^{-3} ms^{-1}	$\lambda = 7$ Wm^{-2}K^{-1}, Fig. 4.1
U_{geo}	$[2 - 15]$ ms^{-1}	Van der Linden et al. (2017)
$z_{0,m}$	20 cm	Regional Roughness Cabauw

the Basilisk toolbox that is available via `www.basilisk.fr` (Popinet, 2011b). The descriptions for the turbulent transport are based on simple first-order, local, stability dependent K-diffusion closures (Louis et al., 1982; Troen and Mahrt, 1986; Holtslag and Boville, 1993). The mesh-element sizes are varied adaptively, based on the evolution of the numerical solution. For clarity of presentation, this section does not address the details of our model. Therefore, a more elaborated description is presented in the aforementioned work of Van Hooft et al. (2018a) and the appendix. The implementation are documented and freely available. Links to their corresponding online locations are given in the appendix.

4.3.2   An example large-eddy simulation study

The results of the SCM study are supplemented with a 3D turbulence-resolving study that concerns a similar setup as the SCM study, but using a small value for the wind-forcing parameter, $\Pi_5 = 0.5$. This value is chosen small in order to limit the effects of shear on the ABL dynamics, yet large enough to ensure that the closures for the surface transport (i.e. a logarithmic 'law-of-the-wall') remains valid (Sullivan and Patton, 2011; Ansorge, 2018). The values of the other dimensionless groups are taken from the SCM study (see Eqs. 4.25). With an LES approach, one aims to resolve the most dominant (turbulent) flow structures in the atmosphere explicitly, assuming that (1) these govern the overall turbulent dynamics of the ABL, (2) these large turbulent structures decay into smaller structures via a predominantly downward cascade, and (3) these smaller-scale structures are universal and can be parameterized with sufficient accuracy. Such an approach may be preferred over RANS modelling as it yields 3D solution data that explicitly includes the internal variability of the ABL system and reduces the reliance on closures for turbulent transport. However, not the full range of turbulent motions are resolved and this requires an associated model for the sub-grid scale (SGS) turbulent transport. In this work, we parameterize the effects of the SGS turbulent motions to be locally diffusive with an effective eddy viscosity that is calculated based on the formulation of Vreman (2004). Furthermore, at the approach of the surface, the size of the dominant turbulent eddies decreases to

such small (viscous and roughness) scales, that the effect of the underlying surface also needs to be parameterized similar to the SCM approach. The LES domain is a cube of size L_0^3, with $L_0 = 3L_c$ and the lateral boundaries prescribe periodicity of the solution in the horizontal directions. The resulting convective boundary layer depth will grow to be $\approx 0.8L$ (see Sect 4.4). The aspect ratio of the horizontal periodicity and the vertical length scale (approx. 3.75 : 1) is in the 'dangerzone', as there is the risk of large plumes interacting with themselves across the periodic boundaries (Schmidt and Schumann, 1989; Van Heerwaarden and Mellado, 2016). For this preliminary study, we do not study the effects of the chosen horizontal domain size on the dynamics (as in: de Roode et al., 2004). The mesh-element sizes are varied adaptively based on the evolution of the solution for the buoyancy and the three velocity-component fields (Popinet, 2011b; Van Hooft et al., 2018d). The mesh resolution is an important parameter when assessing the fidelity of an LES result (Sullivan and Patton, 2011; Van Stratum and Stevens, 2015). As such, the details for the LES setup, including the resulting mesh-size distribution, are presented in the appendix.

4.3.3 Towards a direct numerical simulation study

For the 3D LES study we have adopted a parameterized description for the drag at the surface and the mixing by SGS turbulence. It is well known that the assumptions for a LES are not generally valid and that SGS models may fail to describe the turbulent mixing with sufficient accuracy for all atmospheric conditions (Mellado et al., 2018; Ansorge, 2018). Alternatively, one may aim to solve the set of equations for fluid motion directly, without adopting a closure for the turbulent transport (Moin and Mahesh, 1998). This entails that the flow needs to be resolved down to the length scales of the turbulent cascade where gradients are sufficiently large such that the molecular diffusion becomes an effective dissipation mechanism for the second order moments of momentum and buoyancy. This warrants the introduction of the fluidâĂŹs viscosity (ν) and thermal diffusivity (κ), which introduces a dimensionless group that is known as the molecular Prandtl number.

$$Pr = \frac{\nu}{\kappa}. \tag{4.26}$$

From the seminal work of Kolmogorov (1941), we learned that the smallest relevant flow-structure scales for the inertial subrange of turbulence are dictated by the dissipation rate of turbulent kinetic energy (ϵ) and the fluid's molecular viscosity (ν). It is known as the Kolomogorov, viscous or dissipation length scale (η) and may be written based on dimensional analysis (Buckingham, 1915),

$$\eta = \frac{\nu^{3/4}}{\epsilon^{1/4}}. \tag{4.27}$$

In order to assess the feasibility of performing a DNS of the present diurnal cycle setup, in the limiting case where there is a total absence of wind forcing (i.e $U_{\text{geo}} = 0$), we follow the works of Garcia and Mellado (2014); Van Heerwaarden and Mellado (2016), and approximate the maximum value of ϵ as a fraction of order one of B_0. We can then define a dimensionless group as the four-thirds power of the scale separation,

that is known as the Reynolds number (Re),

$$Re = \left(\frac{L_c}{\eta}\right)^{4/3} = \frac{B_0}{\nu}\left(\frac{2T}{\pi N^2}\right)^{2/3} = \frac{U_c L_c}{\nu}. \tag{4.28}$$

Typical atmospheric conditions are characterized by $U_c = \mathcal{O}\left(1\ \mathrm{ms}^{-1}\right), L_c = \mathcal{O}\left(1\ \mathrm{km}\right)$ and furthermore, $\nu \approx 1.5 \times 10^{-5}\ \mathrm{m^2s^{-1}}$ meaning that $Re = \mathcal{O}\left(10^8\right)$ and the minimum resolution ($\Delta_{\min} = \mathcal{O}\left(\eta\right)$) would then need to be ($\Delta_{\min} = \mathcal{O}\left(10^{-6}L_c\right)$) on the order of millimetres. This is not feasible for 3D turbulence resolving studies and may remain elusive for a considerable period in the future (Bou-Zeid, 2015). Therefore, in virtually all studies that employ DNS for ABL flows, an offer is made with respect to the Reynolds number, assuming that for sufficiently large values of Re, certain relevant (scaled) statistics become insensitive to its exact value, a concept known as 'Reynolds-number similarity'. Similar to the LES approach, it is assumed that the full depth of the inertial subrange of isotropic turbulence does not need to be resolved to obtain accuracy for the lower-order solution statistics. However, with the available resources for this preliminary study, we cannot perform a DNS with a reasonable value for Re of the full diurnal cycle and hence, this work does not present any results obtained with the DNS technique. Further, heat fluxes in such a simplified representation of the ABL do not scale inviscidly (cf. Van Heerwaarden and Mellado, 2016; Van Hooijdonk et al., 2018), i.e. they have to be normalized with account for changes in Re. This requires a thorough analysis of the viscid scaling behavior of $\Pi_1 - \Pi_5$.

4.4 Results and Discussion

4.4.1 Single-column model results

Since the SCM approach employs semi-empirical descriptions of the turbulent transport, the obtained evolution of the vertical profiles are subject to the particular choices regarding the used closures. As such, the results presented in this section are only intended to provide a qualitative overview of the modeled dynamics. Figure 4.4 presents the results from the simulation run with $\Pi_5 = 3.5$ and provides a prototypical example of the evolution of the vertical profiles with a time interval $\Delta t = T/12$ (corresponding to a two-hourly interval). We observe that the for this case, the depth of the well-mixed layer grows during the daytime to the order of L_c with a characteristic buoyancy that is a fraction of order one of b_{c,Q^*}. During the night, a SBL forms that has a depth of the order of L_s (c.f. Eq. 4.18). As the SBL is shear driven, the shapes of the nighttime profiles are more sensitively responding to the value of Π_5 compared to their daytime counterparts (not shown).

Figure 4.5 shows the partitioning of the available buoyancy (Q^*) between the buoyancy flux (B) and the soil flux (G) for two runs with different pressure-gradient forcing (i.e. $\Pi_5 = \{2,5\}$). It can be observed that for the daytime results, there are hardly any differences, as thermodynamics are dominated by convection. At the end of the day time ($t \approx T/2$), the buoyancy flux changes from positive to negative values before Q^* does so (cf. Van der Linden et al., 2017). At night however (i.e. $B < 0$), the weak wind speeds cause the buoyancy flux to be close to zero and the radiative
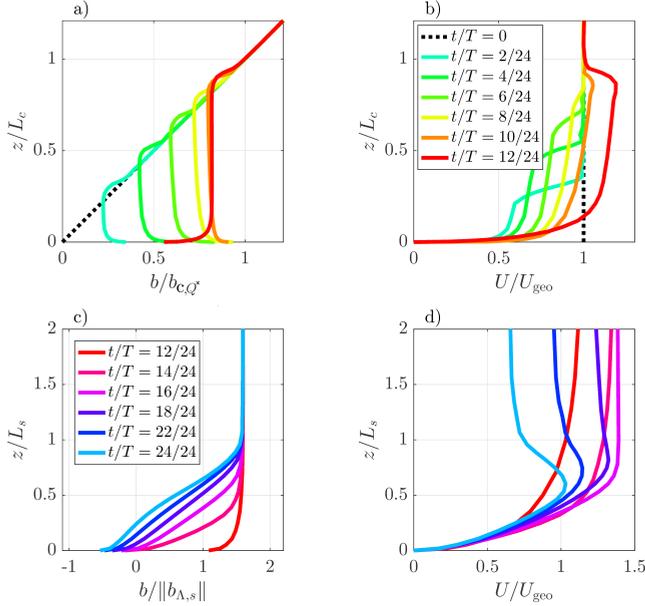
Figure 4.4: The solution profiles obtained for the single-column model run with $\Pi_5 = 3.5$. The plots display the profiles of the daytime the buoyancy (b) and the horizontal wind magnitude (U) in panel a and b, respectively. Panels c) and d) display the same quantities for the nighttime. Notice the different scaling of the axis for daytime and nighttime data. For reference; all panels show the corresponding profile at $t = T/2$ (red line).

buoyancy/energy loss is compensated by the soil flux (G), corresponding to a VSBL. Alternatively, for the strong-wind case (i.e $\Pi_5 = 5$), the soil flux remains small in the SBL and the radiative loss of energy is mostly compensated by the buoyancy flux (B), corresponding to a WSBL (compare e.g. observational data presented in Van de Wiel et al., 2003). Remarkably, the simple setup appears sufficient to retrieve the dynamical difference between the VSBL and the WSBL due to variations in the pressure-gradient forcing. Inspired by this result, we explore the transition between the VSBL and WSBL as a function of Π_5 and plot the difference of buoyancy at the surface and at $z = L_c/20$ (Δb). This inversion is averaged over the 19th hour of simulation (i.e. in the middle of the night) and the results are plotted in Fig. 4.6 a. It appears that for the low pressure-gradient forcing the inversion is of the order one of the anticipated diurnal buoyancy range ($b_{diurnal}$). In literature that concern observational analysis, the large scale pressure-gradient forcing is commonly not available and the inversion strength is often plotted against a wind speed within the boundary layer. As such, we average the wind speed at $z = L_c/20 \equiv 50$ m over the same period and the results are plotted in Fig. 4.6 b. Here we see that the transition between the WSBL and VSBL appears much sharper. This is due to the non-linear
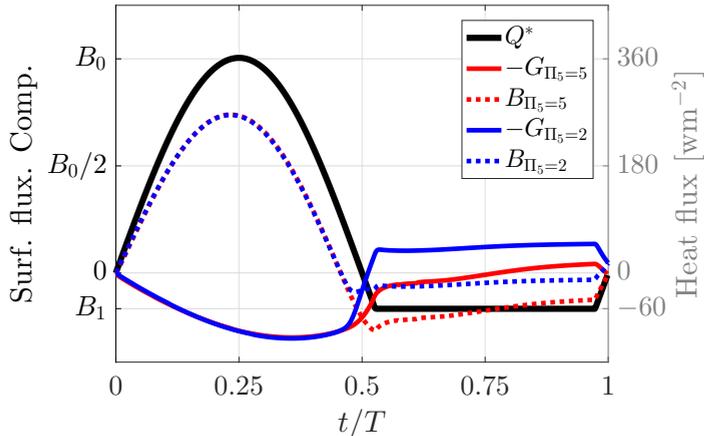
Figure 4.5: The diagnosed buoyancy flux (B), the soil heat flux (G) and the prescribed net radiation (Q^*) obtained from two runs, each with different Π_5 value ($\Pi_5 = \{2, 5\}$). The differences due to the wind forcing are most notable in the stable boundary layer regime (i.e. $t > T/2$). After the occurrence of a buoyancy flux minimum, the sensible heat flux vanishes for the case with the weaker wind forcing, wheasreas it remains finite for the case with the stronger forcing case.

response of the wind speeds within the SBL to U_{geo}. For a more in-depth analysis of this aspect see; Baas et al. (2019).

Finally, In order to point out a limitation of the model scenario with respect to its ability to describe reality, we focus on the evolution of the buoyancy near the surface ($b(z, t) = b(L_c/50, t)$) in Fig. 4.7 for the run with a value of $\Pi_5 = 4$. For a comparison, we plot the evolution of the absolute temperature at $z = 20$m for five consecutive days at the CEASAR observational site in Cabauw, The Netherlands. Data is plotted for the 19th to the 23rd of August 2018. These days are associated with a heat wave and a drought in the Netherlands. These data therefore provide a reference for diurnal cycles with a limited influence of the moist dynamics. Neglecting the actual diurnal temperature range, we see that the overall shape of the observations is captured to some degree in the model. However, during the transition from the CBL to the SBL, the cooling rate predicted by the model is (comparatively) too large. This may be due to the fact that the used closures fail to represent the mixing of decaying turbulence and/or the fact that the soil heat flux description in our model is particularly unsuitable for this period of the day (cf. Fig. 4.1). To assess this discrepancy we have run the model with a full (i.e. layered) soil model such that heat-storage effects are explicitly taken into account. An alternative model where we have used the so-called 'enhanced mixing' formulation under stable conditions is also run (Holtslag and Boville, 1993). The cooling rate at $t \approx T/2$ is smaller than with the present Λ-based description of the soil flux (G), c.f. Eq. 4.7. This is due to significant effects of soil-heat storage: the temperature of the upper soil is higher than that of e.g. the deep soil (T_d) in Eq. 4.6, see Fig. 4.7 c. Therefore, heat
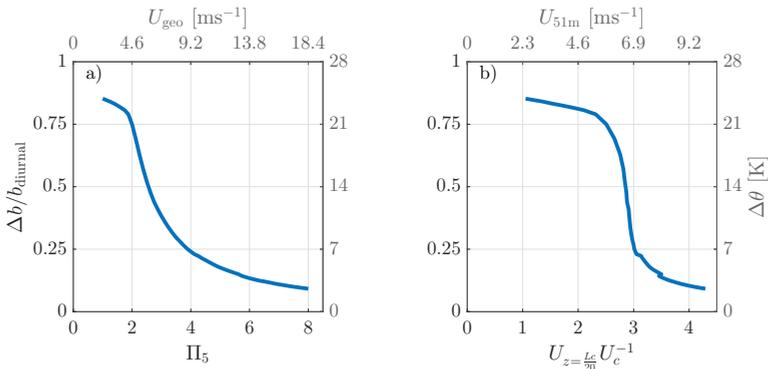
Figure 4.6: The buoyancy inversion (Δb) between the surface and at $z = L_c/20$ averaged over the 19th hour of simulation obtained from runs with different pressure-gradient forcings (i.e. Π_5). Δb Is plotted against the pressure forcing parameter Π_5 (a) and against the 19th-hour average of the horizontal wind speed at $z = L_c/20; U_{z^{L_c}/20}$ (b). The dimensionless numbers on the lower and left-hand side x and y axis are converted to their meteorological equivalents using the values of table 4.1 and are displayed on the corresponding upper and right-hand-side axis (in grey).

is released into the atmosphere. It can also be observed that the model using the enhanced mixing formulation does indeed predict a slower cooling rate. However, even with this mixing, the rapid cooling during the transition remains, which stresses the importance of an accurate representation of ground heat storage. As such, the present 'lumped parameter' model may be a poor representative of reality during the transition period itself (cf. Fig. 4.1).

4.4.2 Large-eddy simulation results

In this section we give an overview of the evolution of the resolved turbulent structures in the ABL during the diurnal cycle with the present framework, containing coupled surface boundary conditions. Due to our low value for Π_5, turbulence is weak during the night and the main actors in the SEB are Q^* and G (see Fig. 4.5). Correspondingly, there are no appreciable turbulence levels in the simulated SBL and the authors argue that in the absence of large eddies, the assumptions that underlie the LES approach may not hold for this period. Therefore, we focus our analysis on the growth and decay of the CBL and we only briefly consider the day-night transition. The SBL itself is left for a more in-depth future study. As we have not prescribed the evolution of buoyancy at the surface, the internal variability of the atmospheric dynamics give rise to a heterogeneous surface buoyancy structure. We plot horizontal slices of the surface buoyancy for the part of the day where the CBL is growing in Fig. 4.8. It appears that initially, at $t/T = 1/48$, the surface buoyancy structures are organized in elongated 'streets', whereas at later stages, the foot print of horizontally
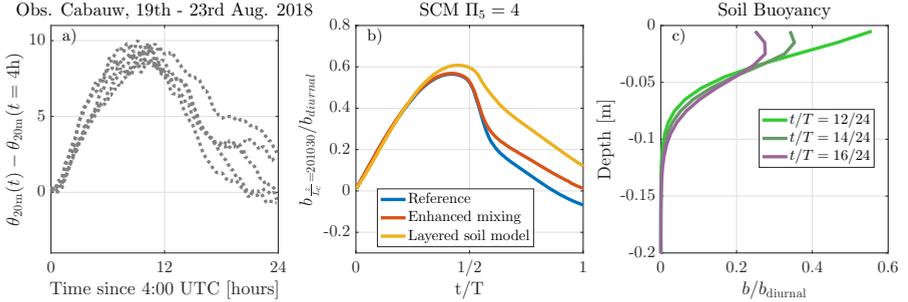
Figure 4.7: The evolution of the temperature at $z = 20$ m for five consecutive clear-sky and relatively dry days with a pronounced diurnal pattern, at Cabauw, The Netherlands (a) and the modeled buoyancy at $z = {}^{L_c}/50 \equiv 20$ m obtained from three different models (b, see text Sect. 4.3). It appears that at the onset of the stable boundary layer ($t \approx {}^{T}/2$), only the model that includes heat-storage effects (yellow line) is able to predict a realistic cooling rate. The corresponding soil-buoyancy profiles (c) are displayed for various times during the day-to-night transition. These profiles reveal that after the transition, the soil is releasing heat into the atmosphere.

isotropic convection cells are observed. This can be explained by the fact that in the early-morning, convection is still weak compared to the shear in the boundary layer. It is known that shear dominated convection tends to organize in elongated surface 'streaks' (Adrian, 2007) or convective 'rolls' (Coleman et al., 1994; de Roode et al., 2004; Conzemius and Fedorovich, 2006; Gibbs and Fedorovich, 2014). As the buoyancy flux and the boundary-layer height increase, this balance shifts to a convection dominated regime. Furthermore, with an increase of the CBL depth over time, the size of the convection cells also grows and this is reflected by the structures in the surface buoyancy. Apart from the largest-cell structures, smaller filaments can be observed. Within the CBL, thermal plumes rise and this process may be visualized by plotting 3D renderings of a isosurface of the buoyancy colored with the local vertical velocity. Figure 4.9 presents such rendering at two stages for the growth of the CBL. The isosurface of the buoyancy is chosen such that it is representative of cores of the thermal plumes and a layer with an identical buoyancy value is found aloft in the inversion layer. It can be observed that at $t/T = 1/24$ there exist many convective plumes within the domain that cause a wave pattern in the overlaying inversion layer. At a later stage (i.e. $t/T = 6/24$) the thermal plumes have grown in size. The snapshot in Fig. 4.8 b) also depicts the process of entrainment (arrow) as we see the isosurface of the buoyancy in the inversion layer being entrained downward to be within the CBL. Finally, 1700 consecutive snapshots of the turbulent structures in the solution field are combined into a movie. It is made available via Vimeo: https://vimeo.com/292329175.

An important characteristic of convective boundary layers is that it may display self-similar behaviour over a range of CBL heights ($\mathcal{L}_c$) and convective velocity scales $\mathcal{U}_c$ (Jonker et al., 2013). For the well-mixed-layer height growing into a linear strati-

a) $t/T = 1/48$
$\langle b \rangle = 0.15$, $\sigma_b = 0.017$

b) $t/T = 3/48$
$\langle b \rangle = 0.47$, $\sigma_b = 0.045$

c) $t/T = 7/48$
$\langle b \rangle = 1$, $\sigma_b = 0.081$

d) $t/T = 11/48$
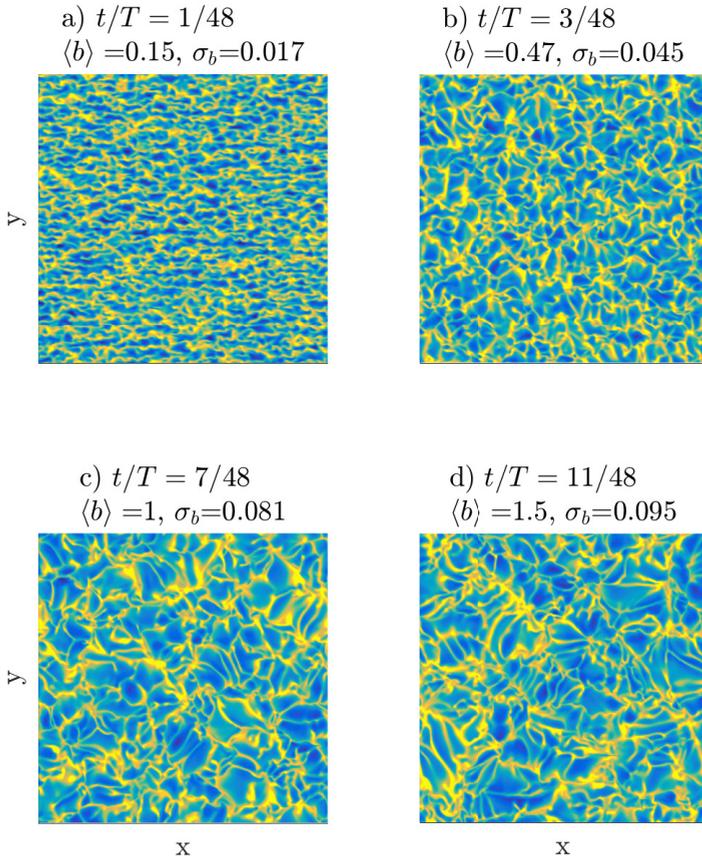$\langle b \rangle = 1.5$, $\sigma_b = 0.095$

Figure 4.8: Slices of the buoyancy field at the surface during the initial growth of the CBL at times $t/T = \{1/48, 3/48, 7/48, 11/48\}$, in panel a) b) c) and d), respectively. The panel title denotes the average ($\langle b \rangle$) and the standard deviation (σ_b) of the slice. The color axis range from $\langle b_s \rangle - \sigma_b$ (blue) via $\langle b_s \rangle (green)$ to $\langle b_s \rangle + \sigma_b$ (yellow).
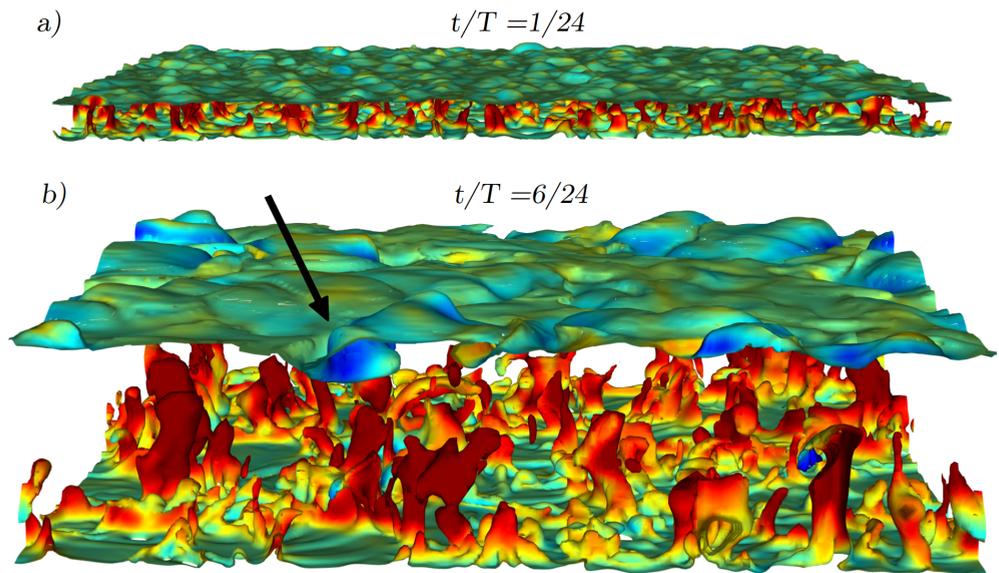
Figure 4.9: Isosurface renderings of the buoyancy field for (a) $t/T = 1/24$ and (b) $t/T = 6/24$, with $b_{\mathrm{iso}}/b_{c,Q*} = \{0.125, 0.64\}$, respectively. The values for the iso surfaces are (subjectively) chosen such that they depict the upward convective motions and the surfaces are colored with the local vertical velocity from red (upward) via green ($w = 0$) to blue (downward). The black arrow in panel (b) annotates the process of boundary-layer entrainment.
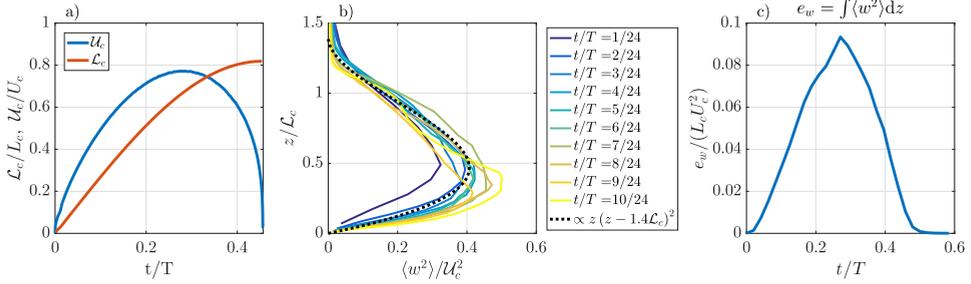
Figure 4.10: The time evolution of the CBL height ($\mathcal{L}_c$) and the instantaneous convective velocity scale ($\mathcal{U}_c$) according to Eqs. 4.29 and 4.30 (a), the vertical (z) profiles of the velocity variance $\langle w^2 \rangle$, plotted for different times and normalized with the external scales $\mathcal{L}_c$ and $\mathcal{U}_c$, respectively, (b). The dashed black line indicates a fit (by eye) of a functional relation for the self-similar profile based on (Troen and Mahrt, 1986). The growth and the subsequent decay of the resolved turbulent motions are quantified by the total height-integrated vertical velocity variance (e_w) (c).

fication ($\mathcal{L}_c$), we follow the definition of Van Heerwaarden and Mellado (2016),

$$\mathcal{L}_c^2 = \frac{2}{N^2} \int_{z_{0,h}}^{z_{top}} \left(\langle b \rangle - N^2 z \right) \mathrm{d}z. \tag{4.29}$$

Based on this length scale, we define the *instantaneous* Deardorff convective velocity scale,

$$\mathcal{U}_c = \left(B\mathcal{L}_c \right)^{1/3}. \tag{4.30}$$

The temporal evolution of these scales is plotted in Fig. 4.10 a) and are used to rescale the vertical profiles of the vertical velocity variance ($\langle w^2 \rangle$) in Fig 4.10 b). Here we see that for the largest part of the daytime a self-similar profile is diagnosed that is described with appreciable accuracy by the well known functional shape as listed in Troen and Mahrt (1986). However, the profiles from the early morning and the later afternoon show clear deviations form the self-similar profile. The shallow early morning CBL may suffer from the limited grid resolution and may also be affected by the relative importance of shear (Conzemius and Fedorovich, 2006). Furthermore, during the late afternoon period, the heat flux vanishes and the convective turbulent structures decay. Hence, it is not expected that the CBL remains self similar nor that Deardorff scale ($\mathcal{U}_c$) is relevant for that period. To obtain an estimate for the growth and decay of the vertical motions, the height-integrated vertical velocity variance ($e_w = \int_{z_{0,h}}^{z_{top}} \langle w^2 \rangle \mathrm{d}z$), averaged for a period $\Delta t = T/48$ is presented in Fig. 4.10 c). In the simulation, the decay of e_w during the day-to-night transition appears to be linear with time. This does not follow the conclusions from any of the more idealized studies on the decay of convective turbulence (Nieuwstadt and Brost, 1986; Sorbjan, 1997; Van Heerwaarden and Mellado, 2016), where several negative scaling exponents with time are proposed to describe the decay of convection. This aspect is not further discussed herein.

Finally, we briefly discuss the surface structure for the buoyancy and surface heat flux of the present setup. We note that there is quite some freedom on how to implement the surface boundary conditions when using a SEB equation. In this work, B is computed as a residual in the SEB, $B = Q^* - G$, were G is evaluated via the buoyancy at the surface (b_{surf}). In turn, the surface buoyancy is computed from fitting a log-linear profile to the local buoyancy field in the lowest two grid points and evaluating the corresponding buoyancy at a height of $z = z_{0,h}$ (see the appendix for details). Even though assuming a logarithmic profile seems to be a robust choice, the main disadvantage of this approach is that the exact value of $z_{0,h}$ becomes an important parameter to obtain b_{surf} . Alternatively, a method taken from the TESSEL/HTESSEL land-surface model (Balsamo et al., 2009; Maronga and Gehrke-Scharf, 2018) has successfully been employed in the LES study by Maronga and Bosveld (2017). Here the surface temperature is computed as the temperature that closes a (more extensive) SEB equation, where the individual terms are a function of T_{surf}. Remarkable, an inconsistency arises between the two methods: With the present model formulation, the correlation between the instantaneous fluctuations in the surface buoyancy field and the surface buoyancy flux (i.e. b'_{surf} and B') are linked via Λ. This is because the regions with a warmer surface correspond to a heat flux towards the soil (G), and vice versa. Hence,

$$B' = -\Lambda b'_{surf}.$$ (4.31)

Alternatively, the TESSEL/HTESSEL formulation computes the sensible heat flux H according to a resistance law (i.e. bulk transfer model),

$$H = \rho C_p \frac{1}{r} \left(\theta_{surf} - \theta_1 \right),$$ (4.32)

Where θ_{surf} and θ_1 are the potential temperature at the surface and the first model level, respectively, and r is the aerodynamic resistance which is computed based on a Monin-Obokhov-style closure. In practice, Eq. 4.32 causes a *positive* correlation between the fluctuations in H and in θ_{surf}, as warmer surfaces transport heat more effectively towards the atmosphere (Van Tiggelen, 2018). Although this seems reasonable, we argue that the formulation of Eq. 4.32 was designed for weather forecasting models where the resolved spatial scales are much larger than individual convection cells. Whereas the LES approach applies its closures for the variations within a convection cell, which are governed by different dynamics. Figure 4.11 shows an illustrative representation for the convergence of warm air near the surface towards the base of a convection cell. At the base, the surface temperature is at a local maximum and at some height above the surface, this is where the heat flux is indeed large. However it is not obvious how the fluctuations, albeit small, in temperature and sensible heat flux *at the surface* relate to each other. With the advent of convection permitting weather models (Prein et al., 2015) and the usage of LES for weather prediction (e.g. Heinze et al., 2017), a proper description is needed. This may be based on the results from a dedicated observational campaign and/or direct numerical simulations of the near-surface heat transport that includes the heat exchange with the soil.
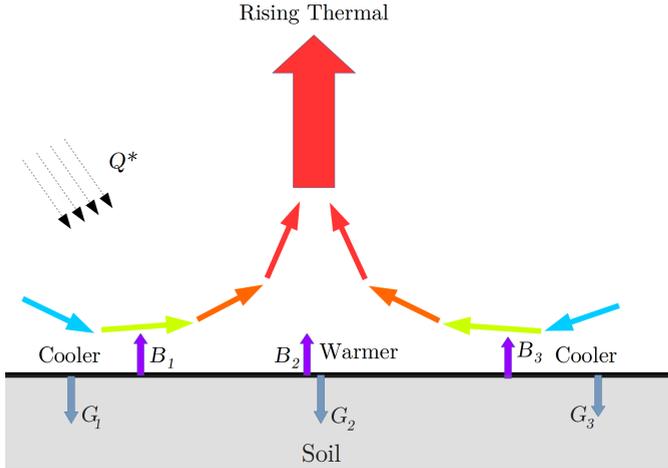
Figure 4.11: A schematic overview of a rising thermal: The surface is heated by the available energy (Q^*) and this causes a positive buoyancy flux (B), resulting in the heating of the atmosphere. The resulting unstable stratification tends to organize a flow where warm air convergences towards the the basis of a rising thermal plume. These rising motions are directly related to the sensible heat flux $(\langle w'b' \rangle)$. At the same time, the soil is heated (G).

4.5   Conclusions

In this work, we have presented a conceptual model for the diurnal cycle of the dry atmospheric boundary layer (ABL). The corresponding forcing parameters can be described with only five dimensionless groups and this provides a convenient framework to study cause-and-effect relations for the effects of the various forcing mechanisms on the ABL dynamics. Relevant scales for the boundary-layer height and atmospheric buoyancy values are derived from the model. Furthermore, the model served as a setup for numerical simulations. This aspect is illustrated for the atmospheric single-column model and a large-eddy simulation techniques.

The results from the preliminary study that used a single-column model showed that the difference between the weakly stable and very stable boundary layer are dynamically retrieved for variations in the wind forcing. This is a key result of the present work and shows that interesting physics can be present in a model that only has a low degree of complexity and low number of input parameters. A large-eddy simulation for a diurnal cycle with weak-wind forcing showed how, for this case, convective structures grow and retain their statistically self-similar structure throughout the day. Furthermore, the decay of residual turbulence in the late afternoon-to-evening transition was quantified. The integrated vertical velocity variance appeared to decay linearly with time.

Limitations of the present description were also identified. Due to the non-physical nature of the lumped-parameter (Λ) to describe the response of the soil to varying

surface temperatures, so-called history-effects are not modeled. These effects appear to play an important role in the day-night transition. Furthermore, for the three-dimensional simulations, the model predicts a heterogeneous surface buoyancy and surface buoyancy flux. However, by design, deviations from the means of these two quantities are perfectly anti correlated. This may not be accurate, but we argue it remains unclear how to accurately model the soil response in an LES.

We conclude that the present conceptual model provides additional insight to the classical ('Stullian') view of the diurnal cycle ((Stull, 1988)), as it enables to define expressions for relevant physical scales that characterize the diurnal cycle. The dimensionless description can be useful to generalize the dynamical behavior of the ABL. Finally, we foresee that more in-depth numerical studies, based on the present idealized forcings for the ABL, can help to better understand the interactions between the most prominent processes that govern the diurnal cycle.

Appendix: Numerical model setups

In this section we discuss the details regarding the single-column model (SCM) and Large-eddy simulation (LES) setups. The exact implementation of the described approaches are documented and made available online via:
http://www.basilisk.fr/sandbox/Antoonvh/READMEwww.basilisk.fr/sandbox/Antoonvh/
SCM: www.basilisk.fr/sandbox/Antoonvh/diurnalSCM.cdiurnalSCM.c
SCM + soil: www.basilisk.fr/sandbox/Antoonvh/diurnalSCMsoil.cdiurnalSCMsoil.c
LES: www.basilisk.fr/sandbox/Antoonvh/diurnalLES.cdiurnalLES.c

The single-column model

The single-column model (SCM) solves an evolution equation for the vertical profiles of the horizontal velocity components (u, v) and the buoyancy (b) according to a parameterized description for turbulent mixing.

$$\frac{\partial u}{\partial t} = fv + \frac{\partial}{\partial z}\left(K\frac{\partial u}{\partial z}\right) \tag{4.33a}$$

$$\frac{\partial v}{\partial t} = f\left(U_{\mathrm{geo}} - u\right) + \frac{\partial}{\partial z}\left(K\frac{\partial v}{\partial z}\right) \tag{4.33b}$$

$$\frac{\partial b}{\partial t} = \frac{\partial}{\partial z}\left(K\frac{\partial b}{\partial z}\right), \tag{4.33c}$$

where U_{geo} is the geostrophic wind, f the Coriolis parameter (c.f. Eq. 4.1) and K the eddy diffusivity. The latter is parameterized according to,

$$K = lV^*, \tag{4.34}$$

With l the Blackadar length scale and V^* a velocity scale due to shear and convection. For l we write,

$$l = \min\left[kz, 70 \text{ m}\right], \tag{4.35}$$

with $k = 0.4$ the Von Kármán consant. For V^* we depart from the work of Van Hooft et al. (2018a) as we do not only include the effects of shear, but also model mixing

due to convective motions. We follow the work of (Troen and Mahrt, 1986),

$$V^* = \sqrt{w_c^2 + (lSf(Ri))^2},$$
(4.36)

where w_c is the local convective velocity scale that is parameterized using,

$$w_c = 3\mathcal{U}_c \frac{z}{\mathcal{L}_c} \left(1 - \frac{z}{\mathcal{L}_c}\right)^2,$$
(4.37)

where $\mathcal{L}_c$ and $\mathcal{U}_c$ are computed via Eqs. 4.29 and 4.30. The shear magnitude (S) is evaluated as,

$$S^2 = \left(\frac{\partial u}{\partial z}\right)^2 + \left(\frac{\partial v}{\partial z}\right)^2,$$
(4.38)

and $f(Ri)$ is the stability-dependent mixing function,

$$f(Ri) = \begin{cases} e^{-10Ri}, & \text{for } Ri > 0 \\ \sqrt{1 - 18Ri}, & \text{for } Ri \leq 0, \end{cases}$$
(4.39)

i.e. based on the gradient Richardson number (Ri),

$$Ri = \frac{\partial b/\partial z}{S^2}.$$
(4.40)

For the enhanced mixing experiment, we use the so-called âĂŸlong tailâĂŹ formulation (Louis et al., 1982),

$$\text{Enhanced}: \ f(Ri > 0) = \frac{1}{1 + (10Ri\,(1 + 8Ri))}.$$
(4.41)

The drag at the bottom surface is based on a near-neutral logarithmic law-of-the wall, and we express the friction velocity (u_τ) as function of the bottom-grid-cell averaged value of u (labeled u_1).

$$u_\tau = \frac{u_1 k}{\ln\left(\frac{\Delta}{z_{0,m}}\right)},$$
(4.42)

which follows directly from integrating the law-of-the-wall over the lowest cell with size $\Delta \gg z_{0,m}$. A logarithmic law of the wall is also applied for the buoyancy profile in the lowest two grid cells. This results in an expression for b_{surf},

$$b_{surf} = \frac{b_2 - b_1 c}{1 - c},$$
(4.43)

with b_1 and b_2 the cell averaged values of b in the lowest two cells. The value of c results from an integration exercise,

$$c = \frac{\ln\left(\frac{4\Delta}{z_{0,h}}\right)}{\ln\left(\frac{\Delta}{z_{0,h}}\right)},$$
(4.44)

where we have assumed that the lowest two cells have a vertical size of Δ and $\Delta \gg z_{0,h}$, the roughness length for heat. The surface buoyancy flux $B = Q^*(t) - G$ can then be readily evaluated. The domain has a height of $z_{top} = 3L_c$ and the mesh-element sizes are adaptively varied down to a maximum resolution of $\Delta_{\min} = z_{top}/512 \equiv 6$ m, based on the estimated discretization error in the representation of the solution fields for u, v, and b (Popinet, 2011b; Van Hooft et al., 2018a). The corresponding refinement-criteria values are: $\zeta_{u,v} = U_{\text{geo}}/20$ and $\zeta_b = b_{diurnal}/50$. These values resulted from a convergence study and aim to strike an arbitrary balance between accuracy and the number of grid cells (Van Hooft et al., 2018a).

The layered soil model

For the SCM run with a layered soil model (see Fig. 4.7), the flux ($G = G_{\text{soil}}$) is described via a conduction layer on top of a soil.

$$G_{\text{soil}} = -A\left(b_{surf} - b_{soil,top}\right), \tag{4.45}$$

with A a conductivity. The buoyancy value at the soil top was found by linear extrapolation of the top two cell-averaged buoyancy values (b_{-1} and b_{-2}) in the fixed and equidistant grid:

$$b_{soil,top} = \frac{3}{2}b_{-1} - \frac{1}{2}b_{-2}. \tag{4.46}$$

The layers have a buoyancy-equivalent-to-heat-capacity $(\rho c_v)_{soil} = 1000 \times (\rho c_p)_{air}$, a diffusivity $\kappa_{soil} = 5 \times 10^{-5}$ m^{2}s^{-1} and the conductivity $A = 2 \times 10^{-3}$ ms^{-1}.

The large-eddy simulation

The Large-eddy simulation (LES) solves the following equations for incompressible-fluid motion via the (filtered) velocities ($\mathbf{u} = \{u, v, w\}$), the modified pressure (p) and the buoyancy (b),

$$\frac{\partial u}{\partial t} + \mathbf{u} \cdot \nabla u = -\frac{\partial p}{\partial x} + fv + \nabla \cdot (K\nabla u), \tag{4.47a}$$

$$\frac{\partial v}{\partial t} + \mathbf{u} \cdot \nabla v = -\frac{\partial p}{\partial y} + f\left(U_{\text{geo}} - u\right) + \nabla \cdot (K\nabla v), \tag{4.47b}$$

$$\frac{\partial w}{\partial t} + \mathbf{u} \cdot \nabla w = -\frac{\partial p}{\partial z} + \nabla \cdot (K\nabla w) + b, \tag{4.47c}$$

$$\nabla \cdot \mathbf{u} = 0, \tag{4.47d}$$

$$\frac{\partial b}{\partial t} + \mathbf{u} \cdot \nabla b = \nabla \cdot (K\nabla b). \tag{4.47e}$$

The eddy diffusivity (K) is evaluated according to the sub-grid scale model of Vreman (2004) and at the bottom surface the law-of-the-wall sub-grid scale model is applied to the horizontal momentum and buoyancy, identical to the SCM (c.f. Eqs. 4.42 and 4.43). Time integration is carried out via a classical fractional time-step algorithm, for details see Castillo-Castellanos (2017); Popinet (2018). The spatial discretization follows the finite-volume methodology, employing cubic-cells to mesh the cubic ($3L_c \times$

$3L_c \times 3L_c$) domain using an octree grid structure. A damping layer in active in the top half of the domain. The octree grid allows grid-cell sizes to vary by factors of two (Popinet, 2011b). In order to resolve the largest eddies, those that dominate the dynamics, the tree grid is locally refined and coarsened adaptive to the prevailing situation. Each timestep, a multiresolution analysis is performed to *estimate* the local deviation from a spatially linearly varying test function. This deviation is computed for all velocity components ($\chi_{u,v,w}$) and the buoyancy field (χ_b). Grid refinement is carried out when the χ value exceeds the corresponding refinement criterion ($\chi > \zeta$), with a maximum resolution corresponding to a 256^3-cell equidistant grid. Cells may be coarsened when $\chi < \frac{2}{3}\zeta$, with the additional requirement that the coarse cell 'fits' the hierarchical grid structure (Van Hooft et al., 2018d). In order to properly take into account the time-varying nature of the daytime convection, the refinement criteria are dynamically evaluated as fractions of the Deardorff velocity and buoyancy fluctuation scale (for $B > 0$),

$$\zeta_{u,v,w} = \max\left[\frac{\mathcal{U}_c}{c_u}, \zeta_{\min,u}\right], \tag{4.48a}$$

$$\zeta_b = \max\left[\frac{\left(B^2/\mathcal{L}_c\right)^{1/3}}{c_b}, \zeta_{\min,b}\right]. \tag{4.48b}$$

Here c_u and c_b are dimensionless constants that may be tuned to balance accuracy (via grid resolution) versus computational speed. We have chosen $c_u = 2$ and $c_b = 1$ and furthermore, $\zeta_{\min,u} = U_c/10$ and $\zeta_{\min,b} = \frac{\left(B_0^2/L_c\right)^{1/3}}{5}$. The authors of this work realize that hinting at the accuracy of a simulation via ζ is unconventional compared to listing a fixed mesh-element size (see Van Hooft et al., 2018a). Therefore, Fig. A1 displays the horizontally-averaged effective resolution, presented via the corresponding number of equidistant-grid cells. Furthermore, Fig. A2 presents a horizontal and vertical slice of the grid at mid day (i.e. $t/T = 6/24$). It can be observed that the mesh elements are dynamically focused on the surface layer, the entrainment and inversion layer and towards the decay of convective turbulence. Furthermore, At the late stage of the simulation, the internal waves in the free troposphere are the most dynamically active process. The grid slices in Fig. A2 reveal that within the CBL, a high resolution is employed to resolve the cores of the thermal plumes.
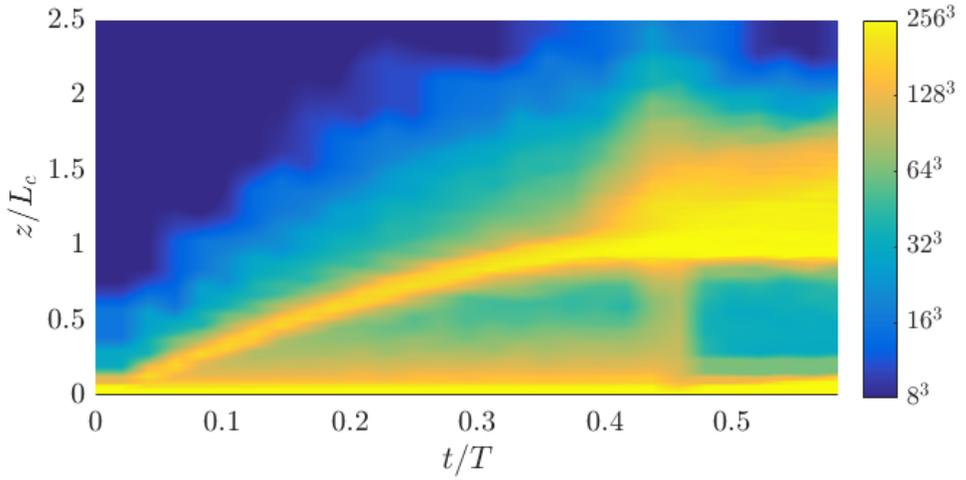
captionA1: The evolution of the *equidistant-grid equivalent* number of cells as a function of height (horizontally averaged).
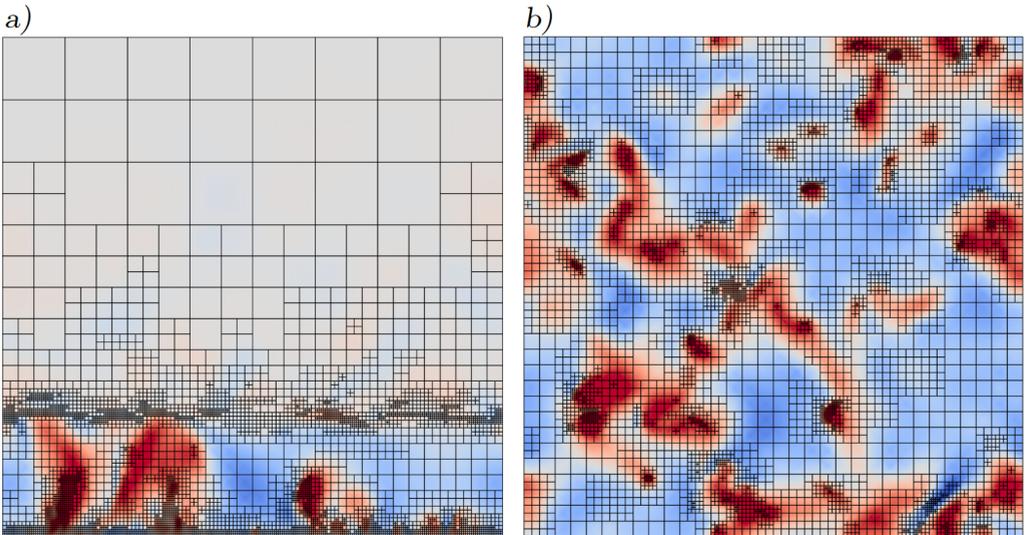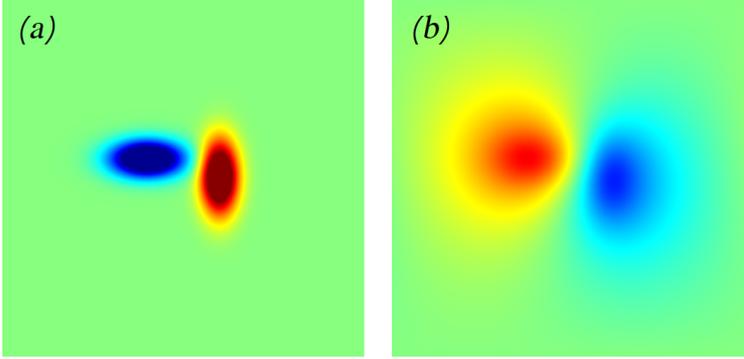

Figure 4.12: A2: A vertical (a) and a horizontal slice (b) of the vertical velocity (color) and the used adaptive-grid structure. These slices are taken over the full domain at $t/T = 6/24$ and the horizontal slice is obtained at height $z = L_c/3$.

(a)

(b)

Poisson's problem appears in many physical systems;

$$\nabla^2 f = s. \tag{4.49}$$

Given s, one may numerically solve for f using Basilisk's (`www.basilisk.fr`) solver that applies a multigrid strategy to an iterative relaxation procedure (à la Brandt; see Popinet, 2019: /src/poisson.h). For testing purposes we define a two-dimensional not-too-trivial right-hand side;

$$s(x,y) = e^{-(x-2)^2 - \left(\frac{y}{2}\right)^2} - e^{-\left(\frac{x+2.}{2}\right)^2 - (y-1)^2}, \tag{4.50}$$

that is know as the source term. The solution $f(x,y)$ on a square domain ($x, y \in \{-10, 10\}$) is unique with the homogeneous Dirichlet boundary conditions at the bottom and top boundaries ($f = 0$), and periodicity is prescribed in the left-right direction. See top figure (a) for s and (b) for the structure of f.

The numerically obtained approximate solution for f (here named; F) differs from the analytical one (f) due to discretization errors that arise from the discrete evaluation of the double derivatives. A total error norm L_F is defined as;

$$L_F = \sum \|\epsilon_i\| \Delta^2, \tag{4.51}$$

where i is a cell-specific index and,

$$\epsilon_i = F_i - f_i, \tag{4.52}$$

is the difference between the approximate cell-averaged solution and the exact cell-averaged solution. We evaluate ϵ_i via f_i taken from a superior resolution computation. This is a more practical alternative to expressing f_i (the cell averaged value of f) analytically. L_F is evaluated on various equidistant grids with 16 to 512 cells in each direction (N) and the results are plotted below (left).

It appears that the solver is second-order accurate. From dimensional arguments and based on the linearity of the system, we can then guess the form of

the leading-order-error term:

$$\epsilon \approx \xi_f = (C_1 f_{xx} + C_2 f_{yy} + C_3 f_{xy}) \Delta^2 + \mathcal{O}(\Delta^3). \qquad (4.53)$$

Since the Poisson equation is isotropic, we recognize,

$$\xi_f = (C_1 s_i + C_3 f_{xy,i}) \Delta^2 + \mathcal{O}(\Delta^3). \qquad (4.54)$$

Next, a least-squares fitting procedure for C_1 and C_3 can be employed to find the universal dimensionless constants for the particular solver: $C_1 \approx -0.06$, and $C_3 \approx 0$. Such semi-empirical approach circumvents the need of a full analytical elaboration of the numerical schemes. The fact that f_{xy} does not appear as an error source can be understood from the fact that the discrete equation for F reads,

$$\nabla^2 F + c (f_{xxxx} + f_{yyyy}) \Delta^2 + \mathcal{O}(\Delta^3) = s, \qquad (4.55)$$

which is not polluted by the cross term (f_{xy}). Hence we plot s_i against ϵ_i for various levels in the bottom figure (right). Note that ϵ_i is scaled with Δ^2 and the on the x-axis, we add the the level-of-refinement used for the computation to better delineate the results obtained from the various grids. The results show that indeed value of the source term s_i is highly correlated with the obtained error. This result could form the basis of a future, more rigorous (cf. Chapt. 2), problem-specific adaptation algorithm.

Apparently, the error-source estimate does not actually converge to a line on higher-resolution grids as there remains some spread in the data-clouds' 'cigar shape'. This is due to non-local errors that arise (Brandt, 1977), as locally-generated errors propagate throughout the domain (see also /Antoonvh/non-local-errors.c). Notice that this generic behavior is not retrieved when using the popular Poisson test problem with the special property that the derivatives of the solution are a fraction of the solution itself (e.g. this Gerris test case: /tests/poisson.html).

For details, see: **http://basilisk.fr/sandbox/Antoonvh/poisson_f.c**
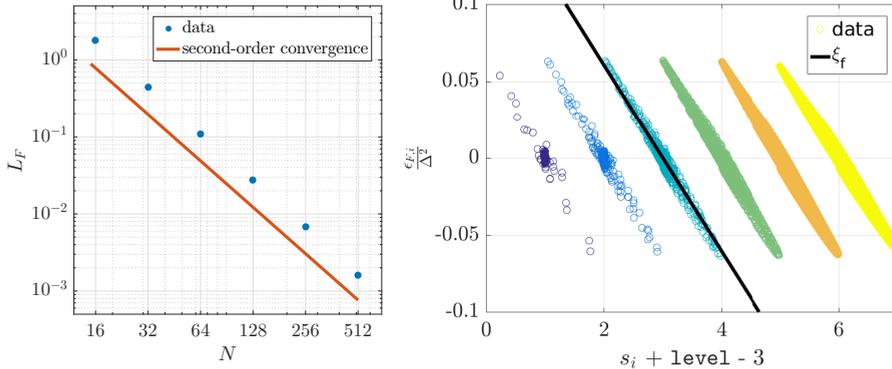
> *There is always a well-known solution to every complex problem – neat, plausible, and wrong.*
>
> Rephrased from H.L. Menken (1917)

5 | A Note on Scalar-Gradient Sharpening in the Stable Atmospheric Boundary Layer

abstract

The scalar front generated by the horizontal self advection of a dipolar vortex through a modest scalar gradient is investigated. This physical scenario is an idealization of the emergence of strong temperature ramps in the stable atmospheric boundary layer. The proposed mechanism is discussed and a two-dimensional analogy is studied in depth using direct numerical simulation. More specifically, the scalar-gradient sharpening is investigated as a function of the Reynolds number. It appears that the process of gradient sharpening at large-eddy scales may be challenging for turbulence-resolving methods applied to the stable-boundary-layer regime.
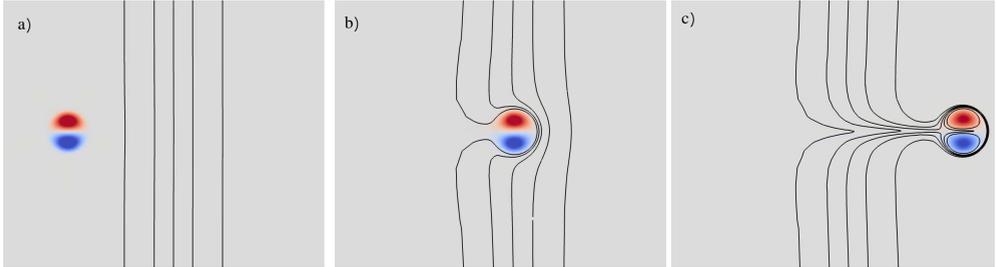
Figure 5.1: The process of scalar-front generation by dipolar self advection at $Re = 800$ (see Sect. 5.2). a) A Lamb–Chaplygin dipolar vortex (vorticity field in colour, with red, positive values and blue, negative) is initialized together with a passive tracer field (black isolines). b) The vortex structure moves to the right through the original scalar front, which is modest in magnitude. c) A much sharper scalar front emerges at the vortex edge. The five isolines indicate 10%, 30%, 50%, 70%, and 90% of the total horizontal scalar field inversion

5.1 Introduction

Coherent scalar-gradient sharping is typically not associated with turbulent flows. As such, the emergence of sharp temperature fronts forms an intriguing aspect of the stable atmospheric boundary layer (SBL). This note concerns the generation of such fronts by dipolar-vortex structures as is illustrated in Fig. 5.1, with a visualization of a two-dimensional (2D) direct numerical simulation (see Sect. 5.2 for details). A dipolar vortex is initialized and advects itself towards a passive scalar front with a moderate spatial gradient (black isolines). The flow structure propagates due to the entrainment of the vortices by each other. As the system evolves, the isolines of the scalar tracer field converge near the edge of the vorticity patches (see also, Eames and Flór, 1998). Hereby the local gradients in the scalar field sharply increase and the dissipation of the scalar-field variance is enhanced.

Scalar fronts in SBL flows have both been observed and modelled. A conditionally-sampled analysis of large-eddy-simulation results by Sullivan et al. (2016) indicates that sharp temperature fronts in the SBL coincide with the dynamics of coherent vortex structures. A horizontal cross-section of such structures revealed a dipolar structure, where two oppositely-signed patches of vorticity are located in each other's vicinity. In their study, such vortex columns are identified as the legs of hairpin vortices commonly found in three-dimensional (3D) wall-bounded turbulent flows (Hommema and Adrian, 2003; Adrian, 2007). Further, it is well known that dipolar vortex structures can easily emerge in stratified flows, as demonstrated by the laboratory experiments of Van Heijst and Flór (1989),Voropayev et al. (1991), and Flór and Van Heijst (1994). Here, vertical motions are limited due to the stratification that may suppress isotropic flow at large scales, which, for sufficiently strong stratification, gives rise to quasi-2D flow. While the identification of coherent vortex structures in the atmosphere from field observations is challenging, and typically relies on indirect footprints of such structures (Cuxart et al., 2002; Barthlott et al., 2007), indications of so-called 'pancake vortex structures' have been reported. Here,

the characteristic motions of the air have a much larger horizontal extent compared with the vertical flow scales (Galperin et al., 2007; Mahrt, 2009; Sun et al., 2015), hinting at vertically-restricted dynamics.

Based on laboratory data, numerical results, and field observations, this study concerns the aforementioned, heavily idealized scenario to describe the generation of large-scale temperature fronts in SBL flows. The self-advective property of dipolar-vortex structures makes them a prime suspect for the generation of scalar fronts. In order to study this process in more depth, the problem is isolated from its meteorological context. It turns out that the scalar-field-gradient amplification in the present surrogate scenario is only limited by the diffusivity of momentum and the scalar quantity. A useful integral measure for the strength of a scalar front is the integral of the squared absolute gradient, which is directly related to the dissipation rate of the scalar-field variance. As such, this study concerns the amplification of the scalar dissipation by dipolar self-advection as a function of the medium's diffusivity.

Computer simulations need to idealize (or parametrize) the complexity of the atmosphere's dynamics in order to reduce a physical problem to a numerical one. The advantage is that this facilitates controlled studies on the interactions between the relevant processes. Even though the present set-up focuses on a candidate building block of the SBL structure, and has little direct resemblance to the full flow reality, the author believes that the detailed analysis yields interesting results for the atmospheric-boundary-layer community. I stress the need for future field observations of turbulence and temperature structures. With promising advancements in observational technologies, such as distributed temperature sensing (Thomas et al., 2012; Lapo et al., 2019) and thermal imaging (Grudzielanek and Cermak, 2015, 2018), there is hope for revelations on this topic.

5.2   Numerical Set-up

In order to model the self advection of a 2D vortex structure, the steady dipolar-vortex model for inviscid flow proposed by H Lamb and SA Chaplygin is employed (Meleshko and Van Heijst, 1994), which describes a vortex structure with a circular radius of size R that propagates without deformation through an otherwise irrotational fluid at a flow speed U. The streamfunction ψ of the so-called Lamb–Chaplygin dipole, moving in the positive x direction, in the co-moving frame of reference is given in cylindrical coordinates (r, θ, see Fig. 5.2) by

$$\psi = \begin{cases} \frac{-2U J_1(kr)}{k J_0(kR)} \sin(\theta), & \text{for } r < R, \\ U \left(\frac{R^2}{r} - r \right) \sin(\theta), & \text{for } r \geq R, \end{cases} \tag{5.1}$$

where $J_0(x)$ and $J_1(x)$ are the zeroth and first Bessel function of the first kind for a dummy variable x, respectively, and k is an inverse length scale with a value such that $kR = 3.83...$, the first non-trivial zero of $J_1(x)$ (i.e. $J_1(3.83...) = 0$).

As a model for a temperature field with an initially moderate horizontal front, a passive tracer field s is used, which gradually changes from low to high values for increasing x, according to
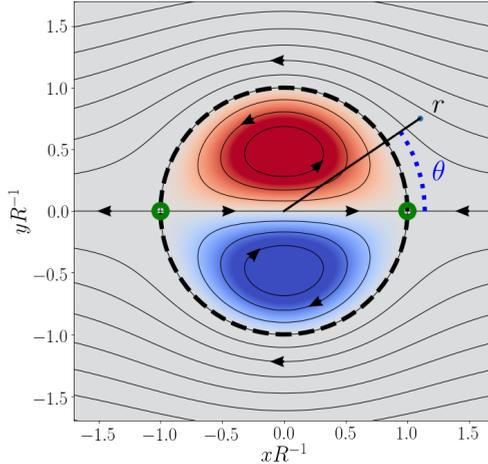
$$s = A \tanh\left(\frac{x}{\sigma}\right), \tag{5.2}$$

Figure 5.2: The flow structure of the Lamb–Chaplygin dipolar vortex, showing the streamlines ($\psi = $ constant) evaluated in the co-moving frame of reference, with the colours indicating the vorticity field ($\omega = \nabla^2 \psi$). The dashed line marks the separatrix, a streamline that encloses the vortex structure. Arrow heads are drawn to indicate the local flow direction and green circles annotate the locations of the stagnation points (see text)

with A an amplitude-of-s scale, 'tanh' the hyperbolic tangent function, and σ is a length scale of the initial scalar transition. Here, $\sigma = 2R$ is chosen and the vortex structure is initially placed at $x = -5R$, where $s \approx -A$, such that it advects towards the right-hand side (r.h.s.) of the initial scalar transition, where $s \approx A$.

A generic feature of dipolar vortices is the so-called separatrix: a streamline in the co-moving frame that encloses the vortex structure and, thereby, the dipole entrains the fluid inside this region. Figure 5.2 depicts the circular separatrix (of radius R) of the Lamb–Chaplygin dipole model and reveals the presence of two stagnation points; two streamlines at $\psi = 0$ coincide. At these stagnation points, the scalar gradient would increase to a singularity if it were not affected by the medium's diffusivity. As such, the flow is considered to be affected by the fluid's viscosity ν, and the evolution of the tracer field s is subject to the diffusivity κ. The following dimensionless parameters can be constructed from the parameters R, U, ν and κ:

$$Re = \frac{UR}{\nu},$$ (5.3)

known as the Reynolds number and,

$$Pr = \frac{\kappa}{\nu},$$ (5.4)

known as the Prandtl number. The latter is set to unity ($Pr = 1$) and the evolution of tracer-field properties is studied as a function of the Reynolds number Re. The range of Re values is restricted to $50 \leq Re \leq 6400$, which covers the limits from minimal

gradient sharpening to the apparent asymptotic scaling for large Re values (see Sect. 5.3).

The set of equations for fluid motion (Navier–Stokes equations) together with the advection–diffusion equation for the tracer field s, are solved in the frame of reference that is co-moving with the initialized dipolar vortex ($u_{\text{trans}} = U$). The evolution of the system is solved until $t_{\text{end}} = 15RU^{-1}$ in a large square domain $\mathcal{D}$ with size $L_0^2 = 25R \times 25R$. The vortex structure is initialized in the domain centre so that the exact location of the domain's boundaries has little influence on the results presented herein. The bulk flow (i.e. u_{trans}) is directed to the left direction inside a free-slip channel with a no-flux condition for the field s at the walls. The left-hand-side (l.h.s.) boundary facilitates outflow conditions by setting the normal derivative to zero for the velocity components (u_x, u_y) and the tracer field s. Inflow occurs at the r.h.s. boundary ($x = x_r$) and applies Dirichlet conditions to $u_x(x_r) = -u_{\text{trans}}$ and $s(x_r) = A \tanh(\frac{x_r + tu_{\text{trans}}}{\sigma})$.

Numerically, the adaptive quadtree-grid solver for the Navier–Stokes equations within the freely-available Basilisk code is employed (see `www.basilisk.fr` and Popinet, 2015)). The adaptive-grid approach is attractive as it consistently chooses a grid resolution based on the fidelity of the discrete representation of the relevant fields, lifting this non-trivial burden from the model user. Further, it focuses the computational resources towards the regions in space and time where they are most required. The numerical schemes are identical to those used in earlier work on adaptive turbulence-resolving simulations (Van Hooft et al., 2018c). The grid-element sizes are adaptively refined and coarsened based on the representation of the second-order polynomial content in the scalar field. Refinement-criterion values for the scalar field ($\zeta_s = 0.02A$) and for the velocity-component fields ($\zeta_{u_i} = 0.02U$) resulted from a convergence study, and aim to balance the accuracy of the results versus the required computational effort (see Van Hooft et al. 2018b for a detailed example). The maximum resolution is not explicitly limited; the algorithm increased it to $R\Delta_{\min}^{-1} = 655.36$ for the run where $Re = 6400$. This mesh-element size corresponds to that of a 16384×16384-cell equidistant grid.

The computer code is available at:
`www.basilisk.fr/sandbox/Antoonvh/gradient-sharpening.c`.

5.3   Results and Implications

Figure 5.1 depicts the global evolution of the flow for $Re = 800$. As the vortex structure moves to the right, the isolines converge at the dipole's separatrix where a large absolute gradient in the tracer field is generated, and defined by

$$\|\boldsymbol{\nabla}s\| = \sqrt{\left(\frac{\partial s}{\partial x}\right)^2 + \left(\frac{\partial s}{\partial y}\right)^2}. \tag{5.5}$$

A global measure for the strength of the scalar front is the domain $\mathcal{D}$ integral of $\|\boldsymbol{\nabla}s\|^2$

$$\epsilon = \iint_{\mathcal{D}} \|\boldsymbol{\nabla}s\|^2 \mathrm{d}O. \tag{5.6}$$
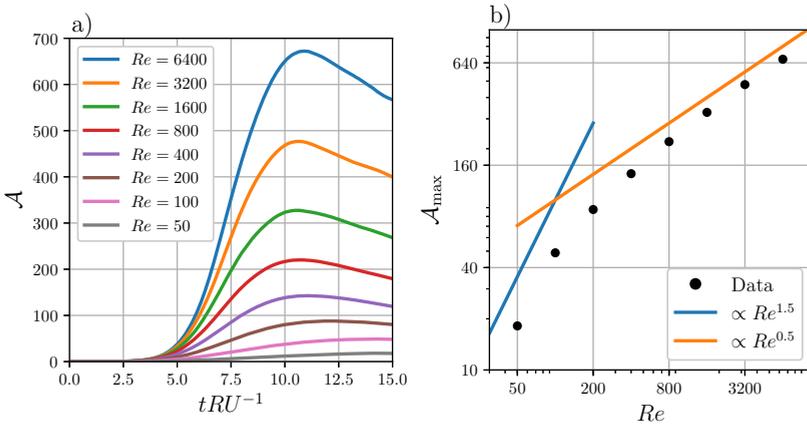
Figure 5.3: (a) The evolution of the scalar-gradient-amplification measure $\mathcal{A}$ (see Eq. 5.8), and (b) the maximum value of $\mathcal{A}$ plotted against the Reynolds number Re on logarithmic scales

In order to quantify the gradient amplification due to the dipole self-advection with a measure that is insensitive to the exact domain size, we take two steps to modify ϵ:

1) ϵ is 'corrected' with its initial value,

$$\epsilon_{\mathrm{DP}} = \epsilon - \epsilon_{t=0}. \tag{5.7}$$

2) The amplification $\mathcal{A}$ is defined by scaling ϵ_{DP} with the initial ϵ-value per unit length R in the y direction, giving

$$\mathcal{A} = \frac{\epsilon_{DP}}{RA \int\limits_{\mathrm{left}}^{\mathrm{right}} \left(\frac{\mathrm{d}}{\mathrm{d}x}\tanh\left(\frac{x}{\sigma}\right)\right)^2 \mathrm{d}x} \equiv \epsilon_{DP}\frac{25}{\epsilon_{t=0}}, \tag{5.8}$$

where the factor 25 is specific for the chosen length of the domain in the y direction $(L_0 R^{-1} = 25)$. The time evolution of the amplification $\mathcal{A}(t)$ is plotted for various Reynolds numbers in Fig. 5.3a. For each of the studied Reynolds numbers, there exists a temporal maximum corresponding to the dipolar vortex being on the r.h.s. of the transition at a time where the diffusivity of the scalar s has not yet started to smooth the scalar gradient. As such, Fig. 5.3b plots the maximum value $\mathcal{A}_{\mathrm{max}}$ against Re, illustrating that for high Re values (say, $Re > 800$), $\mathcal{A}_{\mathrm{max}}$ scales with Re according to

$$\mathcal{A}_{\mathrm{max}} \propto Re^{0.5}, \tag{5.9}$$

which follows the 2D Prandtl boundary-layer theory (Kundu et al., 2015, Chap. 10) and is a consequence of the inviscid scaling of dissipation (Tennekes et al., 1972). For the high Reynolds numbers, the flow field is not significantly affected by the viscosity,

as the Lamb–Chaplygin model is a steady solution in the limit of inviscid flow. For the lower Reynolds numbers (i.e. $Re < 800$), both the momentum and scalar fields are affected by their respective diffusivities (ν and κ). Apparently, this results in a stronger sensitivity to the value of Re compared with the high-Reynolds-number regime.

We conclude from this idealized scenario that 2D dipolar-vortex columns form an effective mechanism for the generation of scalar fronts.

Since temperature fronts are a relevant large-scale feature of the SBL, and indeed, both observations (e.g., Balsley et al., 2003) and numerical simulations show that coherent vortex structures such as hairpins (Adrian, 2007) are the rule rather than the exception in the SBL, the corresponding dynamics should be captured properly by numerical models for the SBL. The results indicate that the severity of the temperature front is sensitive to the value of the Reynolds number or the effective Reynolds number equivalent. For large-eddy simulation, a diffusive subgrid-scale closure is typically invoked to model the flow at the unresolved scales, of which there are a large variety of formulations, and as such, the modelling of flow problems as discussed herein is likely to be sensitive to the details of the chosen closure.

The present example of the 2D surrogate system clearly shows that scalar fronts (e.g., of temperature) may emerge that are much smaller in width than the eddy size itself, and so this challenge was approached by studying a reduced-dimensional problem with respect to the realistic SBL, and an adaptive grid was employed to focus the computer resources. Figure 5.4 depicts the $\|\nabla s\|$ field and the corresponding adaptive-grid structure used for the computations at $t = 10RU^{-1}$ for $Re = 800$. For this dynamical system, a high resolution is required to capture the thin scalar boundary layer at the vortex-structure edge.
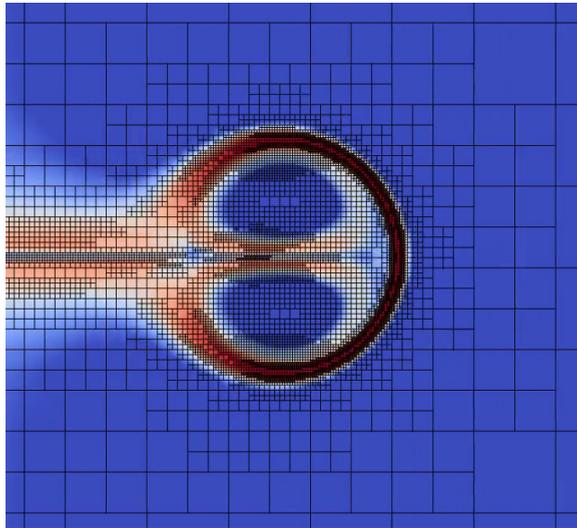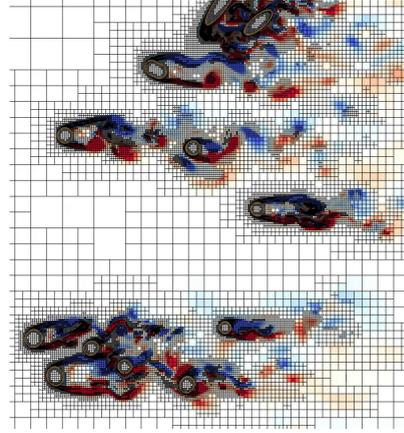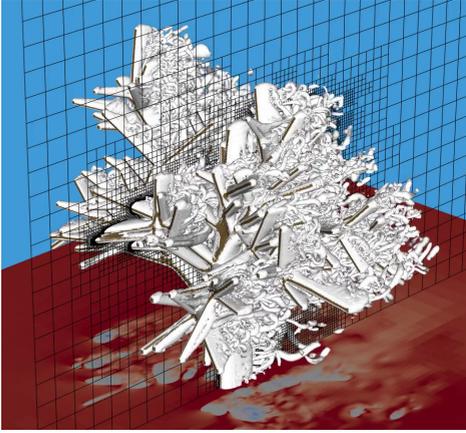

Figure 5.4: A snapshot of the adaptive quadtree-grid structure and the $\|\nabla s\|$ field at $t = 10RU^{-1}$ for the simulation with $Re = 800$. Blue and red colours indicate regions with low and high values for the scalar gradient ($\|\nabla s\|$), respectively.

The earth's surface is not smooth. It is well known that its roughness impacts on the exchange of momentum between the earth and atmosphere. For winds over land, this exchange rate can effectively be characterized using the so-called roughness-length concept. Such a length scale aims to represent the effective drag over a sufficient statistically homogeneous surface (e.g. a forest, grassland, urban, etc.). However, as numerical weather and research models are alloted with ever-increasing resolutions, the effect of roughness transitions and individual obstacles becomes important. The roughness-length model then fails to accurately describe local momentum exchange. As such, a correct formulation of the drag induced by individual roughness elements is desirable.

Trees are an abundant obstacle for the flow near the surface. Such foliage exhibits a natural fractal-like branch structure, seemingly designed to maximize the effectiveness of exchange processes. Those natural objects, even without leaves (say in winter time), are notoriously difficult to characterize in both numerical modeling and wind tunnel studies. Given the 'fractal nature' of tree-grid structures, we were tempted to assess whether AMR methods would be effective in resolving these complex flow problems. With the help of embedded boundaries (a Cut-cell method) it is possible to represent the flow past complex objects on a grid with cubic cells. The top left figure shows a snapshot of the turbulent structures (white λ_2 isosurfaces) induced by the flow passing the tree. The vorticity in the wake owes its existence to the detachment of a thin viscous boundary layer at the surface of the branches. The top right figure shows a zoom-in on a horizontal cross section, displaying the vertical vorticity field and the accompanying adaptive-grid structure. The usage of the adaptive grid enables to resolve the domain with a maximum resolution corresponding to 4096^3 equidistant cells using 'only' 240 cores of the Cartesius super computer facility of Surf Sara.

It would be interesting to extend this research by studying a large variety of tree-like structures. Perhaps, a law can then be formulated that links some effective *tree-complexity parameter* with its momentum exchange efficiency. For

this purpose, we have implemented a simple fractal tree model (as shown above), whose parameters van be varied to construct different trees (see below). Further, the space-colonization algorithm of Runions et al. (2007) has been implemented to generate even more complex tree structures (bottom). Finally, it is possible to use laser-scanning techniques and tree-reconstruction software to obtain a real tree geometry (Du et al., 2019), that is compatible with the Basilisk software (bottom).

Overview of the methods for this project:
`http://www.basilisk.fr/sandbox/Antoonvh/tree/README`
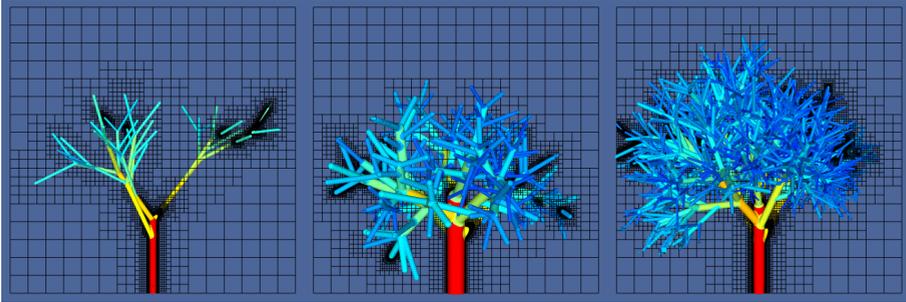
Three simple fractal tree examples. Color coded with the branch radius
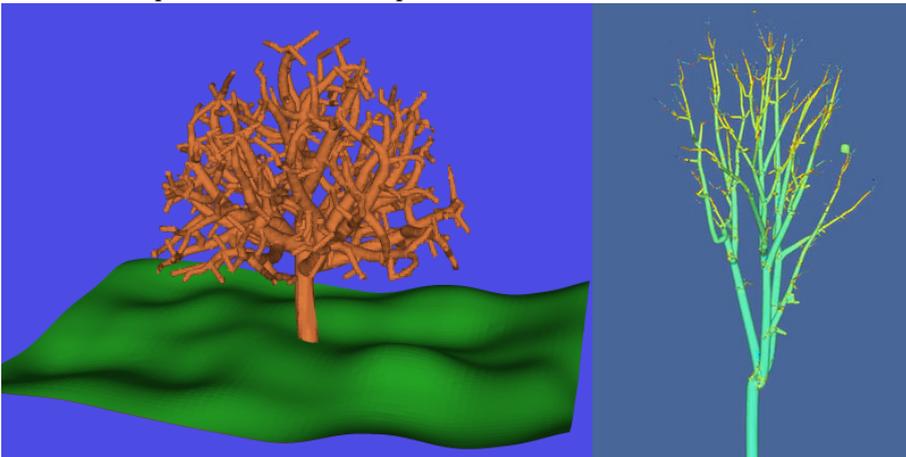
A tree structure based on the space-colonization algorithm of Runions et al. (2007) placed on a artificial surface (left) and a reconstruction of a tree in the Mekel park on the Delft university campus using the software of Du et al. (2019) (right). Color coding follows to the local curvature of the branch. Both trees are represented as an embedded boundary on an octree grid. The point-cloud data was kindly provided by Adriaan L. van Natijne.

> *Not having conclusions is often overlooked as a conclusion.*
>
> Rephrased from I.G.S. van Hooijkdonk (2018) on decision making.

6 | Conclusions and perspective

6.1 Summary of conclusions

In this work we have focused on modeling of the diurnal cycle of the atmospheric boundary layer (ABL). In chapter 2 we motivated investigations on the potential of adaptive numerical methods for turbulence-resolving simulations for research on the diurnal cycle and in chapter 3 we extended this aspect to Reynolds-averaged-Navier-Stokes-based simulations, as used in weather models. Further, in chapter 4 we introduced a conceptual model to describe the most prominent processes that govern the diurnal evolution of the ABL. Since each chapter comes with its own conclusion section, we only briefly summarize here:

1. For cases with a high degree of scale separation in space and/or time, adaptive numerical methods form an interesting alternative to their static counter parts for turbulence-resolving simulations of the ABL. We found that between two state-of-the-art codes, there exists considerable *overhead* for the adaptive method compared to static grids, such that the latter remains the more effective option for the more homogeneous study cases. When increasing the resolution in models, the adaptive method is the only approach where the scaling of the required computational effort inherits the fractal character of the modeled physics. (Chapter 2). Furthermore, it should be realized that in the real atmosphere, heterogeneity and unsteadiness are the rule, rather than the exception. Including these effects more realistically in research models is likely to be favorable for the adaptive approach.

2. A vertically adaptive grid is an effective method to accurately represent the atmospheric boundary layer in weather models with a limited number of grid cells. This particularly aids to numerical resolve part of the boundary layer where turbulent length scales are small, such as in regions with temperature inversions or near the surface. The present work (Chapter 3), only considered a one-dimensional single-column model but the results motive to extend the methods to a full three-dimensional weather model.

3. The last chapter focuses on a conceptual method to describe the main forcings of the atmospheric boundary layer, such that a full diurnal cycle can be simulated (rather than a preset daytime/nighttime case), while allowing for rudimentary atmosphere surface coupling. The main forcing of a diurnal cycle can be summarized with only five dimensionless parameters (Chapter 4). Even though

the systems they describe are highly simplified, they appear to reproduce well known and interesting dynamical aspects of the diurnal cycle. As such, the concepts form an interesting framework for future studies on the diurnal cycle. In particular for 'academic cases' with turbulence resolving models that typically using simplified forcing conditions.

6.2 Perspectives

The author of this thesis cannot help but notice that the statements above are not very 'concluding'. Rather, they motivate to continue research on the aforementioned topics. Especially, the potential of adaptive grids for ABL research is huge and provides the tools to numerically investigate new types of atmospheric problems. It is these types of flows (with a high separation scales), that have not yet benefited from numerical studies. On the other hand, the elephant-in-the-room question: *"Do adaptive-grid methods really work so well for ABL flows?"*, remains difficult to answer based on the contents of this book alone.

Over the past years I have come to the realization that the contents of chapter 2 are not sufficient to persuade the ABL-turbulence-resolving-model community to adopt the adaptive-grid philosophy. That chapter aims to present a proof-of-concept. Probably the best proof would be to actually do original and interesting research using the proposed methods. In fact, the answer on its true potential can only be given, when its advantages and disadvantage are explored over the full spectrum, by scientists from different backgrounds. From 'hard-core' numerical mathematicians, computer and data scientists, technical engineers, physicists, meteorologists and weather forecasters. Indeed, it is not very different from the effort made historically in numerical weather forecasts (see introduction). Only then a true overall assessment can be made. As such, I am exited to have the possibility to extend upon the current work in the coming two years by focusing on the development and application of adaptive numerical methods to a larger variety of meteorological problems.

The planned developments consists of extending the Basilisk code to include more solvers and functions that are of interest for the atmospheric boundary layer community. Including:

1. Moist dynamics,

2. Idealized and realistic surface topographies,

3. Explicit Soil-heat transport,

4. Plant physics,

5. Extended sub-grid-scale-model options,

to mention some. To stimulate the practicality of the method, we hope to provide an 'off-the-shelf' option for new researchers that wish to study problems with a high degree of scale separation. Using these methods, topics of great importance and interest can benefit from the adaptive-grid approach.

Bibliography

Abkar, Mahdi, Ahmad Sharifi, and Fernando PortÃĺ-Agel (2015), "Large-eddy simulation of the diurnal variation of wake flows in a finite-size wind farm." *J Phys: The Conference Series*, 625, 012031.

Adrian, Ronald J (2007), "Hairpin vortex organization in wall turbulence." *Physics of Fluids*, 19, 041301.

Aechtner, Matthias, NK-R Kevlahan, and Thomas Dubos (2015), "A conservative adaptive wavelet method for the shallow-water equations on the sphere." *Quarterly Journal of the Royal Meteorological Society*, 141, 1712–1726.

Angevine, Wayne M., Henk Klein Baltink, and Fred C. Bosveld (2001), "Observations of the morning transition of the convective boundary layer." *Boundary-Layer Meteorology*, 101, 209–227.

Ansorge, Cedrick (2018), "Scale dependence of atmosphere–surface coupling through similarity theory." *Boundary-Layer Meteorology*, 1–27.

Ansorge, Cedrick and Juan Pedro Mellado (2016), "Analyses of external and global intermittency in the logarithmic layer of ekman flow." *J Fluid Mech*, 805, 611–635.

Arrillaga, Jon A, Carlos Yagüe, Mariano Sastre, and Carlos Román-Cascón (2016), "A characterisation of sea-breeze events in the eastern cantabrian coast (spain) from observational data and wrf simulations." *Atmospheric Research*, 181, 265–280.

Baas, P, BJH Van de Wiel, SJA Van der Linden, and FC Bosveld (2018), "From near-neutral to strongly stratified: Adequately modelling the clear-sky nocturnal boundary layer at cabauw." *Boundary-layer meteorology*, 166, 217–238.

Baas, Peter, Bas J. H. Van de Wiel, Erik Van Meijgaard, Etienne Vignon, Christophe Genthon, Steven J. A. Van der Linden, and Stephan R. de Roode (2019), "Transitions in the wintertime near-surface temperature inversion at dome c, antarctica." *Quarterly Journal of the Royal Meteorological Society*, 145, 930–946, URL https://rmets.onlinelibrary.wiley.com/doi/abs/10.1002/qj.3450.

Baas, Peter, BJH Van de Wiel, SJA Van der Linden, and FC Bosveld (2017), "From near-neutral to strongly stratified: Adequately modelling the clear-sky nocturnal boundary layer at cabauw." *Boundary-Layer Meteorology*, 1–22.

Babuška, I and WC Rheinboldt (1979), "Adaptive approaches and reliability estimations in finite element analysis." *Computer Methods in Applied Mechanics and Engineering*, 17, 519–540.

Babuvška, I and Werner C Rheinboldt (1978), "Error estimates for adaptive finite element computations." *SIAM Journal on Numerical Analysis*, 15, 736–754.

Bacon, David P., NashâĂŹat N. Ahmad, Zafer Boybeyi, Thomas J. Dunn, Mary S. Hall, Pius C. S. Lee, R. Ananthakrishna Sarma, Mark D. Turner, Kenneth T. Waight, Steve H. Young, and John W. Zack (2000), "A dynamically adapting weather and dispersion model: The operational multiscale environment model with grid adaptivity (omega)." *Monthly Weather Review*, 128, 2044–2076.

Balsamo, Gianpaolo, Anton Beljaars, Klaus Scipal, Pedro Viterbo, Bart Van den Hurk, Martin Hirschi, and Alan K. Betts (2009), "A revised hydrology for the ecmwf model: Verification from field site to terrestrial water storage and impact in the integrated forecast system." *Journal of Hydrometeorology*, 10, 623–643, URL https://doi.org/10.1175/2008JHM1068.1.

Balsley, Ben B., Rod G. Frehlich, Michael L. Jensen, Yannick Meillier, and Andreas Muschinski (2003), "Extreme gradients in the nocturnal boundary layer: Structure, evolution, and potential causes." *J Atmos Sci*, 60, 2496–2508.

Barthlott, Christian, Philippe Drobinski, Clément Fesquet, Thomas Dubos, and Christophe Pietras (2007), "Long-term study of coherent structures in the atmospheric surface layer." *Boundary-Layer Meteorol*, 125, 1–24, URL https://doi.org/10.1007/s10546-007-9190-9.

Basu, Sukanta, Jean-François Vinuesa, and Andrew Swift (2008), "Dynamic les modeling of a diurnal cycle." *J Appl Meteorol Clim*, 47, 1156–1174.

Bauer, Peter, Alan Thorpe, and Gilbert Brunet (2015), "The quiet revolution of numerical weather prediction." *Nature*, 525, 47.

Beare, R.J. et al. (2006), "An intercomparison of large-eddy simulations of the stable boundary layer." *Boundary-Layer Meteorol*, 118, 247–272.

Beare, Robert J. (2008), "The role of shear in the morning transition boundary layer." *Boundary-Layer Meteorology*, 129, 395–410.

Beetham, Edward, Paul S Kench, Joanne O'Callaghan, and Stéphane Popinet (2016), "Wave transformation and shoreline water level on funafuti atoll, tuvalu." *Journal of Geophysical Research: Oceans*, 121, 311–326.

Behrens, J. (2007), *Adaptive Atmospheric Modeling: Key Techniques in Grid Generation, Data Structures, and Numerical Operations with Applications.* Lecture Notes in Computational Science and Engineering, Springer Berlin Heidelberg, URL https://books.google.nl/books?id=SSyaX3myq4gC.

Berger, Marsha J and Phillip Colella (1989), "Local adaptive mesh refinement for shock hydrodynamics." *Journal of computational Physics*, 82, 64–84.

Berger, Marsha J and Joseph Oliger (1984), "Adaptive mesh refinement for hyperbolic partial differential equations." *Journal of Computational Physics*, 53, 484 – 512, URL http://www.sciencedirect.com/science/article/pii/0021999184900731.

Bertoldi, G, JD Albertson, WP Kustas, F Li, and MC Anderson (2007), "On the opposing roles of air temperature and wind speed variability in flux estimation from remotely sensed land surface states." *Water resources research*, 43.

Betts, Alan K (1986), "A new convective adjustment scheme. part i: Observational and theoretical basis." *Quarterly Journal of the Royal Meteorological Society*, 112, 677–691.

Bosveld, Fred C, Peter Baas, Gert-Jan Steeneveld, Albert AM Holtslag, Wayne M Angevine, Eric Bazile, Evert IF de Bruijn, Daniel Deacu, John M Edwards, Michael Ek, et al. (2014), "The third gabls intercomparison case for evaluation studies of boundary-layer models. part b: results and process understanding." *Boundary-layer meteorology*, 152, 157–187.

Bou-Zeid, Elie (2015), "Challenging the large eddy simulation technique with advanced a posteriori tests." *J Fluid Mech*, 764, 1–4.

Boussinesq, Joseph (1897), *Théorie de l'écoulement tourbillonnant et tumultueux des liquides dans les lits rectilignes à grande section (In French)*, volume 1. Gauthier-Villars.

Brandt, Achi (1977), "Multi-level adaptive solutions to boundary-value problems." *Mathematics of computation*, 31, 333–390.

Bretherton, C.S. et al. (1999), "An intercomparison of radiatively driven entrainment and turbulence in a smoke cloud, as simulated by different numerical models." *Q J R Meteorol Soc*, 125, 391–423.

Brown-Dymkoski, Eric and Oleg V. Vasilyev (2017), "Adaptive-anisotropic wavelet collocation method on general curvilinear coordinate systems." *Journal of Computational Physics*, 333, 414 – 426, URL http://www.sciencedirect.com/science/article/pii/S0021999116307021.

Buckingham, Edgar (1915), "The principle of similitude." *Nature*, 96, 396.

Castillo-Castellanos, Andrés (2017), *Turbulent convection in Rayleigh-Bénard cells with modified boundary conditions*. Theses, Université Pierre et Marie Curie - Paris VI, URL https://hal.sorbonne-universite.fr/tel-01609741.

Chen, T. H., A. Henderson-Sellers, P. C. D. Milly, A. J. Pitman, A. C. M. Beljaars, J. Polcher, F. Abramopoulos, A. Boone, S. Chang, F. Chen, Y. Dai, C. E. Desborough, R. E. Dickinson, L. DÃijmenil, M. Ek, J. R. Garratt, N. Gedney, Y. M. Gusev, J. Kim, R. Koster, E. A. Kowalczyk, K. Laval, J. Lean, D. Lettenmaier, X. Liang, J.-F. Mahfouf, H.-T. Mengelkamp, K. Mitchell, O. N. Nasonova, J. Noilhan, A. Robock, C. Rosenzweig, J. Schaake, C. A. Schlosser, J.-P. Schulz, Y. Shao, A. B. Shmakin, D. L. Verseghy, P. Wetzel, E. F. Wood, Y. Xue, Z.-L. Yang, and

Q. Zeng (1997), "Cabauw experimental results from the project for intercomparison of land-surface parameterization schemes." *Journal of Climate*, 10, 1194–1215.

Clercx, HJH and GJF Van Heijst (2017), "Dissipation of coherent structures in confined two-dimensional turbulence." *Phys Fluids*, 29, 111103.

Coleman, GN, JH Ferziger, and PR Spalart (1994), "A numerical study of the convective boundary layer." *Boundary-Layer Meteorology*, 70, 247–272.

Conzemius, Robert J and Evgeni Fedorovich (2006), "Dynamics of sheared convective boundary layer entrainment. part i: Methodological background and large-eddy simulations." *Journal of the atmospheric sciences*, 63, 1151–1178.

Cuxart, J., G. Morales, E. Terradellas, and C. Yagüe (2002), "Study of coherent structures and estimation of the pressure transport terms for the nocturnal stable boundary layer." *Boundary-Layer Meteorol*, 105, 305–328, URL https://doi.org/10.1023/A:1019974021434.

Cuxart, Joan, Albert AM Holtslag, Robert J Beare, E Bazile, Anton Beljaars, A Cheng, L Conangla, M Ek, F Freedman, R Hamdi, et al. (2006), "Single-column model intercomparison for a stably stratified atmospheric boundary layer." *Boundary-Layer Meteorology*, 118, 273–303.

de Lozar, Alberto and Juan Pedro Mellado (2015), "Mixing driven by radiative and evaporative cooling at the stratocumulus top." *J Atmos Sci*, 72, 4681–4700.

de Roode, Stephan R, Peter G Duynkerke, and Harm JJ Jonker (2004), "Large-eddy simulation: How large is large enough?" *Journal of the atmospheric sciences*, 61, 403–421.

de Roode, Stephan R, Harm JJ Jonker, Bas JH Van de Wiel, Victor Vertregt, and Vincent Perrin (2017), "A diagnosis of excessive mixing in smagorinsky subfilter-scale turbulent kinetic energy models." *J Atmos Sci*, 74, 1495–1511.

De Roode, Stephan R, Irina Sandu, Johan J Van Der Dussen, Andrew S Ackerman, Peter Blossey, Dorota Jarecka, Adrian Lock, A Pier Siebesma, and Bjorn Stevens (2016), "Large-eddy simulations of euclipse–gass lagrangian stratocumulus-to-cumulus transitions: Mean state, turbulence, and decoupling." *J Atmos Sci*, 73, 2485–2508.

Deardorff, James W (1970), "A numerical study of three-dimensional turbulent channel flow at large reynolds numbers." *Journal of Fluid Mechanics*, 41, 453–480.

Dietachmayer, Gary S and Kelvin K Droegemeier (1992), "Application of continuous dynamic grid adaption techniques to meteorological modeling. part i: Basic formulation and accuracy." *Monthly weather review*, 120, 1675–1706.

Du, Shenglan, Roderik Lindenbergh, Hugo Ledoux, Jantien Stoter, and Liangliang Nan (2019), "Adtree: Accurate, detailed, and automatic modelling of laser-scanned trees." *Remote Sensing*, 11, 2074.

Dubos, T and N K-R Kevlahan (2013), "A conservative adaptive wavelet method for the shallow-water equations on staggered grids." *Quarterly Journal of the Royal Meteorological Society*, 139, 1997–2020.

Dunbar, TM, Emmanuel Hanert, and RJ Hogan (2008), "A one-dimensional finite-element boundary-layer model with a vertical adaptive grid." *Boundary-layer meteorology*, 128, 459–472.

Eames, I and J. B. Flór (1998), "Fluid transport by dipolar vortices." *Dyn Atmos Oceans*, 28, 93–105, URL http://www.sciencedirect.com/science/article/pii/S0377026598000463.

Eggers, J, Tamara Grava, MA Herrada, and Giuseppe Pitton (2017), "Spatial structure of shock formation." *Journal of Fluid Mechanics*, 820, 208–231.

Emauel, Kerry A (1994), *Atmospheric convection*. Oxford university press.

England, David E and Richard T McNider (1995), "Stability functions based upon shear functions." *Boundary-Layer Meteorology*, 74, 113–130.

Fedorovich, E, R Conzemius, I Esau, FK Chow, D Lewellen, CH Moeng, D Pino, P Sullivan, and J Vila-Guerau de Arellano (2004), "Entrainment into sheared convective boundary layers as predicted by different large eddy simulation codes, preprints 16th ams symp on boundary layers and turbulence." In *Portland, ME, USA*. Amer meteorol soc, P4.7.

Fidkowski, Krzysztof J and David L Darmofal (2011), "Review of output-based error estimation and mesh adaptation in computational fluid dynamics." *AIAA journal*, 49, 673–694.

Flór, Jan-Bert and Gert-Jan F Van Heijst (1994), "An experimental study of dipolar vortex structures in a stratified fluid." *J Fluid Mech*, 279, 101–133.

Fornberg, Bengt (1998), *A practical guide to pseudospectral methods*, volume 1. Cambridge university press. 216 pp.

Frisch, Uriel (1995), *Turbulence: the legacy of AN Kolmogorov*, chapter 8, 120–194. Cambridge university press.

Fuster, Daniel, Gilou Agbaglah, Christophe Josserand, Stéphane Popinet, and Stéphane Zaleski (2009), "Numerical simulation of droplets, bubbles and waves: state of the art." *Fluid Dyn Res*, 41, 065001.

Galperin, Boris, Semion Sukoriansky, and Philip S Anderson (2007), "On the critical richardson number in stably stratified turbulence." *Atmos Sci Lett*, 8, 65–69.

Garcia, Jade Rachele and Juan Pedro Mellado (2014), "The two-layer structure of the entrainment zone in the convective boundary layer." *Journal of the Atmospheric Sciences*, 71, 1935–1955.

Gibbs, Jeremy A and Evgeni Fedorovich (2014), "Comparison of convective boundary layer velocity spectra retrieved from large-eddy-simulation and weather research and forecasting model data." *Journal of Applied Meteorology and Climatology*, 53, 377–394.

Grell, Georg A, Steven E Peckham, Rainer Schmitz, Stuart A McKeen, Gregory Frost, William C Skamarock, and Brian Eder (2005), "Fully coupled âĂIJonlineâĂİ chemistry within the wrf model." *Atmospheric Environment*, 39, 6957–6975.

Greve, Peter, Kirsten Warrach-Sagi, and Volker Wulfmeyer (2013), "Evaluating soil water content in a wrf-noah downscaling experiment." *Journal of Applied Meteorology and Climatology*, 52, 2312–2327.

Griebel, Michael and Gerhard Zumbusch (2001), "Hash based adaptive parallel multilevel methods with space-filling curves." In *NIC Symposium*, volume 9, 479–492.

Grimsdell, Alison W. and Wayne M. Angevine (2002), "Observations of the afternoon transition of the convective boundary layer." *Journal of Applied Meteorology*, 41, 3–11.

Grudzielanek, A. Martina and Jan Cermak (2015), "Capturing cold-air flow using thermal imaging." *Boundary-Layer Meteorol*, 157, 321–332, URL `https://doi.org/10.1007/s10546-015-0042-8`.

Grudzielanek, A. Martina and Jan Cermak (2018), "Temporal patterns and vertical temperature gradients in micro-scale drainage flow observed using thermal imaging." *Atmosphere*, 9, 498, URL `http://dx.doi.org/10.3390/atmos9120498`.

Günther, Frank, Miriam Mehl, Markus Pögl, and Christoph Zenger (2006), "A cache-aware algorithm for pdes on hierarchical data structures based on space-filling curves." *SIAM Journal on Scientific Computing*, 28, 1634–1650.

Haghshenas, Armin and Juan Pedro Mellado (2019), "Characterization of wind-shear effects on entrainment in a convective boundary layer." *Journal of Fluid Mechanics*, 858, 145–183.

Harten, Ami and James M Hyman (1983), "Self adjusting grid methods for one-dimensional hyperbolic conservation laws." *Journal of computational Physics*, 50, 235–269.

Heinze, Rieke, Anurag Dipankar, Cintia Carbajal Henken, Christopher Moseley, Odran Sourdeval, Silke Trömel, Xinxin Xie, Panos Adamidis, Felix Ament, Holger Baars, et al. (2017), "Large-eddy simulations over germany using icon: a comprehensive evaluation." *Quarterly Journal of the Royal Meteorological Society*, 143, 69–100.

Heus, Thijs, CC Van Heerwaarden, HJJ Jonker, A Pier Siebesma, S Axelsen, K Dries, O Geoffroy, AF Moene, D Pino, SR De Roode, et al. (2010), "Formulation of the dutch atmospheric large-eddy simulation (dales) and overview of its applications." *Geosci Model Dev*, 3, 415–444.

Holtslag, AAM and BA Boville (1993), "Local versus nonlocal boundary-layer diffusion in a global climate model." *Journal of Climate*, 6, 1825–1842.

Holtslag, AAM, Gunilla Svensson, P Baas, S Basu, B Beare, ACM Beljaars, FC Bosveld, J Cuxart, Jenny Lindvall, GJ Steeneveld, et al. (2013), "Stable atmospheric boundary layers and diurnal cycles: challenges for weather and climate models." *Bulletin of the American Meteorological Society*, 94, 1691–1706.

Hommema, Scott E. and Ronald J. Adrian (2003), "Packet structure of surface eddies in the atmospheric boundary layer." *Boundary-Layer Meteorol*, 106, 147–170, URL https://doi.org/10.1023/A:1020868132429.

Howell, JF and J Sun (1999), "Surface-layer fluxes in stable conditions." *Boundary-Layer Meteorology*, 90, 495–520.

Howland, Christopher J, Arnaud Antkowiak, J Rafael Castrejón-Pita, Sam D Howison, James M Oliver, Robert W Style, and Alfonso A Castrejón-Pita (2016), "ItâĂŹs harder to splash on soft solids." *Physical review letters*, 117, 184502.

Jablonowski, Christiane (2004), *Adaptive grids in weather and climate modeling.* Ph.D. thesis, University of Michigan.

Jablonowski, Christiane, Robert C Oehmke, and Quentin F Stout (2009), "Block-structured adaptive meshes and reduced grids for atmospheric general circulation models." *Philosophical Transactions of the Royal Society of London A: Mathematical, Physical and Engineering Sciences*, 367, 4497–4522.

Jeong, Jinhee and Fazle Hussain (1995), "On the identification of a vortex." *Journal of fluid mechanics*, 285, 69–94.

Jonker, Harm JJ, Maarten Van Reeuwijk, Peter P Sullivan, and Edward G Patton (2013), "On the scaling of shear-driven entrainment: a dns study." *Journal of Fluid Mechanics*, 732, 150–165.

Jonker, Harmen JJ and Maria A Jiménez (2014), "Laboratory experiments on convective entrainment using a saline water tank." *Bound-Layer Meteorol*, 151, 479–500.

Kirstetter, Geoffroy, Jie Hu, Olivier Delestre, François Darboux, P-Y Lagrée, Stéphane Popinet, Jose-Maria Fullana, and Christophe Josserand (2016), "Modeling rain-driven overland flow: Empirical versus analytical friction terms in the shallow water approximation." *Journal of Hydrology*, 536, 1–9.

Kolmogorov, Andrey Nikolaevich (1941), "The local structure of turbulence in incompressible viscous fluid for very large reynolds numbers." In *Dokl. Akad. Nauk SSSR*, volume 30, 299–303.

Kosović, Branko and Judith A Curry (2000), "A large eddy simulation study of a quasi-steady, stably stratified atmospheric boundary layer." *Journal of the atmospheric sciences*, 57, 1052–1068.

Kramer, Werner, HJH Clercx, and GJF Van Heijst (2007), "Vorticity dynamics of a dipole colliding with a no-slip wall." *Physics of Fluids*, 19, 126603.

Kudela, Henryk and Andrzej Kosior (2014), "Numerical study of the vortex tube reconnection using vortex particle method on many graphics cards." *Journal of Physics: Conference Series*, 530, 012021, URL `https://doi.org/10.1088%2F1742-6596%2F530%2F1%2F012021`.

Kumar, Vijayant, Jan Kleissl, Charles Meneveau, and Marc B. Parlange (2006), "Large-eddy simulation of a diurnal cycle of the atmospheric boundary layer: Atmospheric stability and scaling issues." *Water Resour Res*, 42. W06D09.

Kumar, Vijayant, Gunilla Svensson, AAM Holtslag, Charles Meneveau, and Marc B Parlange (2010), "Impact of surface flux formulations and geostrophic forcing on large-eddy simulations of diurnal atmospheric boundary layer flow." *Journal of Applied Meteorology and Climatology*, 49, 1496–1516.

Kundu, Pijush K, David R Dowling, Grétar Tryggvason, and Ira M Cohen (2015), *Fluid mechanics*. Academic Press.

Kurzgesagt (2017), "Emergence – how stupid things become smart together." URL `https://www.youtube.com/watch?v=16W7c0mb-rE`.

Lagrée, P-Y, Lydie Staron, and Stéphane Popinet (2011), "The granular column collapse as a continuum: validity of a two-dimensional navier–stokes model with a μ(i)-rheology." *J Fluid Mech*, 686, 378–408.

Lapo, K., A. Freundorfer, L. Pfister, J. Schneider, J. Selker, and C. K. Thomas (2019), "Distributed observations of wind direction using microstructures attached to actively heated fiber-optic cables." *Atmos Meas Tech Disc*, 2019, 1–17, URL `https://www.atmos-meas-tech-discuss.net/amt-2019-188/`.

LeMone, Margaret A., Wayne M. Angevine, Christopher S. Bretherton, Fei Chen, Jimy Dudhia, Evgeni Fedorovich, Kristina B. Katsaros, Donald H. Lenschow, Larry Mahrt, Edward G. Patton, Jielun Sun, Michael TjernstrÃűm, and Jeffrey Weil (2018), "100 years of progress in boundary layer meteorology." *Meteorological Monographs*, 59, 9.1–9.85.

Lenderink, Geert and Albert AM Holtslag (2004), "An updated length-scale formulation for turbulent mixing in clear and cloudy boundary layers." *Quarterly Journal of the Royal Meteorological Society*, 130, 3405–3427.

Li, Yi, Eric Perlman, Minping Wan, Yunke Yang, Charles Meneveau, Randal Burns, Shiyi Chen, Alexander Szalay, and Gregory Eyink (2008), "A public turbulence database cluster and applications to study lagrangian evolution of velocity increments in turbulence." *J Turbul*, 9, 31.

Lim, TT and TB Nickels (1992), "Instability and reconnection in the head-on collision of two vortex rings." *Nature*, 357, 225.

Liu, Shaofeng and Yaping Shao (2013), "Soil-layer configuration requirement for large-eddy atmosphere and land surface coupled modeling." *Atmospheric Science Letters*, 14, 112–117.

López-Herrera, JM, Stéphane Popinet, and AA Castrejón-Pita (2019), "An adaptive solver for viscoelastic incompressible two-phase problems applied to the study of the splashing of weakly viscoelastic droplets." *Journal of Non-Newtonian Fluid Mechanics*, 264, 144–158.

López-Herrera, JM, Stéphane Popinet, and MA Herrada (2011), "A charge-conservative approach for simulating electrohydrodynamic two-phase flows using volume-of-fluid." *J Comput Phys*, 230, 1939–1955.

Lothon, M., F. Lohou, D. Pino, F. Couvreux, E. R. Pardyjak, J. Reuder, J. Vilà-Guerau de Arellano, P. Durand, O. Hartogensis, D. Legain, P. Augustin, B. Gioli, D. H. Lenschow, I. Faloona, C. Yagüe, D. C. Alexander, W. M. Angevine, E. Bargain, J. Barrié, E. Bazile, Y. Bezombes, E. Blay-Carreras, A. Van de Boer, J. L. Boichard, A. Bourdon, A. Butet, B. Campistron, O. de Coster, J. Cuxart, A. Dabas, C. Darbieu, K. Deboudt, H. Delbarre, S. Derrien, P. Flament, M. Fourmentin, A. Garai, F. Gibert, A. Graf, J. Groebner, F. Guichard, M. A. Jiménez, M. Jonassen, A. Van den Kroonenberg, V. Magliulo, S. Martin, D. Martinez, L. Mastrorillo, A. F. Moene, F. Molinos, E. Moulin, H. P. Pietersen, B. Piguet, E. Pique, C. Román-Cascón, C. Rufin-Soler, F. Saïd, M. Sastre-Marugán, Y. Seity, G. J. Steeneveld, P. Toscano, O. Traullé, D. Tzanos, S. Wacker, N. Wildmann, and A. Zaldei (2014), "The bllast field experiment: Boundary-layer late afternoon and sunset turbulence." *Atmos Chem Phys*, 14, 10931–10960.

Louis, J.F., M. Tiedtke, and J.F. Geleyn (1982), "A short history of pbl parameterization at ecmwf." In *paper presented at the Workshop on Planetary Boundary Layer Parameterization, Eur. Cent. For Medium-Range Weather Forecasts, Reading, England.*

Mahrt, Larry (2009), "Characteristics of submeso winds in the stable boundary layer." *Boundary-Layer Meteorol*, 130, 1–14.

Marivela-Colmenarejo, Roberto (2017), *Numerical Perspective on Tsunami Hazards and Their Mitigation by Coastal Vegetation*. Ph.D. thesis, Virginia Tech.

Maronga, B and FC Bosveld (2017), "Key parameters for the life cycle of nocturnal radiation fog: a comprehensive large-eddy simulation study." *Quarterly Journal of the Royal Meteorological Society*, 143, 2463–2480.

Maronga, Bjorn and Katrin Gehrke-Scharf (2018), "Description of the land surface model in palm." URL https://palm.muk.uni-hannover.de/trac/wiki/doc/tec/lsm.

McKeown, Ryan, Rodolfo Ostilla-Mónico, Alain Pumir, Michael P Brenner, and Shmuel M Rubinstein (2018), "Cascade leading to the emergence of small structures in vortex ring collisions." *Physical Review Fluids*, 3, 124702.

Meleshko, VV and GJF Van Heijst (1994), "On chaplygin's investigations of two-dimensional vortex structures in an inviscid fluid." *Journal of Fluid Mechanics*, 272, 157–182.

Mellado, J. P., C. S. Bretherton, B. Stevens, and M. C. Wyant (2018), "Dns and les for simulating stratocumulus: Better together." *Journal of Advances in Modeling Earth Systems*, 10, 1421–1438, URL https://agupubs.onlinelibrary.wiley.com/doi/abs/10.1029/2018MS001312.

Mellado, Juan Pedro, Marc Puche, and Chiel C Van Heerwaarden (2017), "Moisture statistics in free convective boundary layers growing into linearly stratified atmospheres." *Quarterly Journal of the Royal Meteorological Society*, 143, 2403–2419.

Mellor, George L and Tetsuji Yamada (1982), "Development of a turbulence closure model for geophysical fluid problems." *Reviews of Geophysics*, 20, 851–875.

Menken, H.L. (1917), "The devune afflatus." *New York Evening Mail.*

Mirocha, Jeff, Gokhan Kirkil, Elie Bou-Zeid, Fotini Katopodes Chow, and Branko Kosović (2013), "Transition and equilibration of neutral atmospheric boundary layer flow in one-way nested large-eddy simulations using the weather research and forecasting model." *Mon Weather Rev*, 141, 918–940.

Moeng, CH, Jimy Dudhia, Joe Klemp, and Peter Sullivan (2007), "Examining two-way grid nesting for large eddy simulation of the pbl using the wrf model." *Mon Weather Rev*, 135, 2295–2311.

Moin, Parviz and Krishnan Mahesh (1998), "Direct numerical simulation: a tool in turbulence research." *Annual review of fluid mechanics*, 30, 539–578.

Morinishi, Yohei, Thomas S Lund, Oleg V Vasilyev, and Parviz Moin (1998), "Fully conservative higher order finite difference schemes for incompressible flow." *Journal of computational physics*, 143, 90–124.

Muñoz-Esparza, Domingo, Branko Kosović, Clara García-Sánchez, and Jeroen Van Beeck (2014), "Nesting turbulence in an offshore convective boundary layer using large-eddy simulations." *Bound-Layer Meteorol*, 151, 453–478.

Naddei, Fabio, Marta de la Llave Plata, Vincent Couaillier, and Frédéric Coquel (2019), "A comparison of refinement indicators for p-adaptive simulations of steady and unsteady flows using discontinuous galerkin methods." *Journal of Computational Physics*, 376, 508–533.

Neggers, Roel AJ, A Pier Siebesma, and Thijs Heus (2012), "Continuous single-column model evaluation at a permanent meteorological supersite." *Bulletin of the American Meteorological Society*, 93, 1389–1400.

Nieuwstadt, Frans TM, Paul J Mason, Chin-Hoh Moeng, and Ulrich Schumann (1993), "Large-eddy simulation of the convective boundary layer: A comparison of four computer codes." In *Turbulent Shear Flows 8*, 343–367, Springer.

Nieuwstadt, FTM and RA Brost (1986), "The decay of convective turbulence." *Journal of the atmospheric sciences*, 43, 532–546.

Orlandi, Paolo (1990), "Vortex dipole rebound from a wall." *Physics of Fluids A: Fluid Dynamics*, 2, 1429–1436, URL https://doi.org/10.1063/1.857591.

Popinet, S. (2011a), "Quadtree-adaptive tsunami modelling." *Ocean Dyn*, 61, 1261–1285.

Popinet, Stéphane (2003), "Gerris: a tree-based adaptive solver for the incompressible euler equations in complex geometries." *J Comput Phys*, 190, 572–600.

Popinet, Stéphane (2009), "An accurate adaptive solver for surface-tension-driven interfacial flows." *J Comput. Phys*, 228, 5838–5866.

Popinet, Stéphane (2011b), "Quadtree-adaptive tsunami modelling." *Ocean Dynamics*, 61, 1261–1285.

Popinet, Stéphane (2017a), "Multigrid poisson-helmholtz solvers." `http://www.basilisk.fr/src/poisson.h`. Accessed: 2018-01-01.

Popinet, Stéphane (2017b), "Time-implicit discretisation of reactionâĂŞdiffusion equations." `http://www.basilisk.fr/src/diffusion.h`. Accessed: 2018-01-01.

Popinet, Stéphane (2018), "Incompressible navier-stoked solver (centered formulation)." URL `http://basilisk.fr/src/navier-stokes/centered.h`.

Popinet, Stéphane, Murray Smith, and Craig Stevens (2004), "Experimental and numerical study of the turbulence characteristics of airflow around a research vessel." *Journal of Atmospheric and Oceanic Technology*, 21, 1575–1589.

Popinet, StÃľphane (2015), "A quadtree-adaptive multigrid solver for the serreâĂŞgreenâĂŞnaghdi equations." *Journal of Computational Physics*, 302, 336 – 358, URL `http://www.sciencedirect.com/science/article/pii/S0021999115005902`.

Poulos, Gregory S, William Blumen, David C Fritts, Julie K Lundquist, Jielun Sun, Sean P Burns, Carmen Nappo, Robert Banta, Rob Newsom, Joan Cuxart, et al. (2002), "Cases-99: A comprehensive investigation of the stable nocturnal boundary layer." *Bulletin of the American Meteorological Society*, 83, 555–581.

Prein, Andreas F, Wolfgang Langhans, Giorgia Fosser, Andrew Ferrone, Nikolina Ban, Klaus Goergen, Michael Keller, Merja Tölle, Oliver Gutjahr, Frauke Feser, et al. (2015), "A review on regional convection-permitting climate modeling: Demonstrations, prospects, and challenges." *Reviews of geophysics*, 53, 323–361.

Reynolds, Osborne (1895), "On the dynamical theory of incompressible viscous fluids and the determination of the criterion." *Philosophical transacations of the Royal Society of London*, 56, 40–45.

Richardson, Lewis F. (1922), "Weather prediction by numerical process." *Quarterly Journal of the Royal Meteorological Society*, 48, 282–284, URL `https://rmets.onlinelibrary.wiley.com/doi/abs/10.1002/qj.49704820311`.

Rohatgi, Ankit (2018), "Webplotdigitizer." `https://github.com/ankitrohatgi/WebPlotDigitizer`. Accessed via the web interface: 2018-01-01.

Roussel, Olivier, Kai Schneider, Alexei Tsigulin, and Henning Bockhorn (2003), "A conservative fully adaptive multiresolution algorithm for parabolic pdes." *Journal of Computational Physics*, 188, 493–523.

Roy, Christopher (2010), "Review of discretization error estimators in scientific computing." In *48th AIAA Aerospace Sciences Meeting Including the New Horizons Forum and Aerospace Exposition*, 126.

Runions, Adam, Brendan Lane, and Przemyslaw Prusinkiewicz (2007), "Modeling trees with a space colonization algorithm." *NPH*, 7, 63–70.

Sandlin, D. (2018), "Two vortex rings colliding in slow motion - smarter every day 195." URL `https://www.youtube.com/watch?v=EVbdbVhzcM4`.

Schaller, Robert R (1997), "Moore's law: past, present and future." *IEEE spectrum*, 34, 52–59.

Schmidt, Helmut and Ulrich Schumann (1989), "Coherent structure of the convective boundary layer derived from large-eddy simulations." *Journal of Fluid Mechanics*, 200, 511–562.

Schneider, Kai and Oleg V Vasilyev (2010), "Wavelet methods in computational fluid dynamics." *Annu Rev of Fluid Mech*, 42, 473–503.

Shapiro, Alan, Evgeni Fedorovich, and Stefan Rahimi (2016), "A unified theory for the great plains nocturnal low-level jet." *J Atmos. Sci*, 73, 3037–3057.

Siebesma, A.P., C.S. Bretherton, A. Brown, A. Chlond, J. Cuxart, P.G. Duynkerke, H. Jiang, M. Khairoutdinov, D. Lewellen, C.-H. Moeng, E. Sanchez, B. Stevens, and D.E. Stevens (2003), "A large eddy simulation intercomparison study of shallow cumulus convection." *J Atmos. Sci*, 60, 1201–1219. Cited By 317.

Skamarock, William, Joseph Oliger, and Robert L Street (1989), "Adaptive grid refinement for numerical weather prediction." *Journal of Computational Physics*, 80, 27–60.

Skamarock, William C and Joseph B Klemp (1993), "Adaptive grid refinement for two-dimensional and three-dimensional nonhydrostatic atmospheric flow." *Monthly Weather Review*, 121, 788–804.

Slingo, JM (1987), "The development and verification of a cloud prediction scheme for the ecmwf model." *Quarterly Journal of the Royal Meteorological Society*, 113, 899–927.

Sorbjan, Zbigniew (1997), "Decay of convective turbulence revisited." *Boundary-Layer Meteorology*, 82, 503–517.

St-Cyr, Amik, Christiane Jablonowski, John M Dennis, Henry M Tufo, and Stephen J Thomas (2008), "A comparison of two shallow-water models with nonconforming adaptive grids." *Monthly Weather Review*, 136, 1898–1922.

Stull, Roland B (1988), *An introduction to boundary layer meteorology*, volume 1. Springer Science & Business Media. 670 pp.

Sullivan, Peter P, James C McWilliams, and Chin-Hoh Moeng (1996), "A grid nesting method for large-eddy simulation of planetary boundary-layer flows." *Bound-Layer Meteorol*, 80, 167–202.

Sullivan, Peter P, Chin-Hoh Moeng, Bjorn Stevens, Donald H Lenschow, and Shane D Mayor (1998), "Structure of the entrainment zone capping the convective atmospheric boundary layer." *J Atmos Sci*, 55, 3042–3064.

Sullivan, Peter P and Edward G Patton (2011), "The effect of mesh resolution on convective boundary layer statistics and structures generated by large-eddy simulation." *J Atmos. Sci*, 68, 2395–2415.

Sullivan, Peter P, Jeffrey C Weil, Edward G Patton, Harmen JJ Jonker, and Dmitrii V Mironov (2016), "Turbulent winds and temperature fronts in large-eddy simulations of the stable atmospheric boundary layer." *Journal of the Atmospheric Sciences*, 73, 1815–1840.

Sun, Jielun, Carmen J Nappo, Larry Mahrt, Danijel Belušić, Branko Grisogono, David R Stauffer, Manuel Pulido, Chantal Staquet, Qingfang Jiang, Annick Pouquet, et al. (2015), "Review of wave-turbulence interactions in the stable atmospheric boundary layer." *Rev Geophys*, 53, 956–993.

SURFsara (2017), "Cartesius description." https://userinfo.surfsara.nl/systems/cartesius. Accessed: 2017-03-05.

Svensson, Gunilla, AAM Holtslag, V Kumar, T Mauritsen, GJ Steeneveld, WM Angevine, E Bazile, A Beljaars, EIF De Bruijn, A Cheng, et al. (2011), "Evaluation of the diurnal cycle in the atmospheric boundary layer over land as represented by a variety of single-column models: the second gabls experiment." *Boundary-Layer Meteorology*, 140, 177–206.

Tennekes, Hendrik, John Leask Lumley, Jonh L Lumley, et al. (1972), *A first course in turbulence*. MIT Press.

Teyssier, Romain (2002), "Cosmological hydrodynamics with adaptive mesh refinement-a new high resolution code called ramses." *Astron Astrophys*, 385, 337–364.

Thomas, Christoph K., Adam M. Kennedy, John S. Selker, Ayla Moretti, Martin H. Schroth, Alexander R. Smoot, Nicholas B. Tufillaro, and Matthias J. Zeeman (2012), "High-resolution fibre-optic temperature sensing: A new tool to study the two-dimensional structure of atmospheric surface-layer flow." *Boundary-Layer Meteorol*, 142, 177–192, URL https://doi.org/10.1007/s10546-011-9672-7.

Troen, IB and L Mahrt (1986), "A simple model of the atmospheric boundary layer; sensitivity to surface evaporation." *Boundary-Layer Meteorology*, 37, 129–148.

Van de Wiel, Bas J H, Etienne Vignon, Peter Baas, Ivo G S Van Hooijdonk, Steven J A Van der Linden, J Antoon Van Hooft, Fred C Bosveld, Stephan R de Roode, Arnold F Moene, and Christophe Genthon (2017), "Regime transitions in near-surface temperature inversions: A conceptual model." *Journal of the Atmospheric Sciences*, 74, 1057–1073.

Van de Wiel, BJH, AF Moene, OK Hartogensis, HAR De Bruin, and AAM Holtslag (2003), "Intermittent turbulence in the stable boundary layer over land. part iii: A classification for observations during cases-99." *Journal of the atmospheric sciences*, 60, 2509–2522.

Van de Wiel, BJH, AF Moene, HJJ Jonker, P Baas, S Basu, JMM Donda, Jielun Sun, and AAM Holtslag (2012), "The minimum wind speed for sustainable turbulence in the nocturnal boundary layer." *Journal of the Atmospheric Sciences*, 69, 3116–3127.

Van der Linden, Steven JA, Peter Baas, J Antoon Van Hooft, Ivo GS Van Hooijdonk, Fred C Bosveld, and Bas JH Van de Wiel (2017), "Local characteristics of the nocturnal boundary layer in response to external pressure forcing." *Journal of Applied Meteorology and climatology*, 56, 3035–3047.

Van Heerwaarden, Chiel C and Juan Pedro Mellado (2016), "Growth and decay of a convective boundary layer over a surface with a constant temperature." *J Atmos Sci*, 73, 2165–2177.

Van Heerwaarden, Chiel C, Bart JH Van Stratum, Thijs Heus, Jeremy A Gibbs, Evgeni Fedorovich, and Juan Pedro Mellado (2017), "Microhh 1.0: a computational fluid dynamics code for direct numerical simulation and large-eddy simulation of atmospheric boundary layer flows." *Geosci Model Dev*, 10, 3145–3165.

Van Heijst, Gert-Jan F and Jan-Bert Flór (1989), "Dipole formation and collisions in a stratified fluid." *Nature*, 340, 212.

Van Hooft, J. A., S. Popinet, and B. J. H. Van de Wiel (2018a), "Adaptive cartesian meshes for atmospheric single-column models: a study using basilisk 18-02-16." *Geoscientific Model Development*, 11, 4727–4738, URL https://www.geosci-model-dev.net/11/4727/2018/.

Van Hooft, J. A., S. Popinet, and B. J. H. Van de Wiel (2018b), "Adaptive cartesian meshes for atmospheric single-column models: a study using basilisk 18-02-16." *Geosci Model Dev*, 11, 4727–4738, URL https://www.geosci-model-dev.net/11/4727/2018/.

Van Hooft, J Antoon, Stephane Popinet, Chiel C Van Heerwaarden, Steven J A Van der Linden, Stephan R de Roode, and Bas J H Van de Wiel (2018c), "Towards adaptive grids for atmospheric boundary layer simulations." *Boundary-Layer Meteorology*, 167, 421–443.

Van Hooft, J. Antoon, Stéphane Popinet, Chiel C. Van Heerwaarden, Steven J. A. Van der Linden, Stephan R. de Roode, and Bas J. H. Van de Wiel (2018d), "Towards adaptive grids for atmospheric boundary-layer simulations." *Boundary-Layer Meteorology*, 167, 421–443, URL https://doi.org/10.1007/s10546-018-0335-9.

Van Hooijdonk, Ivo G. S., Herman J. H. Clercx, Cedrick Ansorge, Arnold F. Moene, and Bas J. H. Van de Wiel (2018), "Parameters for the collapse of turbulence in the stratified plane couette flow." *Journal of the Atmospheric Sciences*, 75, 3211–3231, URL https://doi.org/10.1175/JAS-D-17-0335.1.

Van Hooijdonk, Ivo GS, Judith MM Donda, Herman JH Clercx, Fred C Bosveld, and Bas JH Van de Wiel (2015), "Shear capacity as prognostic for nocturnal boundary layer regimes." *Journal of the Atmospheric Sciences*, 72, 1518–1532.

Van Liebergen, V.A. (2015), *Interactions in an N finite-dipole system.* Master's thesis, Eindhoven University of Technology, the Netherlands.

Van Stratum, Bart JH and Bjorn Stevens (2015), "The influence of misrepresenting the nocturnal boundary layer on idealized daytime convection in large-eddy simulation." *Journal of Advances in Modeling Earth Systems*, 7, 423–436.

Van Tiggelen, M (2018), *Towards improving the land-surface-atmosphere coupling in the Dutch Atmospheric Large-Eddy Simulation model (DALES).* Master's thesis, Delft University of Technology, the Netherlands.

Van Ulden, AP and J Wieringa (1996), "Atmospheric boundary layer research at cabauw." In *Boundary-Layer Meteorology 25th Anniversary Volume, 1970–1995*, 39–69, Springer.

Vaschy, Aimé (1892), "Sur les lois de similitude en physique." In *Annales télégraphiques*, volume 19, 25–28.

Vasilyev, Oleg V and Christopher Bowman (2000), "Second-generation wavelet collocation method for the solution of partial differential equations." *Journal of Computational Physics*, 165, 660–693.

Vasilyev, Oleg V and Nicholas K-R Kevlahan (2005), "An adaptive multilevel wavelet collocation method for elliptic problems." *Journal of Computational Physics*, 206, 412–431.

Venditti, David A and David L Darmofal (2000), "Adjoint error estimation and grid adaptation for functional outputs: Application to quasi-one-dimensional flow." *Journal of Computational Physics*, 164, 204–227.

Voropayev, S I, Ya D Afanasyev, and I A Filippov (1991), "Horizontal jets and vortex dipoles in a stratified fluid." *J Fluid Mech*, 227, 543–566.

Vreman, AW (2004), "An eddy-viscosity subgrid-scale model for turbulent shear flow: Algebraic theory and applications." *Physics of fluids*, 16, 3670–3681.

Wyant, Matthew C, Christopher S Bretherton, Andreas Chlond, Brian M Griffin, Hiroto Kitagawa, Cara-Lyn Lappen, Vincent E Larson, Adrian Lock, Sungsu Park, Stephan R De Roode, et al. (2007), "A single-column model intercomparison of a heavily drizzling stratocumulus-topped boundary layer." *Journal of Geophysical Research: Atmospheres*, 112.

Zheng, J., J. Zhu, Z. Wang, F. Fang, C. C. Pain, and J. Xiang (2015), "Towards a new multiscale air quality transport model using the fully unstructured anisotropic adaptive mesh technology of fluidity (version 4.1.9)." *Geoscientific Model Development*, 8, 3421–3440, URL https://www.geosci-model-dev.net/8/3421/2015/.

Zhou, Y, P-Y Lagrée, S Popinet, P Ruyer, and P Aussillous (2017), "Experiments on, and discrete and continuum simulations of, the discharge of granular media from silos with a lateral orifice." *Journal of Fluid Mechanics*, 829, 459–485.

List of publications

Vignon, E., van de Wiel, B.J.H, van Hooijdonk, I.G.S, Genthon, C., van der Linden, S.J.A., van Hooft, J.A., Baas, P, Maurel, W., Traullé, O. and Casasanta, G. (2017): *Stable boundary-layer regimes at Dome C, Antarctica: observation and analysis.* Q.J.R. Meteorol. Soc.,
doi: 10.1002/qj.2998

van de Wiel, B.J.H, Vignon, E Baas, P, van Hooijdonk, I.G.S, van der Linden, S.J.A., van Hooft, J.A., Bosveld, F.C, de Roode, S.R., Moene, A.F. and Genthon, C. (2017): *Regime Transitions in Near-Surface Temperature Inversions: A Conceptual Model.* J. Atmos. Sci.,
doi: 10.1175/JAS-D-16-0180.1

van der Linden, S.J.A, Baas, P, van Hooft, J. A, van Hooijdonk, I.G.S, Bosveld, F.C., and van de Wiel, B.J.H. (2017): *Local Characteristics of the Nocturnal Boundary Layer in Response to External Pressure Forcing.* J. Appl. Meteor. Climatol.,
doi: 10.1175/JAMC-D-17-0011.1

van Hooft, J. A, Popinet, S. van Heerwaarden, C. C., van der Linden, S.J.A., de Roode, S.R., and van de Wiel, B.J.H. (2018): *Towards Adaptive Grids for Atmospheric Boundary-Layer Simulations.* Bound.-Lay. Meteor.,
doi: 10.1007/s10546-018-0335-9

van Hooft, J. A., Popinet, S. and van de Wiel, B. J. H. (2018): *Adaptive Cartesian meshes for atmospheric single-column models: a study using Basilisk 18-02-16,* Geosci. M. Dev.,
doi: 10.5194/gmd-11-4727-2018

Izett J., van de Wiel B.J.H., Baas, P., van Hooft J.A. and Schulte R. (2019): *Dutch Fog: On the Observed Spatio-Temporal Variability of Fog in the Netherlands.* Q.J.R. Meteorol. Soc.,
doi: 10.1002/qj.3597

van Hooft, J. A., Baas P, van Tiggelen M, Ansorge C and van de Wiel, B.J.H. (2019) *An idealized description for the diurnal Cycle of the dry atmospheric boundary layer.* J. Atmos. Sci.,
doi:10.1175/JAS-D-19-0023.1

Heusinkveld, V.W.J., van Hooft, J.A., Schilderpoort, B, Baas, P, ten Veldhuis, M, and van de Wiel., B.J.H. (2020): *Towards a physics-based understanding of fruit forst protation using wind machines* Argi. and For. Meteor.,
doi: 10.1016/j.agrformet.2019.107868

van Hooft, J.A. (2020): *A Note on the Scalar-Gradient Sharpening in the Stable Atmospheric Boundary Layer* Bound.-Lay Meteor.,
doi:10.1007/s10546-020-00516-x

Acknowledgements

PhD studies only succeed when there is a synergy between student and supervisor. For this reason, I am convinced I could not have made a better choice than doing my PhD project with Bas (i.e. *Prof.* Dr. ir. Van de Wiel). It requires true scientific begeisterung and confidence to facilitate student expeditions into unfamiliar territory. I am grateful for his energizing enthusiasm, abundance of association and great guidance.

Curriculum Vitae

25 Feb. 1989	Born in Hoenzadriel, The Netherlands
1994–2001	OBS *De Meidoorn*, Kerkdriel
2001–2008	*Scholengroep Cambium*, Zaltbommel. Havo & Atheneum
2008	Licensed Taxi driver
2008–2013	Bachelor Technische Natuurkunde,
	Technische Universiteit Eindhoven
	Thesis: Tunable Optical Filters for the K-STAR Fusion Reactor
2009	Licensed Truck driver (articulated, 50 tonnes)
2012	Physics teacher Qualification,
	Eindhoven School of Education
	Intership at *Bischop Beckers college*, Eindhoven, The Netherlands
2013–2015	Master Applied Physics, Specialization in fluid dynamics
	Technische Universiteint Eindhoven
	Intership at *DAF trucks N.V.*, Eindhoven, The Netherlands
	Thesis: *The Dynamical Behaviour of Dipolar Vortices*
	near Sharp-Edged Boundaries
2015–2019	PhD candidate in Atmospheric Physics,
	Delft University of Technology
2019–present	Research fellow in Atmospheric Physics,
	Delft University of Technology

Encore: The implementation cycle of scientific methods

1) *Code up the methods*
 ↪ The code does not compile.
2) *Some more coding to fix it*
 ↪ It compiles(!), but does not run.
3) *Some more coding to fix it*
 ↪ It runs(!), but produces garbage output.
4) *Some more coding to fix it*
 ↪ Output seems OK(!), but does not pass the selected quantitative tests.
5) *Some more coding to fix it*
 ↪ It now passes the selected tests.
Your methods are ready to be used now!